NAVAL POSTGRADUATE SCHOOL

MONTEREY, CALIFORNIA

THESIS

PACKAGING AND CHARACTERIZATION OF BIO-INSPIRED UNDERWATER MEMS DIRECTIONAL SOUND SENSOR

by

Alberto Antonio Espinoza Peyrot

June 2019

Thesis Advisor:	Gamani Karunasiri
Co-Advisor:	Fabio D. Alves

Approved for public release. Distribution is unlimited.

THIS PAGE INTENTIONALLY LEFT BLANK

REPORT DOCUMENTATION PAGE	*Form Approved OMB No. 0704-0188*

1. AGENCY USE ONLY *(Leave blank)*	**2. REPORT DATE** June 2019	**3. REPORT TYPE AND DATES COVERED** Master's thesis

4. TITLE AND SUBTITLE PACKAGING AND CHARACTERIZATION OF BIO-INSPIRED UNDERWATER MEMS DIRECTIONAL SOUND SENSOR	**5. FUNDING NUMBERS** MEMS Directional Mic
6. AUTHOR(S) Alberto Antonio Espinoza Peyrot	
7. PERFORMING ORGANIZATION NAME(S) AND ADDRESS(ES) Naval Postgraduate School Monterey, CA 93943-5000	**8. PERFORMING ORGANIZATION REPORT NUMBER**
9. SPONSORING / MONITORING AGENCY NAME(S) AND ADDRESS(ES) N/A	**10. SPONSORING / MONITORING AGENCY REPORT NUMBER**

11. SUPPLEMENTARY NOTES The views expressed in this thesis are those of the author and do not reflect the official policy or position of the Department of Defense or the U.S. Government.

12a. DISTRIBUTION / AVAILABILITY STATEMENT Approved for public release. Distribution is unlimited.	**12b. DISTRIBUTION CODE** A

13. ABSTRACT (maximum 200 words)

The thin-line towed array hydrophones and vector sensors are commonly used to determine the bearing of sound sources in underwater environments. In this thesis, a MEMS-based directional underwater acoustic sensor (inspired by the ears of the fly *Ormia Ochracea*) is explored. The sensor operates in a narrow frequency band where the mechanical resonance frequency determines the operating frequency. The sensor consists of two wings connected by a bridge and the assembly is pivoted to a substrate using two torsional legs. The electronic readout of the response is obtained using a pair of interdigitated comb finger capacitors attached to the wings. The MEMS sensor was designed using COMSOL finite element modeling and a suitable package was developed for underwater testing. The performance of the sensor was characterized in air using an anechoic chamber, and underwater testing was done using NPS and TRANSDEC water tanks. Measurements showed that the operating frequency of the sensor in air is about 1600 Hz while underwater it shifted to a lower frequency (285 Hz), primarily due to mass loading from the fluid used for immersing the sensor. The peak sensitivity of the MEMS sensor was found to be about -160 dB (re 1V/uPa), which is about 30 dB higher than conventional broadband hydrophones. The sensor showed good directional response with dipole pattern. The results show the potential of MEMS sensors for underwater applications to detect the bearing of sound sources.

14. SUBJECT TERMS vector MEMS sensor, material acoustical properties, sensitivity underwater calibration, directivity pattern underwater calibrations, finite element design, micromachining	**15. NUMBER OF PAGES** 111
	16. PRICE CODE

17. SECURITY CLASSIFICATION OF REPORT Unclassified	**18. SECURITY CLASSIFICATION OF THIS PAGE** Unclassified	**19. SECURITY CLASSIFICATION OF ABSTRACT** Unclassified	**20. LIMITATION OF ABSTRACT** UU

NSN 7540-01-280-5500

Standard Form 298 (Rev. 2-89)
Prescribed by ANSI Std. 239-18

THIS PAGE INTENTIONALLY LEFT BLANK

PACKAGING AND CHARACTERIZATION OF BIO-INSPIRED UNDERWATER MEMS DIRECTIONAL SOUND SENSOR

Alberto Antonio Espinoza Peyrot
Lieutenant, Mexican Navy
BS, Escuela de Ingenieros de la Armada de México, 2009

Submitted in partial fulfillment of the
requirements for the degree of

MASTER OF SCIENCE IN ENGINEERING ACOUSTICS

from the

NAVAL POSTGRADUATE SCHOOL
June 2019

Approved by: Gamani Karunasiri
Advisor

Fabio D. Alves
Co-Advisor

Oleg A. Godin
Chair, Department of Physics

THIS PAGE INTENTIONALLY LEFT BLANK

ABSTRACT

The thin-line towed array hydrophones and vector sensors are commonly used to determine the bearing of sound sources in underwater environments. In this thesis, a MEMS-based directional underwater acoustic sensor (inspired by the ears of the fly *Ormia Ochracea*) is explored. The sensor operates in a narrow frequency band where the mechanical resonance frequency determines the operating frequency. The sensor consists of two wings connected by a bridge and the assembly is pivoted to a substrate using two torsional legs. The electronic readout of the response is obtained using a pair of interdigitated comb finger capacitors attached to the wings. The MEMS sensor was designed using COMSOL finite element modeling and a suitable package was developed for underwater testing. The performance of the sensor was characterized in air using an anechoic chamber, and underwater testing was done using NPS and TRANSDEC water tanks. Measurements showed that the operating frequency of the sensor in air is about 1600 Hz while underwater it shifted to a lower frequency (285 Hz), primarily due to mass loading from the fluid used for immersing the sensor. The peak sensitivity of the MEMS sensor was found to be about -160 dB (re 1V/uPa), which is about 30 dB higher than conventional broadband hydrophones. The sensor showed good directional response with dipole pattern. The results show the potential of MEMS sensors for underwater applications to detect the bearing of sound sources.

THIS PAGE INTENTIONALLY LEFT BLANK

TABLE OF CONTENTS

LIST OF FIGURES

THIS PAGE INTENTIONALLY LEFT BLANK

LIST OF TABLES

LIST OF ACRONYMS AND ABBREVIATIONS

AUV	autonomous underwater vehicle
ATAB	acoustic-thermoviscous acoustic boundary
CAD	computer-aided design
CAE	computer-aided engineering
DI	directivity index
DRIE	deep reactive ion etching
DTLTA	digital thin-line towed array
FE	finite-element computational tools
MEMS	microelectromechanical systems
MUMPS	multi-user MEMS processes
NPS	Naval Postgraduate School
PA	pressure acoustics frequency domain interface
PML	perfectly matched layer
POLYMUMPS	polysilicon surface micromachining process
PVD	physical vapor deposition
SLITA	slim towed array
SM	solid mechanics interface
SOI	silicon on insulator
SOIMUMPS	silicon-on-insulator micromachining process
SRL	Sensor Research Lab
TA	thermoviscous acoustics frequency domain interface
TASB	thermoviscous acoustic-structure boundary
TRANSDEC	Transducer Evaluation Center
UAV	unmanned aerial vehicle
UDS	underwater detection systems
USV	unmanned surface vehicle
UUV	unmanned underwater vehicle

THIS PAGE INTENTIONALLY LEFT BLANK

ACKNOWLEDGMENTS

Thank you to

- My country, Mexico, and the United States for this enriching experience.
- Secretaría de Marina-Armada de México (SEMAR) and the United States Navy for the tremendous efforts toward sea technology development.
- Instituto de Investigación y Desarrollo Tecnológico de la Armada de México (INIDETAM) and Naval Postgraduate School (NPS) for all the shared knowledge.
- Vicealmirantes Rene White Herrera, Rubén Ceballos Guevara and César Carlos Preciado Velázquez, Contralmirante Cuauhtémoc Urrea Urías and Capitán de Navío Miguel Alvarado Juárez for this opportunity.
- Professors Gamani Karunasiri, Fabio Alves, Dragoslav Grbovic, and Renato Rabelo for your tireless support, patience, and countless hours of advice.
- Professors Bruce Denardo and Oleg Godin for bringing me the incredible experience of learning acoustics.
- Jay Adeff, Jeffrey Catterlin, Steven Jacobs, and Johannes Linke for an endless will to help and support. In addition, Steve Pucillo at TRANSDEC provided assistance in the underwater characterization of sensors.
- Jayyeung Park, German Da Re, Parminder Riarh, and Sangmin Lee for your friendship, team effort, and cooperation.
- My family for their support.
- Berenice, the love of my life, and our two beloved daughters, Sophia and Grecia—without you it would have been impossible.

I. INTRODUCTION

Adapting biological sensing mechanisms to microelectromechanical systems (MEMS) allows for the emulation of efficient and effective mechanisms that nature has mastered through evolution. One of the areas of interest to us is miniature directional sound sensors based on biological systems.

Last-century technology [1] employs sensor arrays made from omnidirectional microphones that require spacing proportional to the wavelength of the source to be located. These arrays require time delay, amplitude difference, or phase weighting algorithms to determine the direction of the detected sound [2].

One of the most commonly used arrangements for acoustic direction finding is based on linear arrays. These sensors have evolved over the years, from very heavy and complex systems that required significant space onboard ships to thin light linear arrays easily handled by relatively small autonomous platforms [3].

Specifically, for underwater applications the main component of these systems is the hydrophone. Conventional hydrophones are relatively bulky and omnidirectional in the low-frequency range. The MEMS hydrophone under development at NPS, however, is a relatively small vector-sensor operating in a narrow frequency band. Its directivity characteristics can help to reduce size and weight of underwater detection systems (UDS). MEMS vector sensors combine the directionality and reduced size needed to create small, low-power-consuming and accurate UDS.

The MEMS acoustic sensor in development at the Naval Postgraduate School (NPS) Sensor Research Lab (SRL) is based on the biological acoustic system of the *Ormia Ochracea* parasitic fly. This system can detect frequencies that have a much larger wavelength with respect to the size of the biological sensor. Miles [4] explains that the direction-finding capability of the sensor is due to the mechanical coupling of the eardrums of the fly, enhancing the time difference between arrivals of sound in order to improve its directional sensitivity.

A. UNDERWATER DETECTION TECHNOLOGIES

Throughout history, different approaches have been tried to improve underwater detection capabilities: mounted and/or deployed from ships, submarines, helicopters, airplanes, and most recently unmanned vehicles.

The sensors employed can be hull mounted; ship, submarine, or unmanned vehicle towed; air deployed; or bottom mounted. Towed array systems can be installed in ships, submarines, or unmanned underwater vehicles, to allow detection of underwater acoustic sources.

Particularly, monostatic passive towed arrays are used to locate acoustic sources emitting at the lower frequency bands of the acoustic spectrum. One of the main difficulties while using a towed array resides in the left-right ambiguity, which requires a series of ship's maneuvers to be performed. From the perspective of the author, linear arrays are evolving in two ways: 1) from large and heavy systems that have a nominal weight between 2–5 tons, to thin line arrays to be used in unmanned vehicles; and 2) from arrays of omnidirectional hydrophones to arrays of vector sensor variations capable of solving the left-right ambiguity. Some studies have also evaluated how combining vector and scalar sensors could improve array sensitivity and directivity [5].

Some of the approaches employed to build thin-line towed arrays and vector sensors are summarized in the following sections, describing the principles involved and the results obtained by the different research groups. The vector sensors described in the literature and summarized here as regular-size hydrophones using some additional sensor that measure various characteristics of the acoustic field are MKI, MKII, Hydroflown, Wilcoxon vector sensor, SV-1, and SV-2 hydrophones. The MEMS sensors described here are the bionic sensor, T-shaped sensor, MEMS accelerometer, and micromachined piezoceramic hydrophones. Finally, the bioinspired *Ormia Ochracea*-based underwater acoustic sensor is described.

1. Thin-Line Towed Arrays

The main motivation pushing forward the design of this sensing technology is the advances in unmanned air, underwater, and surface vehicle (UAV, UUV, and USV) technologies [6]. These vehicles require lighter sensors, which can be towed or deployed.

To achieve an efficient thin-line towed array, small hydrophones have to be adapted, and turbulence noise [7] and left-right ambiguity have to be resolved. Several designs have been tested and reported in the literature; each of them uses different sensing elements in order to reduce diameter and weight:

1. DTLTA. The Acoustic Research Laboratory of the National University of Singapore designed a Digital Thin Line Towed Array (DTLTA). Its main characteristics are 10-mm diameter and 12-m long array, weighing no more than 2 kg (excluding the tow cable) [6].

   DTLTA comprises 11 acoustic sensing "super-elements" as the one shown in Figure 1. "Each super-element is built using six individual ceramic hydrophones … (EDO, Micro-line elements) with its signal conditioning electronics. … The number of element [s] … provide [s] an omni directional response [at 2.5 kHz]… The individual sensing elements … are about 2.3 mm in external diameter and 8 mm long." [6]

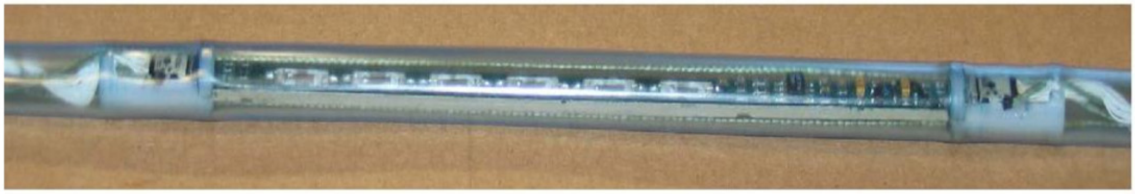

Figure 1. Super-element employed on DTLTA. Source: [6].

2. THINARRAY. Thin-line array of 8-mm outside diameter, using a 6-by-120-mm super-element. The super-element uses "small cylindrical air-

backed ceramic sensors mounted on one side and all the electronic components in the other" [7].

3. SLITA. Slim Towed Array for Autonomous Underwater Vehicle (AUV), with 31-mm diameter, 15-m length acoustic module, 2 octave modules of 1780 and 3550 Hz, 48 cylindrical hydrophones Benthos AQ-4 with a -201 V/µPa sensitivity, 33-mm length and 13-mm diameter [8].

The examples listed in this section do not use vector sensors or MEMS hydrophones as part of the passive elements. They use small omnidirectional hydrophones, which, in order to improve performance and reduce size, could be substituted by MEMS vector sensors with similar sensitivities, smaller sizes, and directional responses, as suggested by [9] and [10].

2. Hydrophones for Towed Arrays

Among the many elements that constitute a passive sonar are the receiving elements, known as hydrophones. This kind of sensor is based on different transducing principles, being the most employed electromechanical transduction.

A hydrophone to be employed in a sensor array is selected by its frequency response, sensitivity, noise floor, resistance to harsh environments, resistance to heavy-duty use and, more recently, its directionality. Some of the technologies used are:

1. Single-element pressure-based. These hydrophones provide a broadband omnidirectional detection, consisting of a single transducer element. These sensors are usually built from a cylindrical piezoceramic element, radially polarized and closed-ended, which in turn will vary the resonance frequency of the designed element [11].

2. Triplet technology. This particular array is formed using three omnidirectional hydrophones. A triplet is designed by locating each transducer element in the corner of an equilateral triangle [12]. Triplet hydrophone arrays exhibit as one of the disadvantages with respect to vector sensors: "limitations in inter-element spacing, which limits the

upper bound on the working frequency, as well as a steering error that depends on the number of triplets on the array and the steer angle" [12].

3. Vector sensors. This kind of sensor is designed to acquire "not only the pressure wave generated by sound which in fact is a scalar component, but also a vector quantity related with the sound field" [8]. One of the most commonly used vector variables is the particle velocity due to volumetric motion [13]. This variable carries directional information of the acoustic energy propagation, which helps to identify the direction of the source.

   As indicated by Sherman and Butler [11], one of the limitations of piezoelectric vector sensors is decreasing response below resonance, "at a rate of 6 dB/octave and with a 90° phase shift relative to the response of a pressure hydrophone." [11]

4. MEMS sensors. As regular hydrophones, these can be omnidirectional or have directional characteristics. The common feature is the use of micromachining processes to reach a final micro device.

3. Vector Sensors

Vector sensors are classified by the physical principle used to determine the direction of an acoustic wave. As the acoustic wave is traveling in space, it produces variation in pressure, volume, and temperature gradients. Those changes can be measured to determine the direction of propagation of the acoustic signal.

The vector behavior of an acoustic sensor is analyzed by its directivity pattern. This characteristic of a sensor is the quantitative measurement of "an interference pattern consisting of angular regions of high intensity (lobes) separated by angular regions of low intensity (nulls)" [11].

Merhaut [14] classifies electromechanical transducers into two groups based on electromagnetic and electrostatic principles [14]. Each of these groups is subdivided "according to the manner in which the electromechanical transducer is connected with the external acoustic field [15]," on orders that start at zero and are numbered until the nth order [15]. Additionally, each of these orders is characterized by the dominant effect that describes the behavior of the frequency characteristic—compliance or capacitance, mass or inductance, and damping or resistance—depending on the variables used on the lumped circuit to describe the sensor [14].

The order of the transducers describes the shape of the directivity pattern. This characteristic of the sensor is given by the order of the sinusoidal function related to the output signal produced by the sensor, according to Equation 1.1 given by [15]:

$$H\left(\phi\right)=\cos^{n}\left(\phi\right) \tag{1.1}$$

Where H represents the receive sensitivity as a function of angle, ϕ can represent azimuthal angular dependence, and "n" is the order value [15]. The zeroth order (n=0) corresponds to omnidirectional sensors, also called monopole sensors. The first order (n=1) corresponds to sensors whose directivity pattern shows the characteristic "figure of eight," also called dipole sensors [15].

The most common characteristic of the acoustic wave employed to determine the direction of sound is the pressure gradient. A pressure gradient is defined as a change in direction and rate in pressure at two closely spaced points [16].

Several approaches have been studied and combined to produce a directional response of underwater acoustic sensors. Some of the approaches published in technical literature are the following:

1. MKI and MKII. These dual-sensor hydrophones allowed the use of pressure-based omni-directional hydrophones and accelerometers to acquire additional information of the direction of the source [17]. MKI design focused on miniaturizing a 3D vector sensor to be fitted in slim towed arrays (18 mm diameter) adapting six Endevco model 12M1A PicochipTM accelerometers (two-axis). MKII intended to improve sensitivity and noise floor by adapting a neutrally buoyant housing using a KS90 accelerometer from the company IDS immonic. MKI characteristics are: sensitivity -235 dB re 1 V/µPa at 6 kHz and good 8-pattern above 4

kHz. MKII characteristics are: sensitivity -197.5 dB re 1 V/µPa at 6 kHz and good 8-pattern at 4 kHz. Both characteristics are shown in Figure 2.

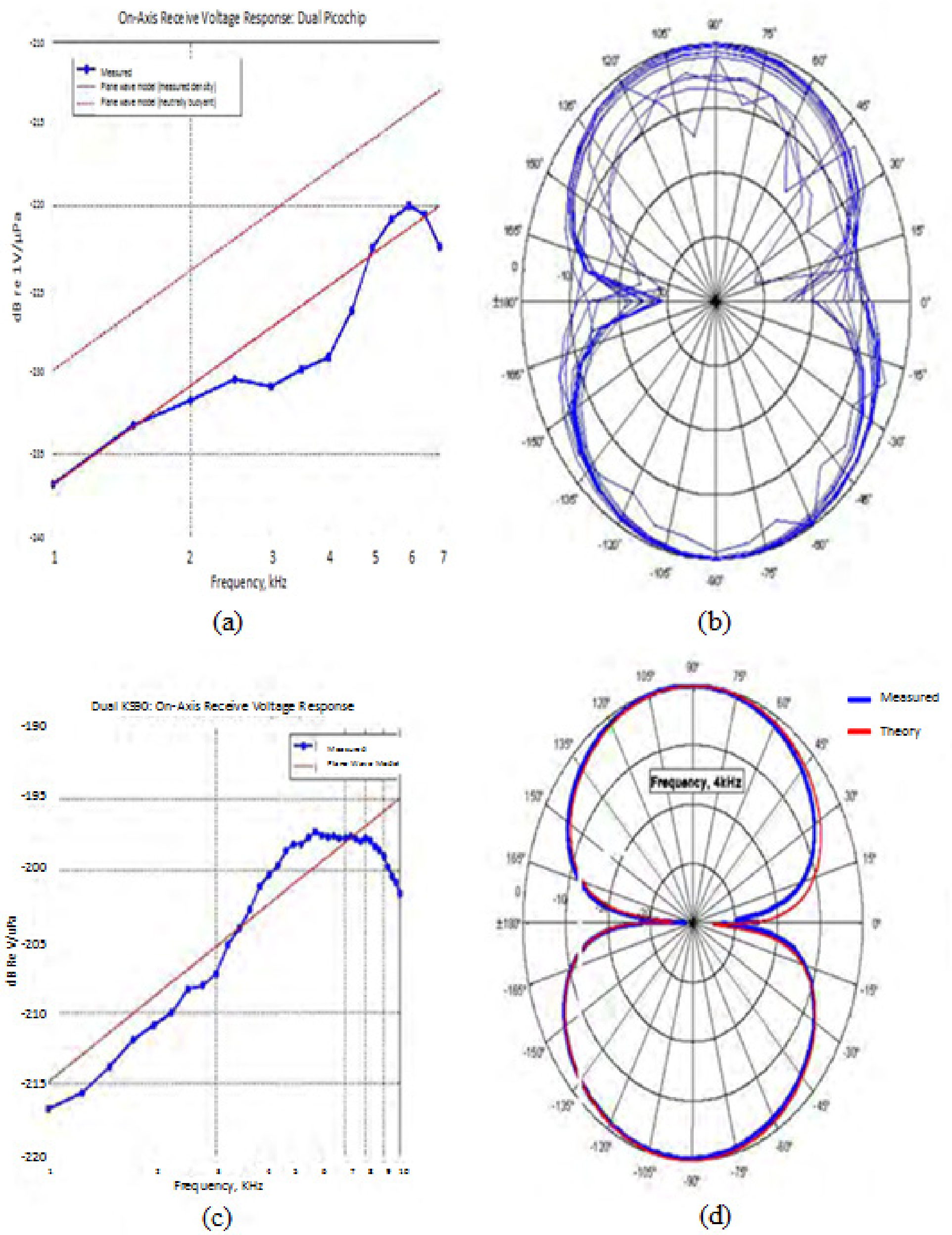

(a) (b)

(c) (d)

Figure 2. MKI and MKII hydrophone characterizations. Adapted from [17]. (a): MKI frequency response from 1 to 7 kHz, (b) MKI directivity patterns from 1 through 7 kHz in 500 Hz increments, (c) MKII frequency response from 1 to 10 kHz, and (d) MKII directivity patterns at 4 kHz.

2. Hydroflown. This vector sensor combines a Microflown sensor and an omni-directional pressure-based hydrophone [13] and [18]. The Microflown device is based on a mass-flow sensor, measuring particle velocity using two parallel platinum wire resistances [19]. The directional response of this design is shown in Figure 3, where it is possible to observe the characteristic 8-pattern obtained with vector sensors.

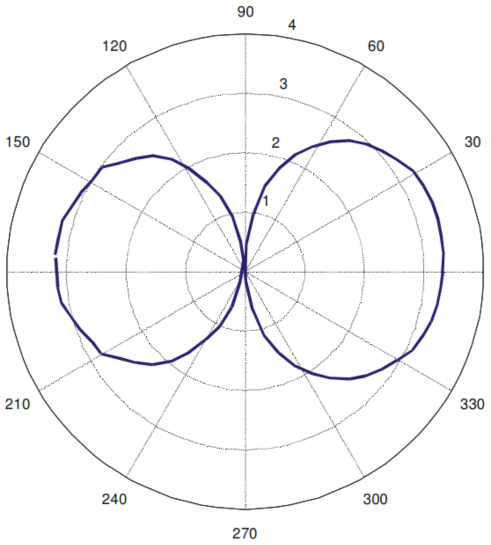

Figure 3. Hydroflown hydrophone directivity pattern at an unspecified frequency. Source: [20].

3. Wilcoxson vector sensor. The vector sensor shown in Figure 4 uses three PMN-PT crystal-based axial accelerometers, a PZT omnidirectional hydrophone, and a 4-channel amplifier. Designed in accordance with key requirements established by the U.S. Navy. It has a frequency range from 3 Hz to 7 kHz, as shown in Figure 5, output frequency response sensitivity of -174 dB re 1 V/μPa, and the characteristic 8-pattern of a vector sensor. Its length is 71.3 mm and its diameter is 40.7 mm [21] and [22].

Figure 4. Wilcoxon vector sensor VS-209. Source: [23].

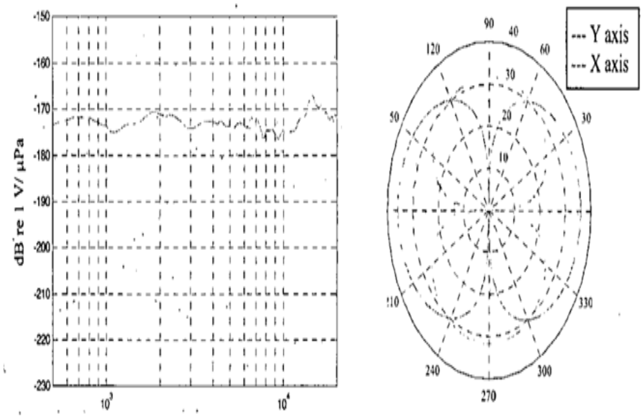

Figure 5. Wilcoxon sensor characterizations. Source: [21]. Frequency response from 400 Hz to 11 kHz and directivity patterns at 7 kHz.

4. SV-1 and SV-2. This kind of vector sensor, shown in Figure 6, bases its working principle on measuring the particle velocity of a neutrally buoyant object that is displaced by the incidence of an acoustical wave. These sensors are constructed by mounting a velocity-sensitive device inside a rigid, spherical shell.

   SV-1 "was used as an absolute standard for the calibration of transducers in the audio frequency range." SV-2 was "used in conjunction with a pressure hydrophone … to determine the acoustic characteristics of the bottom." For SV-2 "the magnetic structure of the pickup is rigidly attached to the case and a light coil is suspended in the air gap". [24]

5. The sensitivity and directivity patterns of both versions of this sensor are shown in Figure 7

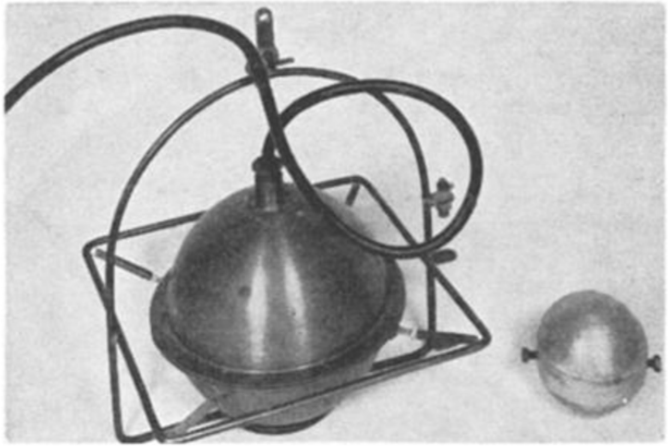

Figure 6. SV-2 and SV-1 hydrophones. Source: [24].

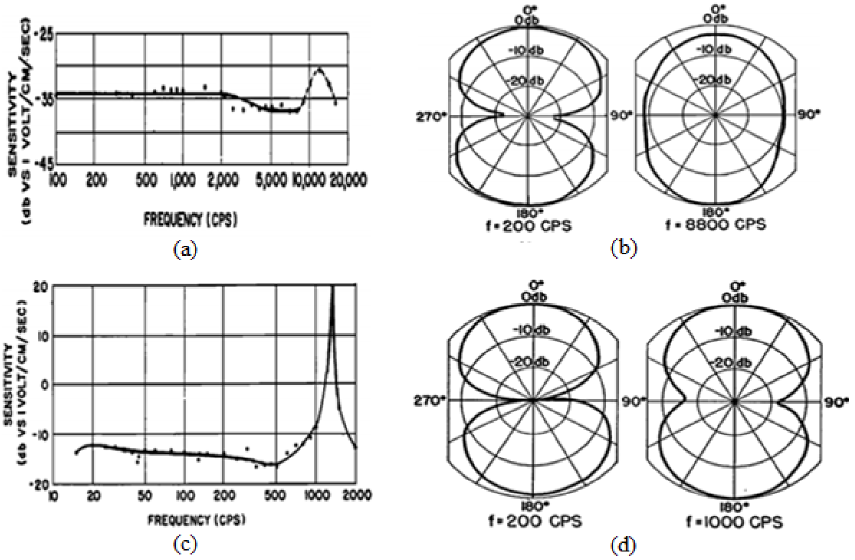

Figure 7. SV-1 and SV-2 hydrophone characterizations. Source: [24]. (a) SV-I frequency response from 100 Hz to 20 kHz, (b) SV-1 directivity patterns at 200 Hz and 8.8 kHz, (c) SV-2 frequency response from 20 to 2 kHz, and (d) directivity patterns at 200 Hz and 1 kHz.

4. MEMS Hydrophones

MEMS hydrophones used for underwater detection consist of microfabricated sensors that transduce underwater sound by being in direct contact with the fluid or sensing the vibration caused by the acoustic wave. The hydrophones here summarized for comparison are bioinspired sensors, neutrally buoyant accelerometers, and piezoelectric transducers:

1. Bioinspired MEMS hydrophones. In the case of adapting biological structures to MEMS, it is possible to emulate systems that nature has reached through evolution. Some of the current trends of research can be summarized as follows:

   One of the biological models adapted to MEMS is the fish lateral line tube organ. A T-shape vector sensor uses a pair of long cantilever beams with piezoresistors on its transverse sections, as shown in Figure 8. The deformation of the beams caused by an underwater acoustic signal induces a resistance variation that is related to the direction and pressure of the wave [25]. In Figure 8, The sensor NUC1 achieves a sensitivity between—181 dB and—170 dB at 1 kHz and an 8-shape directivity pattern, as is shown in Figure 8.

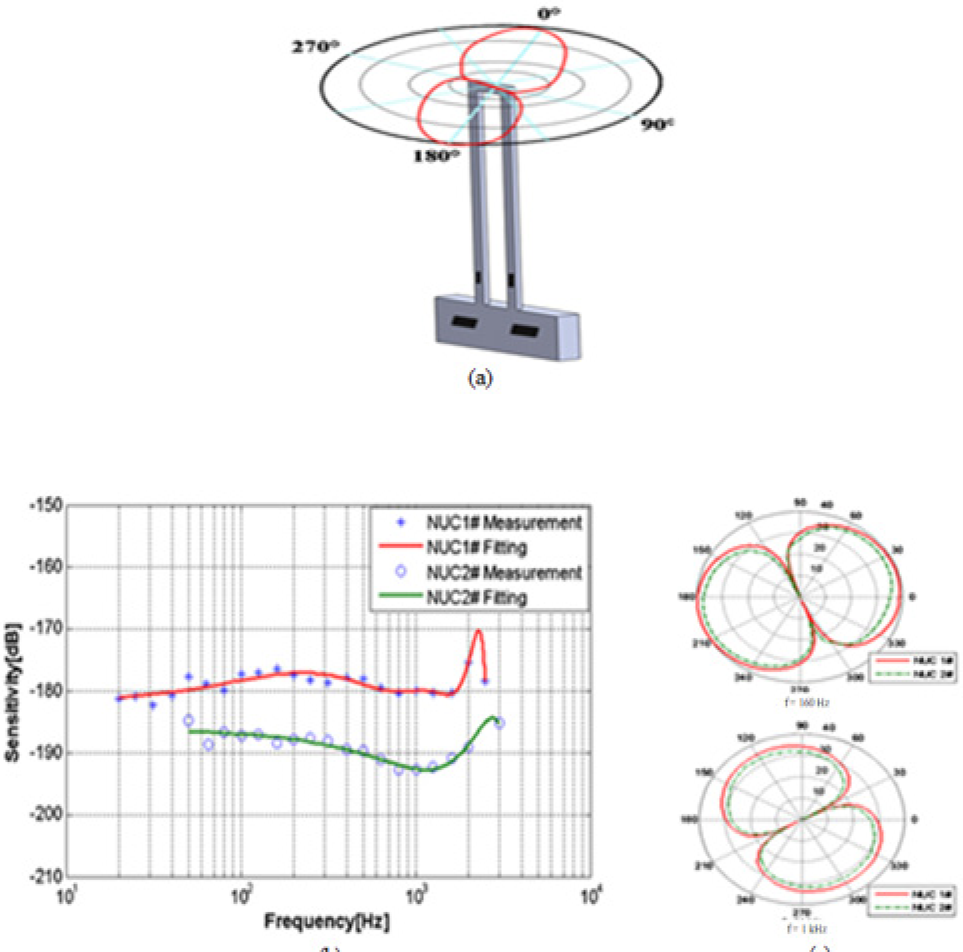

(a) (b) (c)

Figure 8. T-shape vector sensor characterization. Source: [25]. (a) Sensor diagram, (b) frequency response from 20 Hz to 3 kHz, and (c) directivity patterns for 160 Hz and 1 kHz.

The bionic vector sensor is a solitary vertical cylinder that rests in the center of a four-perpendicular-beam structure. Acoustic waves incident to the solitary vertical cylinder create compressive and tensile stresses in the structure. These stresses are transduced to voltage by the piezoresistive effect of resonant tunneling diodes. This sensor reaches a sensitivity of -184.6 dB at 1 kHz and 8-shape directivity pattern, shown in Figure 10.

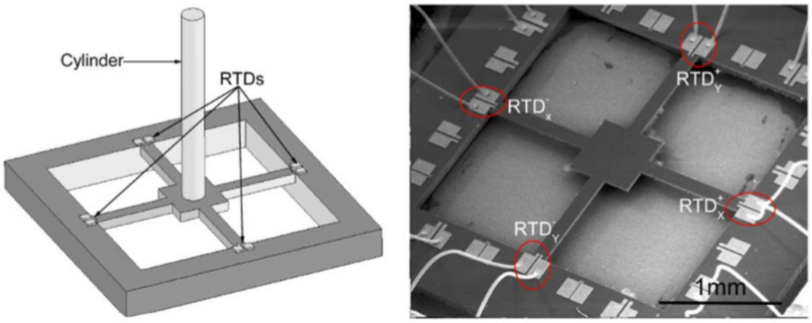

(a) (b)

Figure 9. (a) Bionic sensor structure and (b) SEM photograph of the four-beam structure. Source: [26].

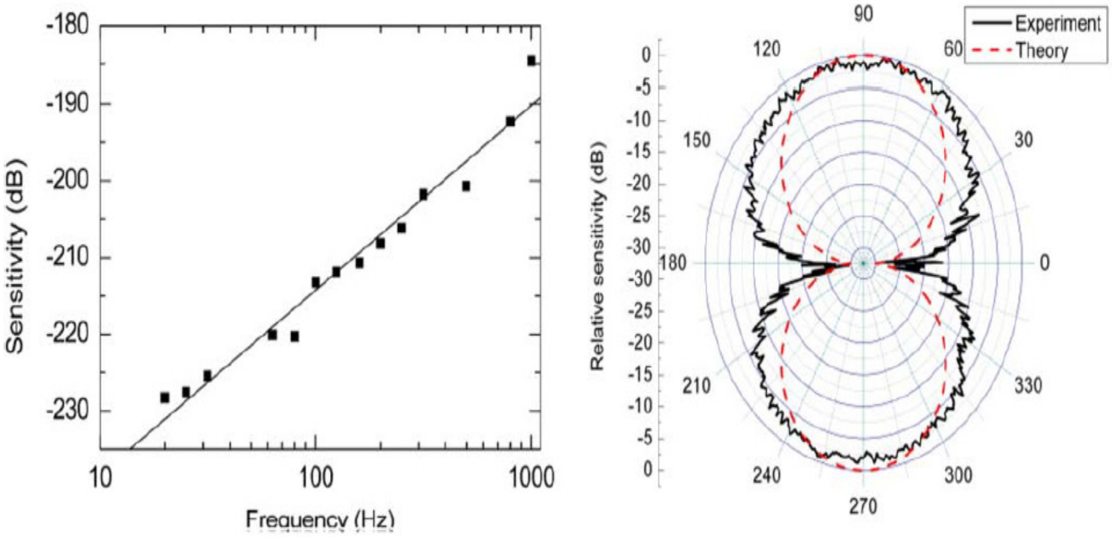

(a) (b)

Figure 10. Bionic vector sensor. Source: [26]. (a) Frequency response from 20 to 1 kHz and (b) directivity pattern at 125 Hz.

2. MEMS Accelerometer Sensors. The device shown in Figure 11 is micromachined from a silicon-on-insulator (SOI) wafer with “interdigitated capacitive comb fingers for electronic readout.” Sensors are typically operated in neutrally buoyant configuration to measure particle velocity of fluid. This sensor exhibits sensitivity up to -208 dB at 500 Hz and an 8-shape directivity pattern as illustrated in Figure 12 [9].

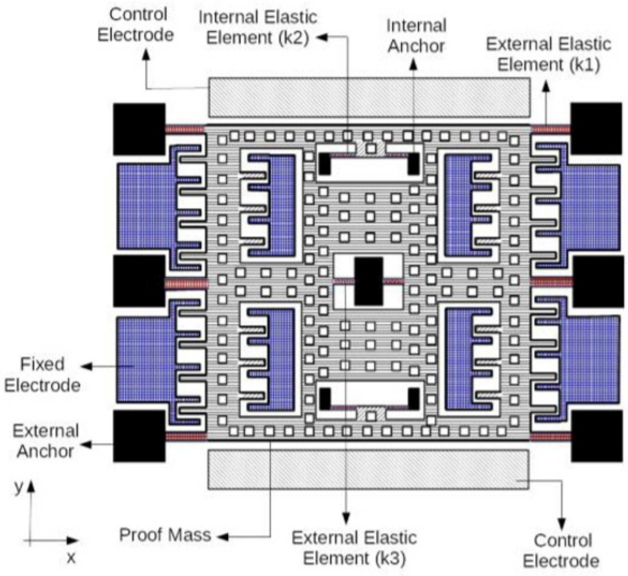

Figure 11. Top view of MEMS accelerometer. Source: [9].

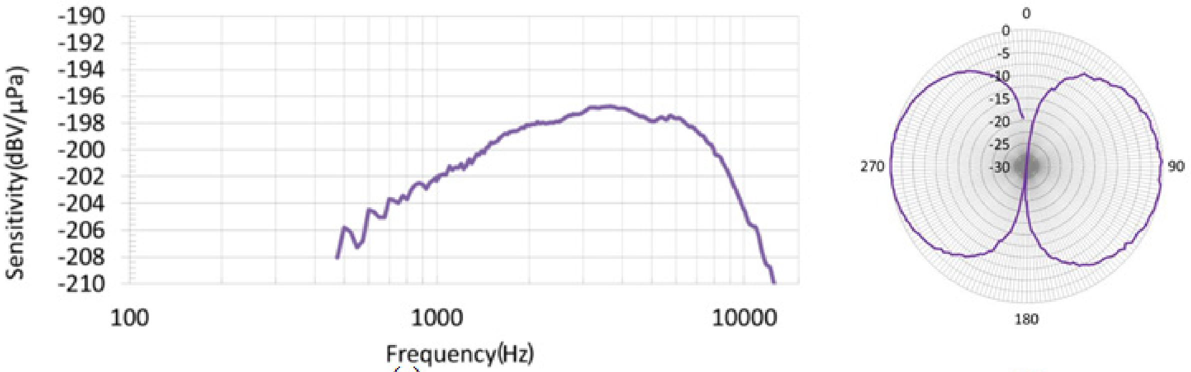

(a) (b)

Figure 12. Broadband MEMS accelerometer sensor. Source: [9]. (a) Frequency response from 500 Hz to 10.5 kHz and (b) directivity pattern at an unknown frequency.

3. Piezoelectric MEMS hydrophones. Advances in piezoceramic materials allow for the fabrication of MEMS hydrophones with a higher sensitivity, at a lower cost, and in bigger production volumes. One of the devices designed is "micro-machined piezoelectric hydrophone with hydrostatically balanced air backing" [27] as shown in Figure 13. This sensor is built using a thin PZT membrane that is air backed using micro

channels to compensate the outer pressure once the sensor is submerged. The whole sensor is built using micromachining processes and shows an omnidirectional behavior [27].

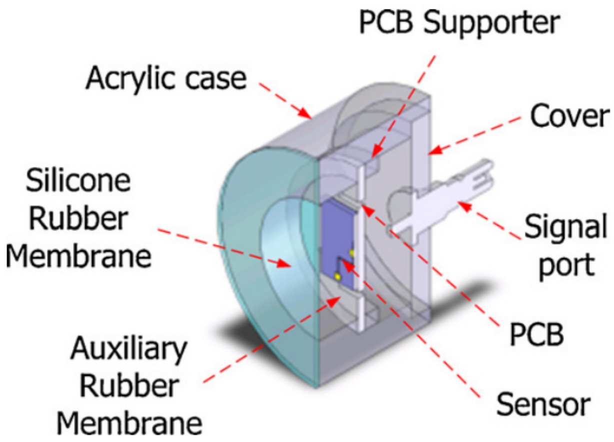

Figure 13. Cross section of the air-backed piezoelectric hydrophone. Source: [27].

B. MEMS SENSOR RESEARCH AT NPS

Bioinspired MEMS acoustic sensors based on the hearing system of the *Ormia Ochracea* parasitic fly have been developed at NPS. The physics of the fly's hearing organ was described by Miles et al. [4]. The detection mechanism is based on coupling of eardrums to enhance interaural time and level differences. The main advantage of this system is the ability to determine the direction of a sound with size smaller than the wavelength of sound it detects. Sensors are typically built using MEMS technology to mimic the fly's hearing system [9]. Figure 14 shows typical sensor geometry and two vibration modes (bending and rocking) under sound excitation.

One of the transducing modes converts the vibration of the mechanical structure to an electrical signal through a capacitive readout [9]. The mechanical motion of the sensor is excited by incident sound with a frequency corresponding to the resonant frequency of the vibrational mode at which the sensor was designed. The bending mode is at a higher natural frequency in comparison to the rocking mode. In the bending motion, both wings oscillate in phase while the rocking wings oscillate out of phase, as depicted in Figure 14. The frequency of the vibrational modes depends on the dimensions of the structure and stiffness of the material employed. The amplitude of oscillations depends on the intensity and direction of the incident sound.

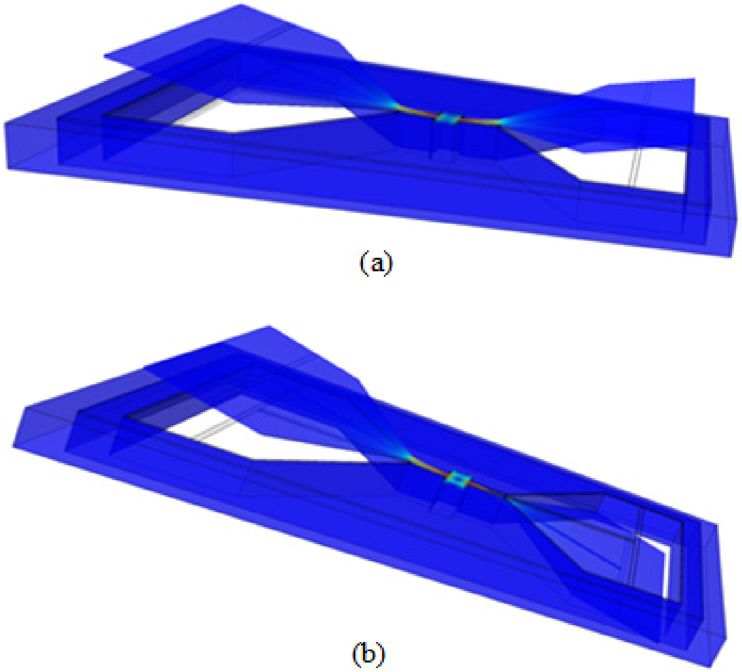

Figure 14. (a) Bending and (b) rocking mode of the two-wing version of MEMS acoustic sensor

This sensor has been deeply studied using finite element computational tools (FE) software and fabricated using a commercial foundry (MEMS Cap). Air and underwater prototypes have been characterized at NPS facilities and third-party laboratories. Two main characteristics are narrow-band low-frequency operation and first-order directionality.

The details of the work can be found in papers [28], [29], and [30]; PhD dissertations [31] and [32]; and masters theses [33], [34], [35], [36], and [37].

Three previous research studies have been conducted ([38], [39], and [40]) that explored the underwater capabilities of the sensor. These studies have shown good adaptability of the sensors to operate in a nonconductive fluid while retaining the operational characteristics observed in air, mainly its directional response, as shown in Figure 15. Some of the features that modify the behavior of the response for underwater operation are still under investigation.

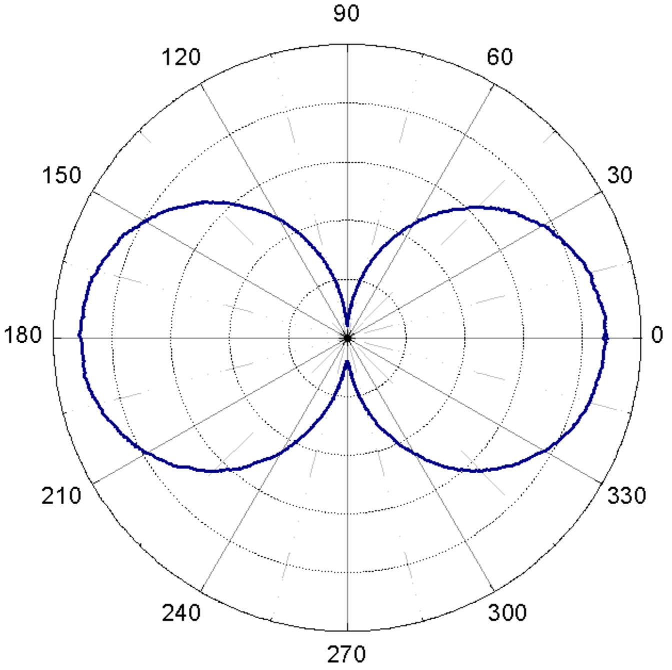

Figure 15. Directional response of the Gen 1–10 sensor as measured at TRANSDEC. Source: [40].

The advantages of the MEMS acoustic sensor under development to adapt it in towed arrays are: due to its small size and weight, it can be useful as the main sensing element on thin-line towed arrays; due to its narrow band of operation, it can inherently filter the frequencies caused by turbulence; and due to its directional response, it solves by itself the left-right ambiguity. According to the characteristics of the sensors for thin-line towed arrays reported by [6], [7], and [8], this option is much smaller and with vector capabilities that can improve the left-right ambiguity resolution. Compared with vector sensors reported by [17], [20], and [21] it shows a smaller size and vector response similar to those reported for the directivity patterns at higher frequencies (4 and 7 kHz). Compared with vector MEMS sensors reported by [9], [25], and [26], it shows a smoother 8-pattern at similar frequencies. In comparison with the previous sensors described it shows a 30 dB peak sensitivity improvement at the frequency of resonance.

C. OBJECTIVE AND THESIS ORGANIZATION

The objective of this thesis is to compare the results between the simulations and real tests of the sensor and its underwater packaging, find an appropriate polyurethane with acoustical transparency for underwater packaging, and demonstrate the advances in micromachining capabilities in NPS.

The results obtained show agreement between simulations and real measurements. PMC-780 polyurethane showed underwater acoustical transmission without significant attenuation between 200 and 600 Hz. Micromachining capabilities of the sensor in the NPS clean room are close to building the first complete device.

Chapter I presents a review of the current technologies employed in thin-line towed arrays, vector sensors, and MEMS sensors. The vector MEMS sensor under research at NPS is compared with thin-line towed array and vector sensors.

Chapter II describes the third generation of the underwater MEMS acoustic sensor, its design using FE software, and the simulations of the frequency response of the underwater packaging.

Chapter III presents the experimental data used to characterize an underwater packaging looking for acoustical transparency properties for this application.

Chapter IV describes the fabrication process of the sensor using commercial foundry services. It also presents the in-house assembly process and preliminary tests, as well as the characterization results of the sensor in air using the anechoic chamber and underwater in the NPS water tank and Transducer Evaluation Center (TRANSDEC) facility.

Chapter V presents the preliminary results of the microfabrication processes performed in the cleanroom to fabricate a Generation 1 underwater MEMS acoustic sensor.

Chapter VI presents the conclusions and some ideas for future work.

II. SENSOR DESIGN WITH FINITE ELEMENT SIMULATION

The first step in fabricating a MEMS acoustic sensor is to determine its characteristics, either analytically or using computational tools. Due to the complexity of the mechanical structure, a computational approach for simulating it was chosen. The software employed was COMSOL Multiphysics®. Through FE modeling, it is possible to determine its characteristics before fabricating it.

The analysis of the sensor has evolved from a mathematical model inspired by the acoustic organ of the *Ormia Ochracea* parasitic fly developed by Miles et al. [4] to a MATLAB graphical model presented by Shivok [33] in his Appendix A. This approach was followed by several COMSOL simulations that added physics considerations as described by Harrison [35]. Once the FE design accurately described the operation of the sensor in air, it was adapted for designing underwater sensors. The thermoviscous acoustics module in COMSOL was employed to account for the interaction between the mechanical structure of the sensor and surrounding fluid [40].

A. UNDERWATER MEMS ACOUSTIC SENSOR EVOLUTION

The MEMS acoustic sensor implemented originally for underwater application was based on a single-wing architecture. With this version, it was possible to measure a 9 mV/Pa sensitivity in the frequency of interest [40] and a directivity index (DI) similar to the one obtained by using two omnidirectional elements under the two-element interferometer configuration that produces a cosine dependence beamforming [2]. This DI measured at the bending resonant frequency of the sensor is shown in Figure 15, as corroborated at TRANSDEC and reported by [40].

The one-wing configuration (denominated generation 1) did not excite rocking mode, and it showed a smooth and symmetric directional response at a resonant frequency equivalent to that of the bending mode [40]. The drawback of this design is its fragility during handling; it was necessary to be extremely careful during manipulation, assembly, and testing [39] due to rigid connection of the wing to the substrate.

The two-wing concept was successfully tested in air and its potential for underwater operation explored [39]. The most recent design using the two-wing configuration for underwater operation is generation 3. The differences between generations 2 and 3 are: 1) changing the spacing between comb fingers from 10 to 5 and 2.5 µm and 2) changing the length of the bridge from 0.75 mm to 1 mm. The purpose of these changes was to study the increase in sensitivity; reduce its fragility during manipulation, assembly, and testing; and study the tuning of the resonance frequency.

B. SIMULATION OF SENSOR CHARACTERISTICS

The sensor was modeled in COMSOL using three different physics: pressure acoustics frequency domain interface (PA), solid mechanics interface (SM), and thermoviscous acoustics frequency domain interface (TA).

The three-dimensional model is shown in Figure 16. The sensor outline was first drawn in 2D and extruded to form the 3D structure as shown in the middle section of the figure. Only half of the 3D structure is shown due to symmetry of the sensor geometry. Next, a spherical structure with a sound-absorbing layer that represents the operational environment was built. The panel on the right of the figure shows the sections where different physics are applied.

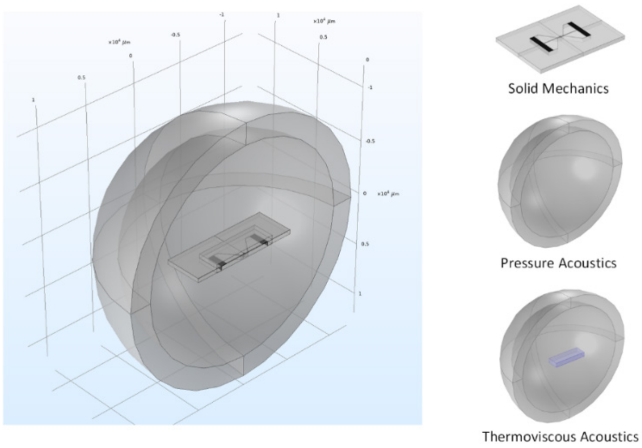

Figure 16. Constituting geometries of the 3D model, indicating the physics evaluated for each section.

The next step of the simulation is to assign materials to different sections under the following considerations:

- MEMS acoustic sensor: Anisotropic silicon with the stiffness matrix as given by [41], [39], and [40] was used for the structure of the sensor including the comb fingers. The region where the pad metal was deposited (see yellow region in Figure 17) was modeled with anisotropic silicon with higher density to take into account the added mass of gold on silicon.

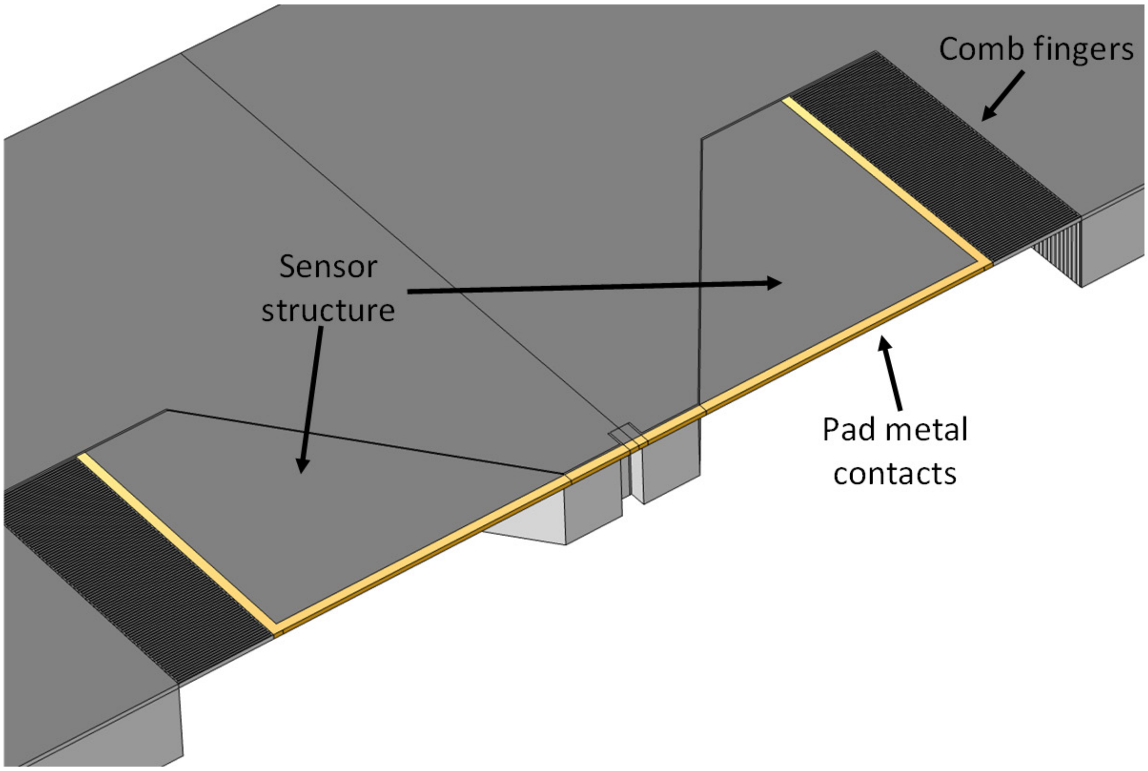

Figure 17. Half of sensor geometry, indicating which sections are assigned with anisotropic silicon.

- Operational environment. Air and cSt-1 oil, for simulating the frequency response of the sensor before and after submerging it.

- Underwater packaging. PMC-780 or Flexane-80 using as Young’s Modulus the values reported in Chapter III. For the density 1,046.025 [42] and 1,018.55 [kg/m^3] [43], respectively, and for the Poisson's ratio 0.394 for both. The three-dimensional model of the underwater packaging is shown in Figure 18.

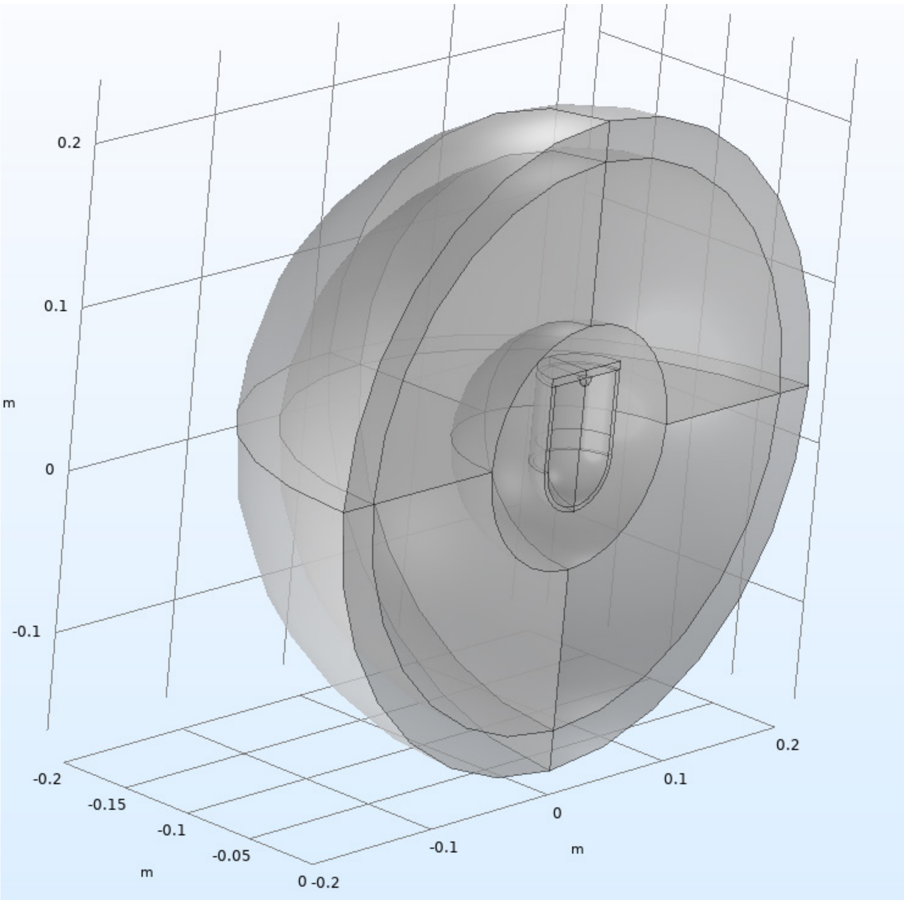

Figure 18. COMSOL geometry with a 3-mm-thick boot.

Once the 3D model was established, it was necessary to add the physics with appropriate boundary conditions. The physics involved in this simulation as described earlier are PA, SM, and TA. The PA physics are assigned to the operational environment represented by a sphere with a perfectly matched layer (PML). The objective of the PML is to establish a free-field condition to avoid reflections of the sound wave from the boundaries of the sphere [35]. The incident sound wave was implemented using background pressure field option within PA.

The TA interface is assigned to a small rectangular section that surrounds the sensor, as can be seen in Figure 16. As explained in [40], the TA model takes into account viscous and thermal losses of the acoustic wave traveling through the fluid. Lastly, SM physics are added to the simulation model to determine how the sensor responds to sound. In order to reduce computational time, only half of the sensor geometry was used in the simulation with help of symmetry boundary condition to represent the other half.

The next step is to add the couplings between different physics used in the simulation. The couplings needed were acoustic-thermoviscous acoustic boundary (ATAB) and thermoviscous acoustic-structure boundary (TASB), which can be introduced with the options available within the Multiphysics option.

The following step was to build the mesh for simulation. This is a crucial part of the process, because it determines the computational load and consequently the time the simulation takes. The mesh points have to be properly placed in order to optimize the accuracy and reduce the calculation time. Some of the domains need an extremely fine mesh like the comb fingers or bridge of the sensor, while others like the environment just need a coarse mesh.

After building the mesh, it is necessary to select and configure the studies. The approach for this step consisted of assigning the correct type of study for obtaining the desired parameters. In this case, we applied a frequency domain analysis, configuring a parametric sweep for some of the variables and a material sweep employing the material switch option.

Finally, the computation was executed and sometimes it was necessary to change the solver type to reduce the relative tolerance. It was observed that changing the solver from PARDISO to MUMPS improved the success rate of the simulations and eliminated a recurrent problem where the relative tolerance exceeded error was shown.

The simulation was executed in three stages: simulation of sensor 1) in air, 2) immersed in a fluid, and 3) underwater packaging immersed in a fluid.

C. MEMS ACOUSTIC SENSOR IN AIR

The computational model was configured with the considerations previously described, making it possible to simulate 1) frequency response and 2) directional response of the sensor. In this simulation, background plane acoustic field amplitude was set to 1 Pa and direction was set to 45 degrees from the normal to the sensor surface. In addition, the direction could be varied by assigning it as a variable, theta.

Additionally, the damping effects were taken into account by adding viscous loads to appropriate boundaries of the 3D model. These damping effects are theoretically calculated due to the airflow between the comb fingers as well as the mass of air that the surface of the wing has to displace as it moves according to formulas given by Klose [44] shown in Equations 2.1 and 2.2 and empirical drag coefficient given by Davis [45].

$$\vec{F}_{Couette} = -\eta \frac{A_s}{g} \vec{v} \tag{2.1}$$

$$\vec{F}_{drag} = -\frac{\vec{v}}{|\vec{v}|} c_d \rho_m |\vec{v}|^2 \frac{A_p}{2} \tag{2.2}$$

Where $F_{couette}$ is the drag force between comb fingers, η is the dynamic viscosity, A_s the comb finger area, g the trench width, v the velocity of the moving comb fingers, F_{drag} the damping force due to the mass loading, c_d the empirical drag coefficient, ρ_m the air density, and A_p the wing area.

This simulation was carried on exclusively in air and without considering the underwater packaging. This approach has been perfected during the last 10 years through numerous comparisons with measurements carried out in the NPS anechoic chamber.

In Figure 19, the frequency response of the sensor is shown by plotting the displacement amplitude of the wing with respect to the frequency of excitation. It is possible to observe the first resonant mode of the sensor, corresponding to the bending at 1580 Hz.

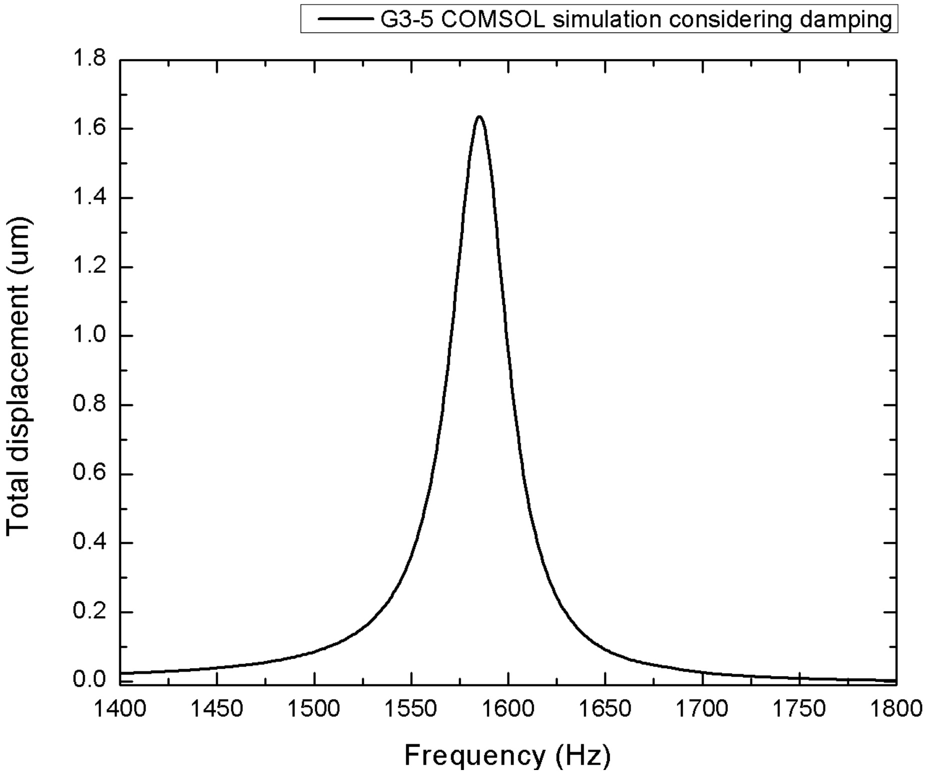

Figure 19. Displacement amplitude of the tip of the wing.

Once the frequency response has been calculated, it is possible to evaluate the directivity pattern of the sensor by appropriate computational tools within COMSOL. This directivity pattern is achieved by adding to the study section of the simulation a parametric sweep that will vary the "theta" variable previously defined, while keeping the frequency at a desired value. The results of this simulation performed at bending resonance frequency are shown in Figure 20. In Figure 20, directional response of the sensor shows a cosine pattern due to interaction of sound from both sides of the wing as described in [32].

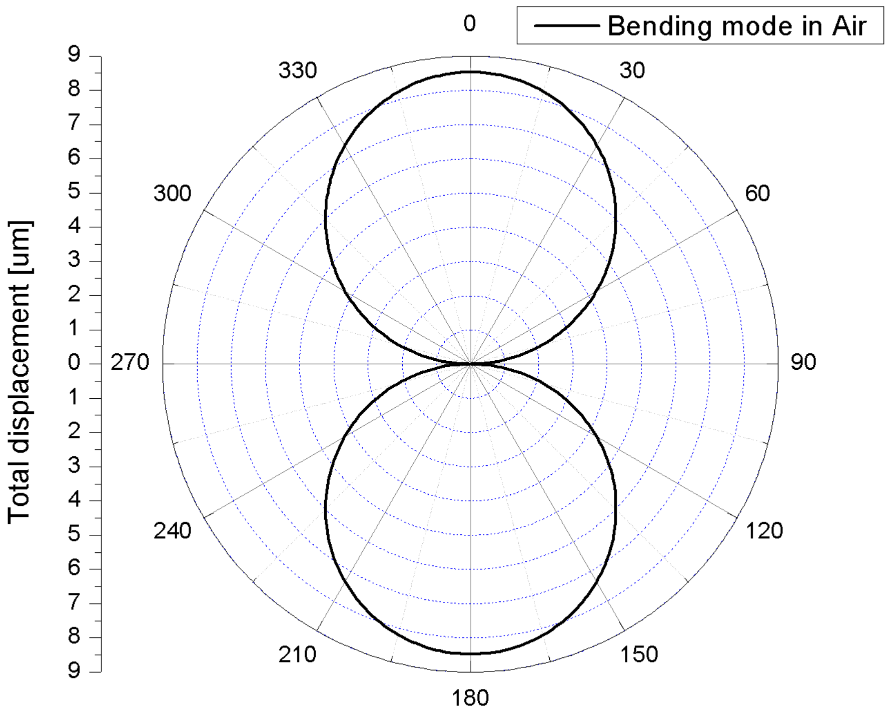

Figure 20. Simulated directivity pattern of the MEMS sensor in air at 1629 Hz

D. MEMS ACOUSTIC SENSOR IN OIL

The simulation was carried out similarly to that in air described in the previous section with the difference of replacing the air with silicone oil. The damping effects were incorporated by adding the actual comb fingers to the wing instead of applying boundary conditions as discussed in Section C of this Chapter. The TA interface was able to calculate the losses produced by the movement of the fluid through the space between fixed and moving combs as well as the drag damping due to displacement of fluid as the wings oscillate. This approach failed to generate adequate damping when the sensors operated in air.

This simulation was carried with sensor immersed in silicone oil and surrounded by water without incorporating the effects of sensor housing. Figure 21 shows the simulated data with 1 CsT silicone oil.

It can be seen in Figure 21 that resonant frequency shifted from 1580 Hz in air to 240 Hz in oil and there was a significant reduction of the amplitude of vibration from 1.6

μm in air to 6 nm in oil. The reduction of the resonant frequency and attenuation of the rocking mode in comparison to air is due to mass loading on the wings as a result of the oscillation in a dense fluid.

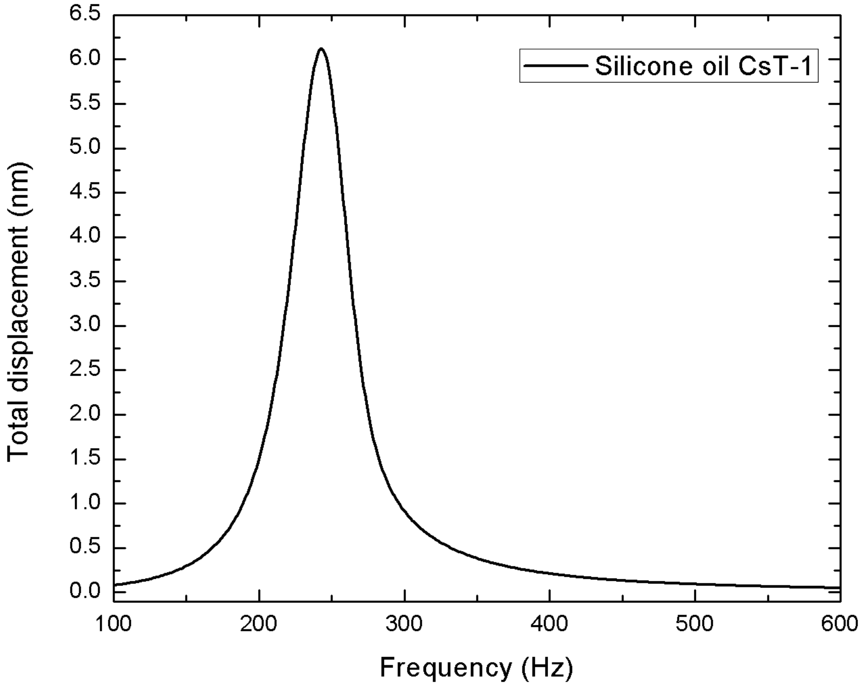

Figure 21. Frequency response of the MEMS acoustic sensor simulation using oil.

Once the simulation was executed, it was possible to identify the frequency of the resonant mode and simulate its directional response by varying the direction from which the acoustic wave was coming. This was accomplished by performing a parametric sweep by varying the incident angle of sound while keeping the frequency at 240 Hz. The results show the expected cosine directional response as illustrated in Figure 22.

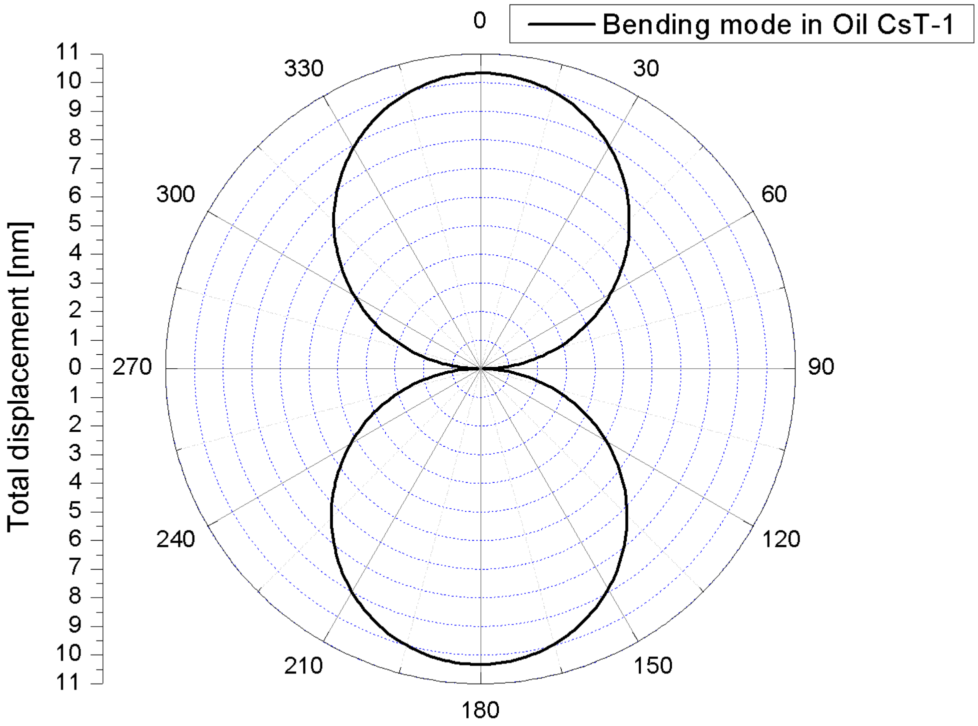

Figure 22. Simulated directional response of the sensor at 240 Hz (bending resonant frequency).

E. SIMULATIONS OF RESPONSE OF BOOT

In earlier experiments carried out using generation 1 sensors [40], it was observed that there were additional resonant responses of the sensor away from the expected ones based on simulations. This may be due to the interaction of the boot with the incident sound, which was ignored during the previous simulations. As a first attempt, the response of the boot to incident sound was simulated using COMSOL. The simulations were carried out in the frequency domain with parametric sweeps to vary damping, Poisson's ratio, density, and Young's modulus.

Figure 23, Figure 24, Figure 25, and Figure 26 show the peaks of frequency response of oscillation of the boot as a function of frequency with varying damping, Young's modulus, Poisson's ratio, and density, respectively. In the simulations the parameters that were not varying were kept constant as follows: density at 1020 [kg/m^3], Young's modulus at 55400 [Pa], Poisson ratio at 0.394 and loss factor at 0.1.

It can be seen in Figure 23 that the highest amplitude lies in the frequency range from 150 to 250 Hz. As expected, higher damping (larger loss factor), reduced the amplitude of oscillation of the boot.

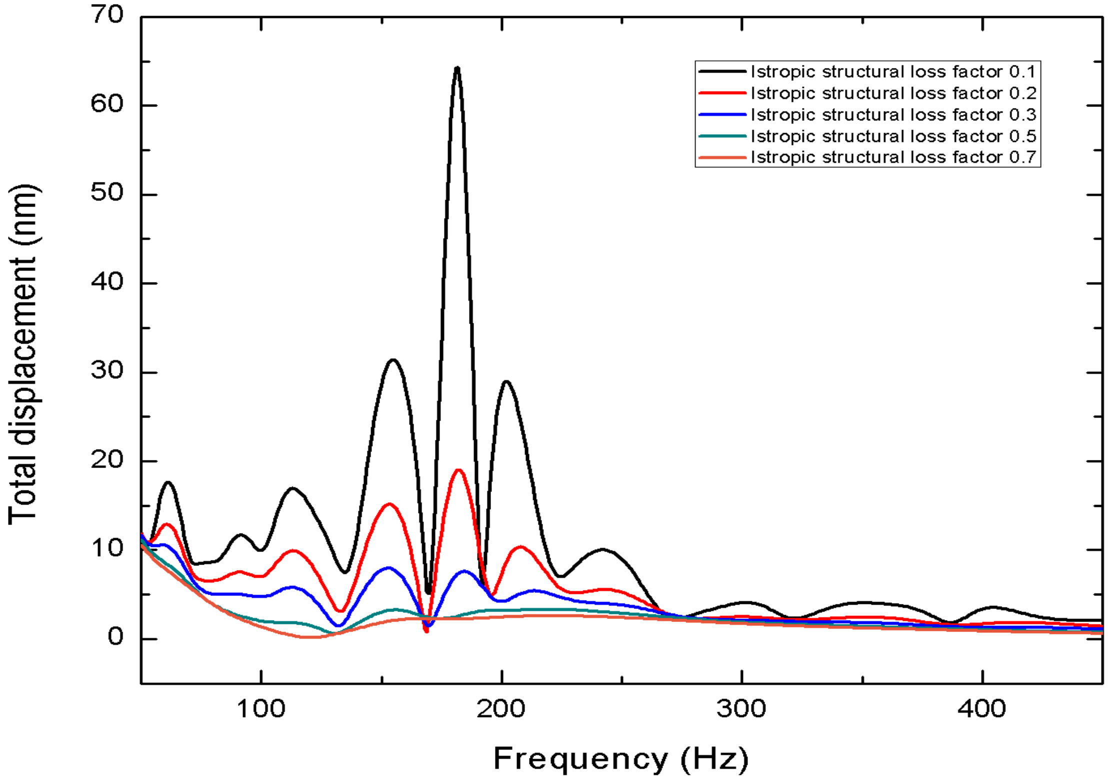

Figure 23. Simulated frequency response of the boot varying the isotropic structural loss as damping parameter.

According to the results of the simulations presented in Figure 24, Figure 25, and Figure 26 it is possible to observe a shift in frequency toward higher values as the Young's modulus and Poisson's ratio are increased, and a shift in frequency toward lower values as the density is increased.

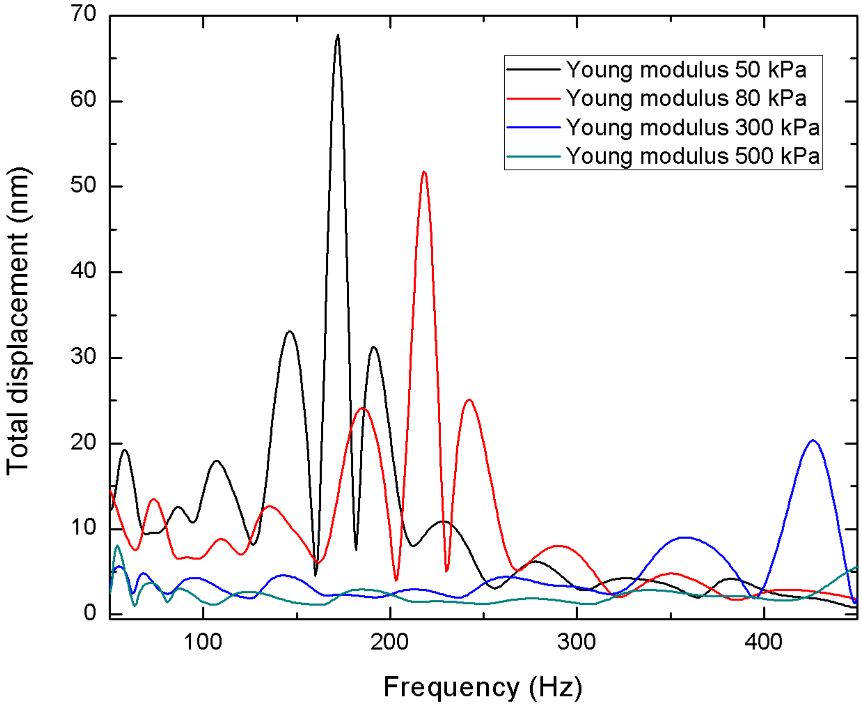

Figure 24. Frequency response simulations varying Young’s modulus of the material

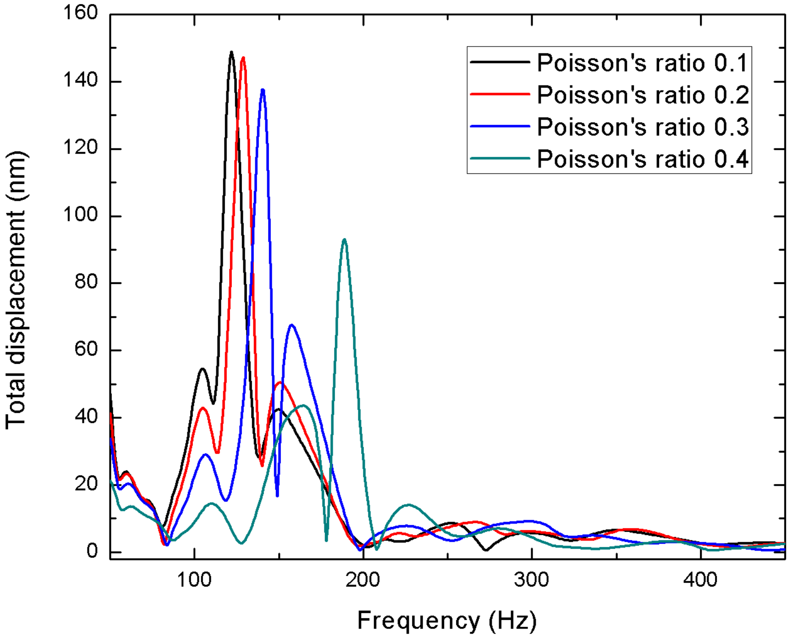

Figure 25. Frequency response simulations varying the Poisson’s ratio of the material

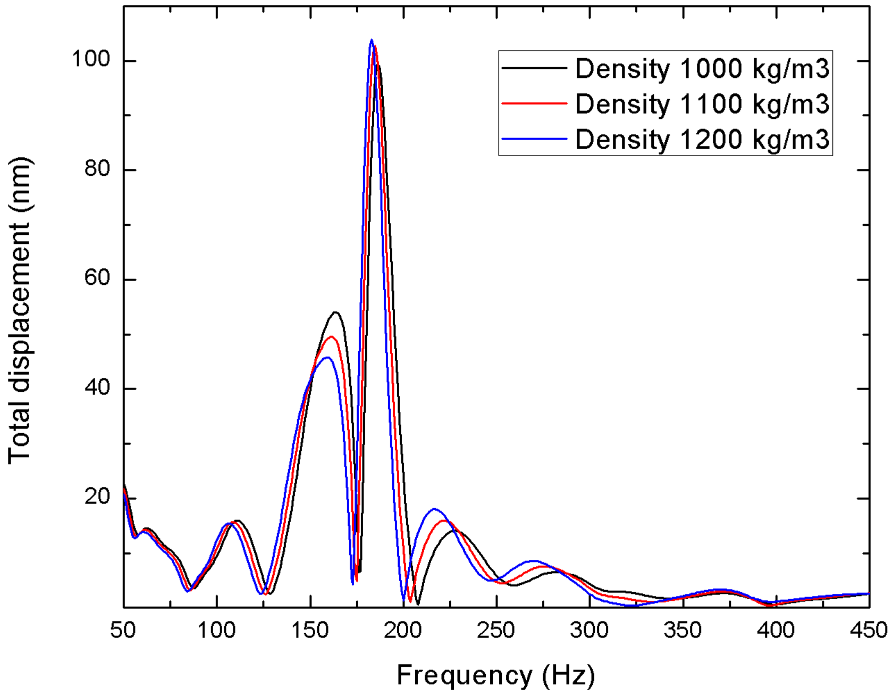

Figure 26. Frequency response simulations varying density of the material

The comprehension of the behavior of the underwater packaging material could represent a valuable asset for future designs, making it possible to design a boot to enhance response of the sensor by matching its resonance with that of the MEMS acoustic sensor.

THIS PAGE INTENTIONALLY LEFT BLANK

III. UNDERWATER PACKAGING

The housing used for mounting the underwater sensor (boot) was suspected to be causing deviations of sensor response from the expected behavior [40]. These deviations are potentially related to the materials employed, presence of air bubbles in the material, and/or oil used for immersing the sensor. It was observed that the housing effects affected the frequency response and/or attenuated the signal at certain frequencies. Another important consideration is the rigidity of the attachment between the sensor and the housing, which according to the literature, defines the free or fixed boundary condition under which the sensor will operate [15].

A. BOOT PHYSYCAL TESTS

Previous sensitivity calibrations of the MEMS acoustic sensor carried at NPS water tank and TRANSDEC facilities showed unexpected variations of frequency response. Initially, inspections of the housing material under a microscope and measurement of its elasticity modulus were performed. These measurements were done to explore how the material characteristics affect the acoustic properties of the material. These inspections allowed identification of differences between molding techniques and material properties that influence the transmission coefficient of the boot. The identification of those differences will allow minimizing the boot effects on sensor characteristics.

1. Microscopic Inspection of the Materials

The comparison of different molding techniques employed in boot fabrication using DEVCON Flexane 80 urethane was performed. This comparison allowed identifying the formation of air bubbles in the walls of the boot. The bubble formation was primarily suspected as a cause of acoustical variations of sensor response reported by Da Re [40]. The presence of bubbles was confirmed by visual inspection using a digital microscope Olympus BX51 with camera DP71 and a 10X magnification lens. This inspection allowed us to observe bubbles in the inner section of the cured polyurethane.

The urethane samples molded using the first technique presented in Appendix A showed bubbles in approximately 20% of its cross section, as well as grooves and bubbles in the inner walls of the boot as can be observed in Figure 27. In contrast, the sample of a boot molded with the second technique mentioned in Appendix A did not show bubbles but just grooves in the inner walls of the boot, as shown in Figure 28.

According to Mennig and Stoeckhert [46], the presence of bubbles in the polyurethanes “could be product of the Carbon dioxide (CO_2) released during the reaction of the polyisocyanate and polyol, evaporation of solvents with low boiling points or expansion of inert gases that are dissolved or dispersed at least in one of the raw materials” [46].

This imperfections during the molding process can cause significant changes in the elasticity properties of the boot.

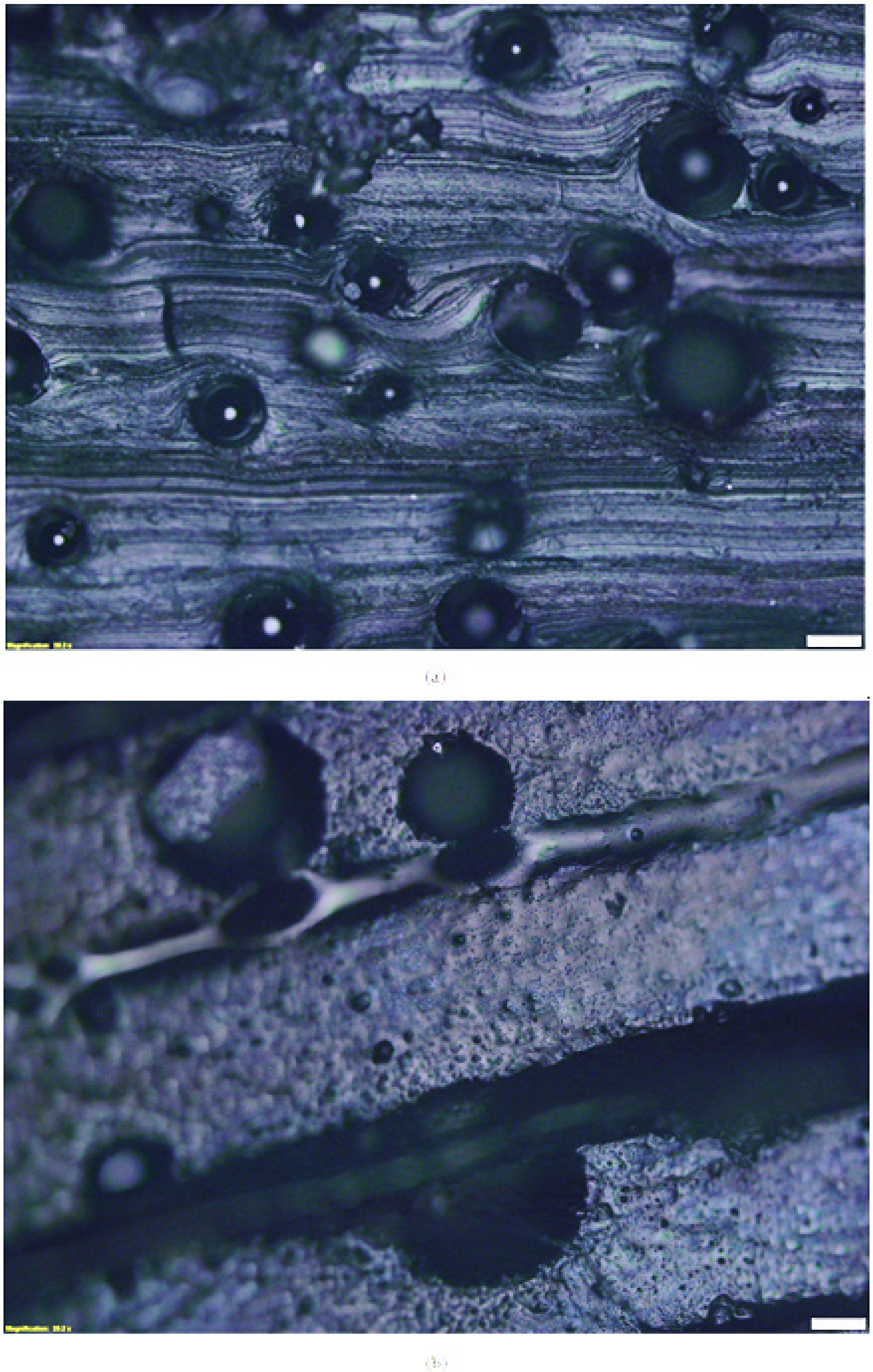

Figure 27. Polyurethane sample molded with technique 1. (a) Transversal section of a sample showing a significant amount of bubbles and (b) inner wall of the boot, showing the presence of grooves and bubbles.

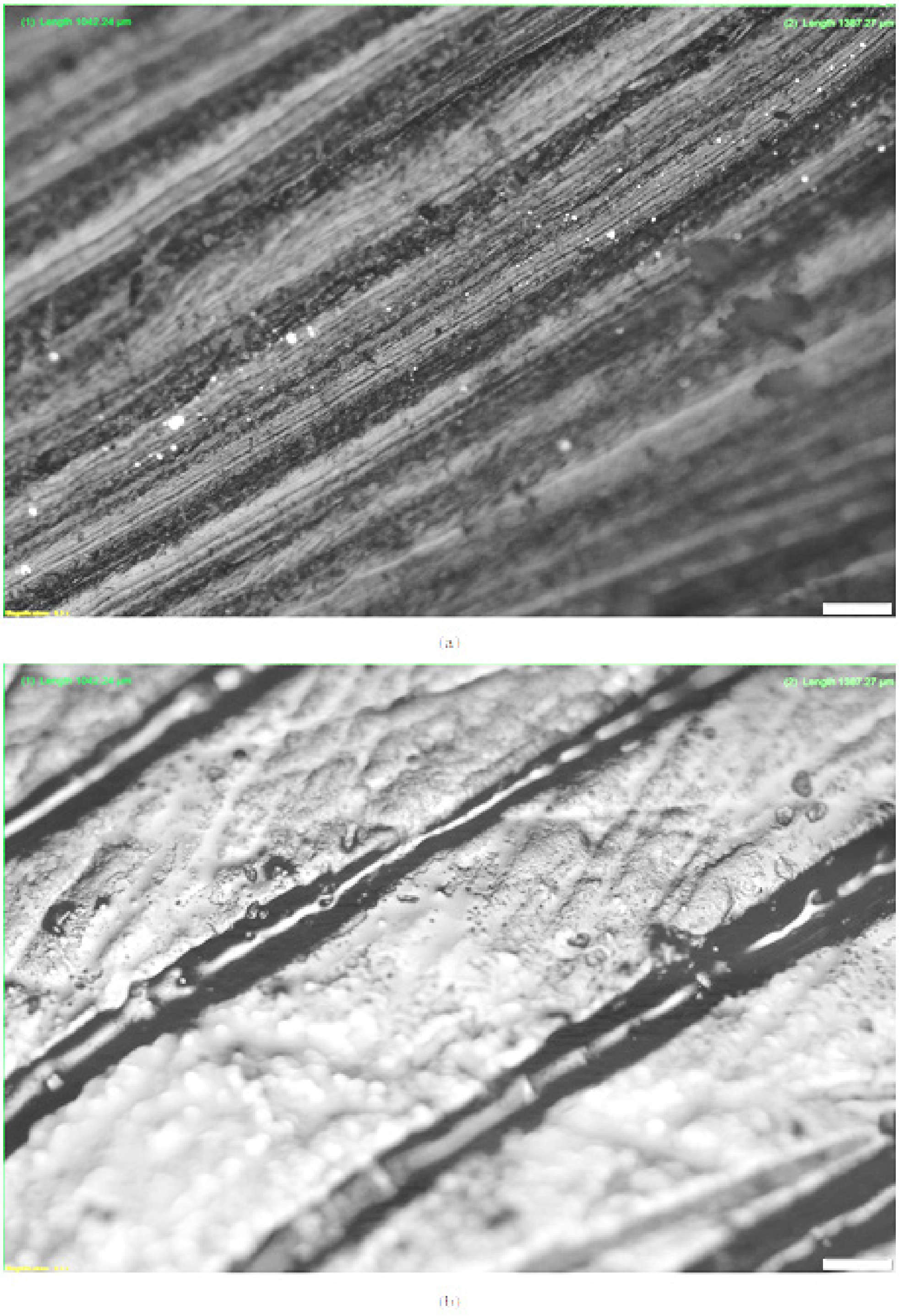

Figure 28. Polyurethane sample molded with technique 2. (a) Transversal section of a sample showing the absence of bubbles and (b) inner wall of the boot, showing no apparent formation of bubbles but the presence of grooves probably due to the finish of the filament with which the molds were 3D printed.

2. Elasticity Modulus Characterization

The materials characteristics were tested to compare the Flexane 80 and PMC-780 polyurethanes. These measurements were done to introduce the correct parameters into the COMSOL simulations, to compare the resonant frequencies of the boots. This comparison was intended to explain the behavior of the boot and the sound interactions in the inner volume of the boot.

Continuing the measurements and procedure described by Da Re [40], a mold for material sheets of 15 cm by 25 cm was manufactured. Two sheets each of Flexane 80 and PMC-780 were molded using the technique number two described in Appendix A. The sheets were cut in the desired shape using a hydraulic press and a specimen die. The elasticity modulus was measured using the Instron model 1000 tensile measurement system and the results are plotted in Figure 29.

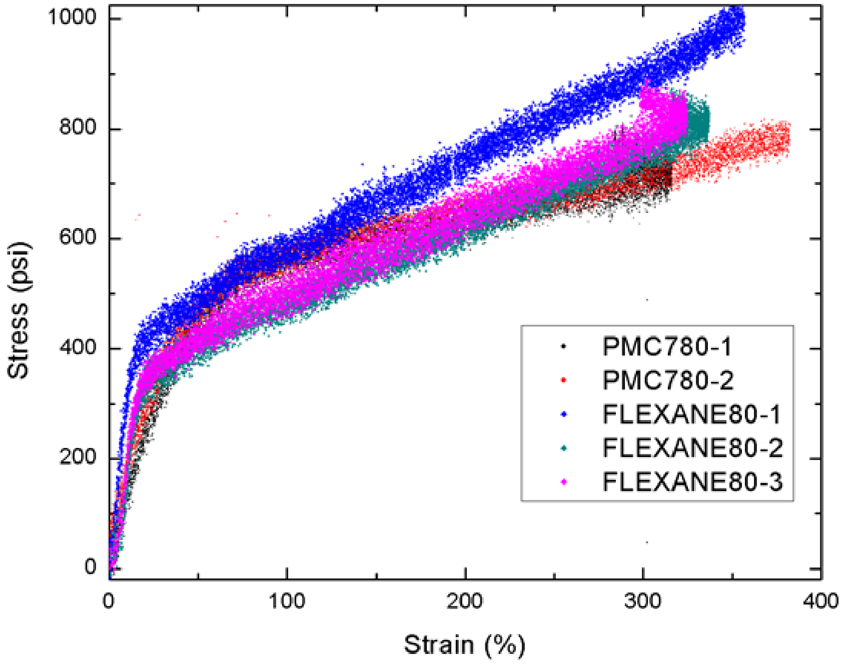

Figure 29. Strain vs. stress graphs obtained with Instron model 1000 tensile measurement system.

The elastic properties measured for the samples of Flexane 80 and PMC-780 are summarized in Table 1. The elastic modulus was calculated as the slope of the measured deformations in the elastic region, obtaining average elasticity modulus values of 55,400 and 67,500 N/m^2. The densities reported in the specification sheets of each material are 1018 and 1046 for Flexane-80 and PMC-780, respectively.

Table 1. Elastic properties of materials employed for molding the boots.

Sample	Material	Tensile ultimate stress measured (psi)		Tensile ultimate stress reported by manufacturer (psi)		Elastic modulus measured (psi)	
		psi	N/m^2 x10^6	psi	N/m^2 x10^6	psi	N/m^2 x10^3
Y-1	Flexane 80	1052.26	7.2	2100	14.5	9.91	68.3
Y-2		873.1	6.02			7.81	53.8
Y-3		890.2	6.14			6.41	44.2
Y-4	PMC-780	822.90	5.67	900	6.20	9.95	68.6
Y-5		817.12	5.63			9.63	66.4

B. BOOT ACOUSTIC CHARACTERISTICS

After observing unexpected features in the MEMS sensor response, it was decided to evaluate the effects of the boot on the sensor response. The response of a reference hydrophone was measured with and without the boot to determine sound transmission through the boot.

1. Design of the Experimental Mount for Acoustic Characterization

The unexpected variations were first reported by Da Re [40]. These variations were specifically observed at around 250 Hz. The recommendations for preparing transducers for underwater calibrations state that “if the mount influences the measured sensitivity, the hydrophone should be calibrated in the same mount that will be used for measurements made with the hydrophone in the field” [47]. A boot used in the actual MEMS sensor packaging was used to determine experimentally which features were generated by the boot. The designed mounting as well as the actual device build and tested are shown in Figure 30.

Responses of a reference hydrophone B&K 8103 were measured with and without the boot. The adaptation of the mount allowed measuring the influence of the boot in the sensitivity range of interest. The measurements with the boot allowed for evaluation of the acoustic transparency of the window and helped to choose appropriate materials needed to minimize the effect of the housing on the sensor performance.

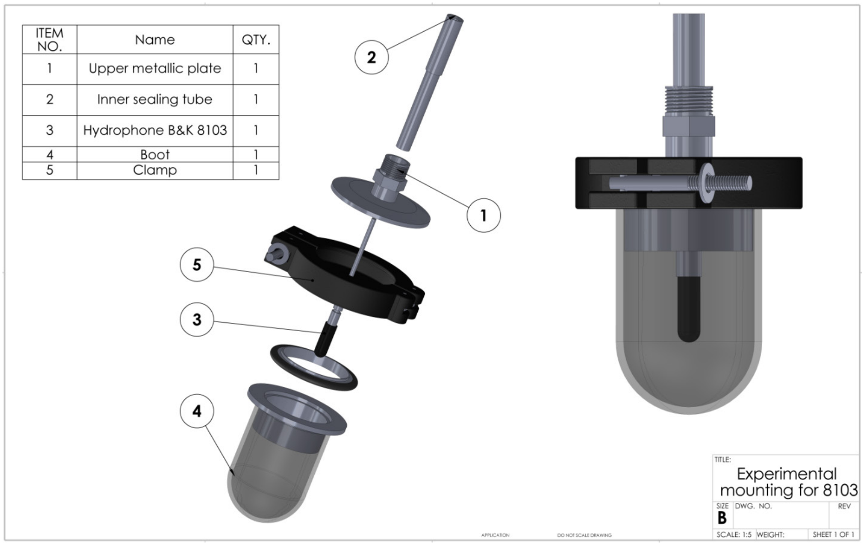

ITEM NO.	Name	QTY.
1	Upper metallic plate	1
2	Inner sealing tube	1
3	Hydrophone B&K 8103	1
4	Boot	1
5	Clamp	1

Figure 30. CAD model of the mount used for measurements

The tests of the boots were carried out in the water tank facility at NPS, employing the free-field calibration by comparison method [47].

The schematics of the measurement system and physical description are shown in Figure 31 and Figure 32. These include the block diagram of the measurement setup and the placement of the components during the calibration process, respectively.

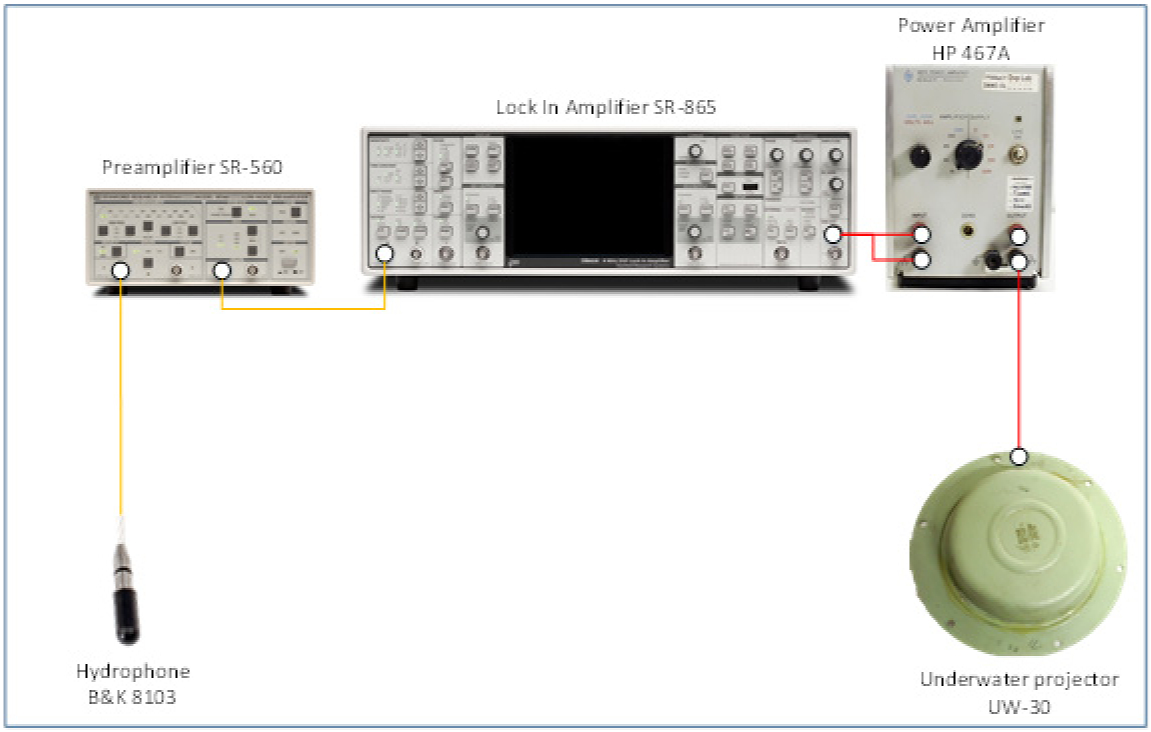

Figure 31. Schematic of measurement setup

The data was captured by a lock-in amplifier SR-865 sweeping frequency from 50 Hz to 1000 Hz. This setup produced a 250-point vector, which gives the frequency measured and the amplitude of the signal received in mV. The signal from the hydrophone was amplified (2000 times) using a preamplifier SR-560. The sync output of the lock in amplifier with a 350-mV amplitude was fed to a power amplifier to drive the underwater projector Lubell UW-30.

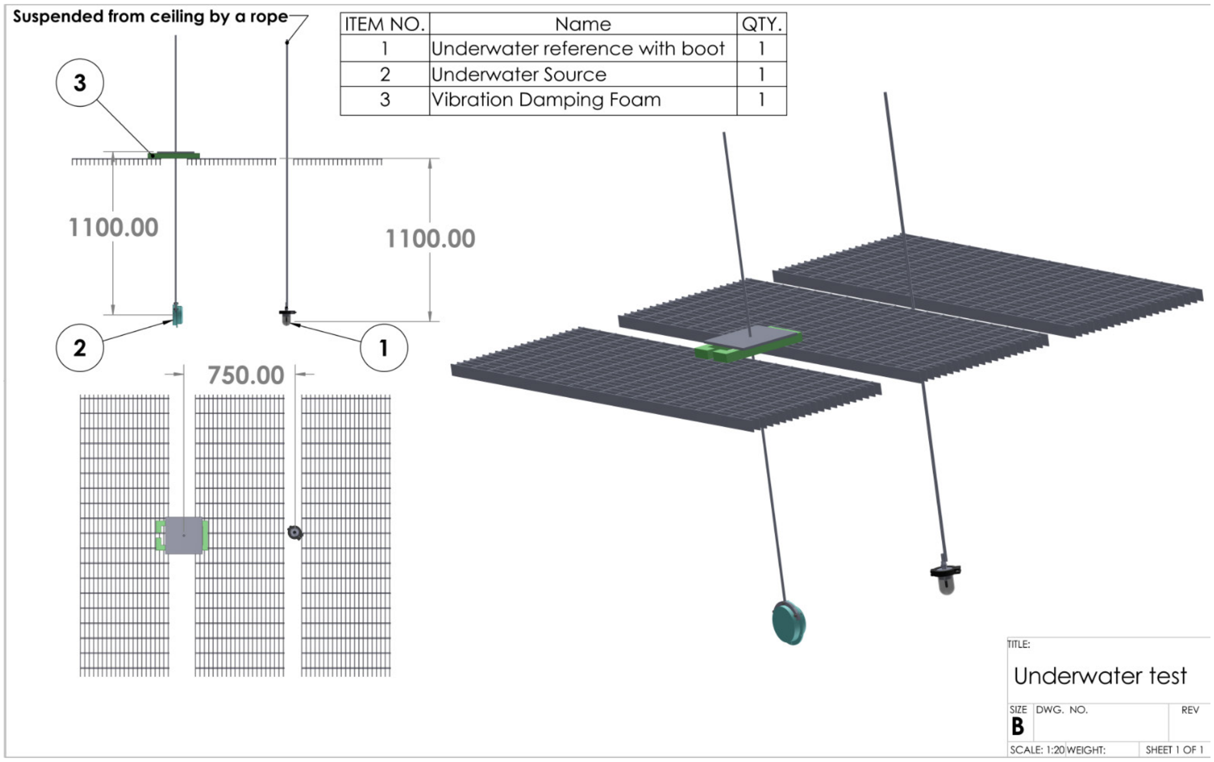

ITEM NO.	Name	QTY.
1	Underwater reference with boot	1
2	Underwater Source	1
3	Vibration Damping Foam	1

Figure 32. Calibration setup with dimensions

2. Sensitivity Comparisons

In the first test, sensitivity of the reference hydrophone mounted inside the boot was measured. When the boot was mounted, a resonant feature around 280 Hz was observed, as shown in Figure 33. In contrast, the response of the hydrophone without the boot showed no resonant feature at 280 Hz.

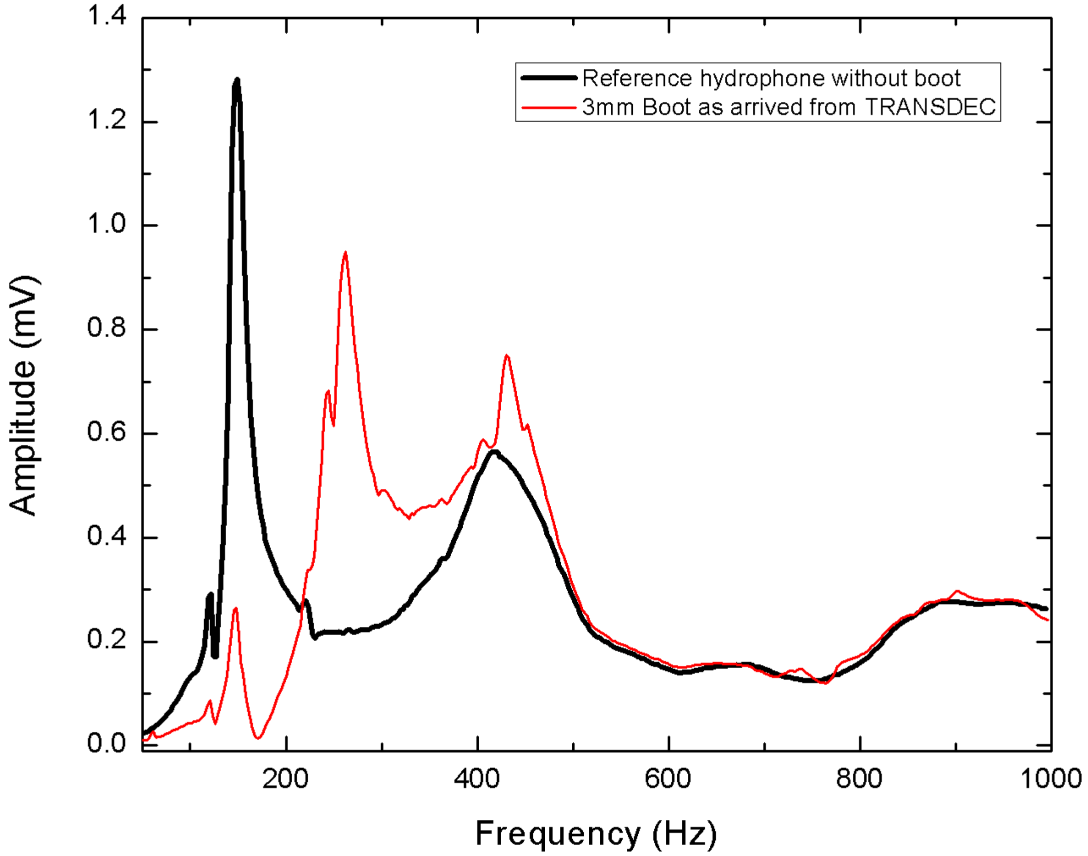

Figure 33. Responses of the reference hydrophone with and without boot

After analyzing the data, the oil while still inside the boot was degassed for a day using a vacuum chamber at -29 inHg. A significant difference of the response of the hydrophone was observed, in which the resonant feature at 280 Hz was slightly decreased and the amplitude of the received signal at the resonant frequency of the underwater source was significantly improved, as shown in Figure 34.

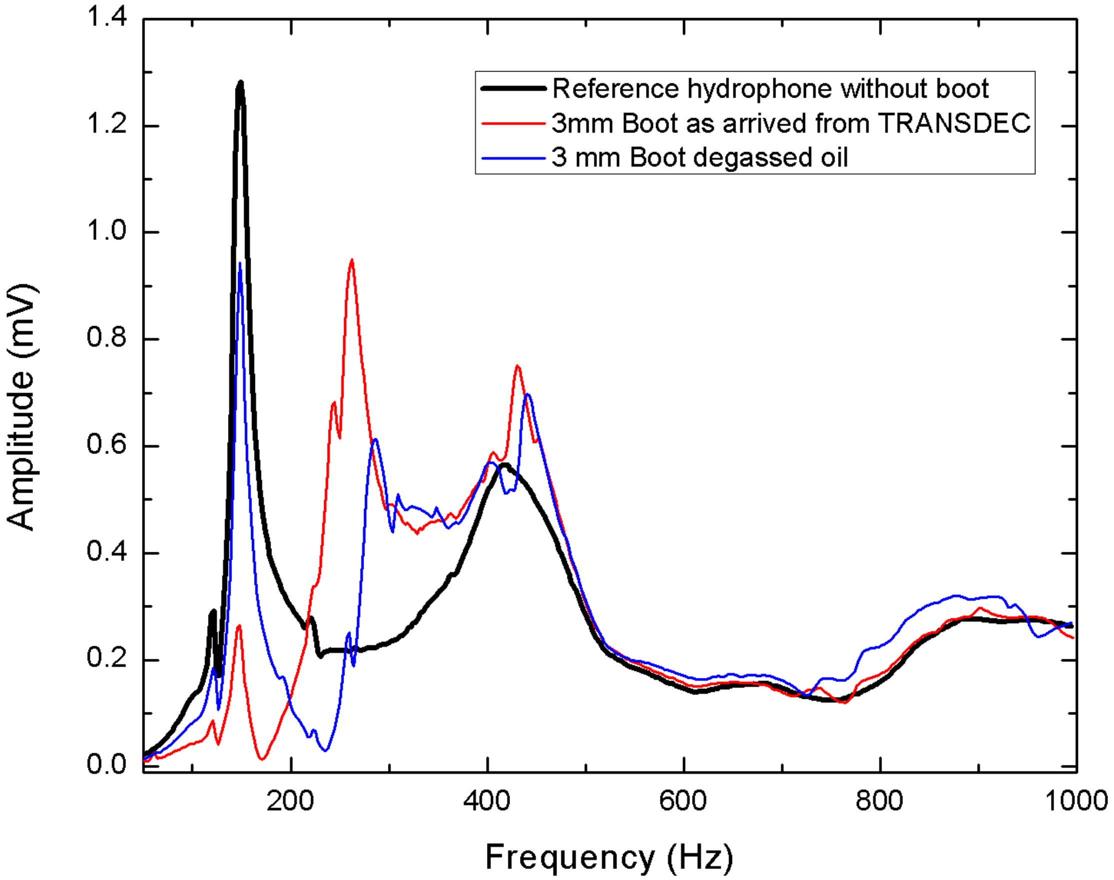

Figure 34. Sensitivity calibration after degassing the oil

The presence of bubbles in the oil showed a significant variation of the acoustic signal received in the interior of the boot. This variation motivated the study of the acoustic properties of the system with boots of different thicknesses and materials. The prototypes were built, and their results are presented here.

The next task was to reduce the amount of bubbles present in the boot material and compare the effects of the thickness on the transmission of the acoustic field. Three Flexane 80 boots were molded—B5-1, B3-2, and B1.5-3—corresponding to 5, 3, and 1.5 mm-thick boots, respectively. The results of the response measurements using these prototypes are shown in Figure 35.

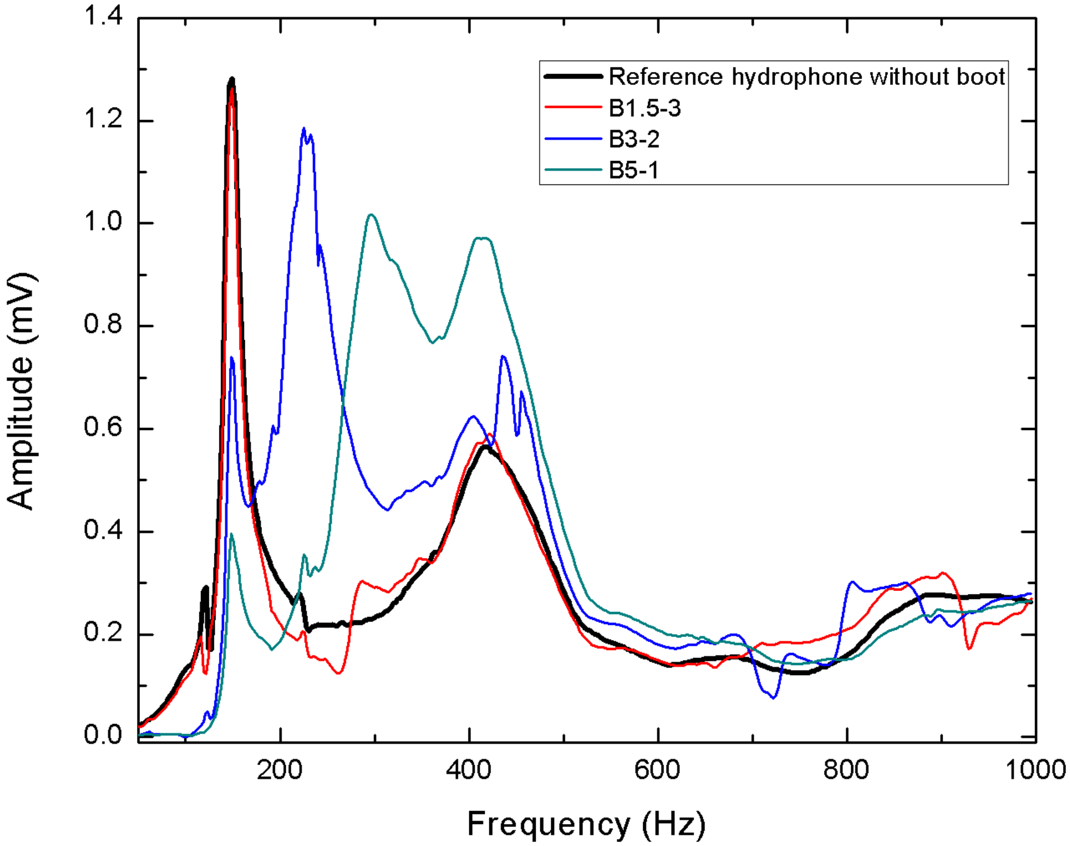

Figure 35. Sensitivity comparisons for 5-, 3-, and 1.5-mm-thick Flexane-80 boots

As observed, the thickness of the boot modified the position of a resonant peak after the source resonance frequency, which is approximately at 140 Hz. It was observed that reducing the thickness significantly improved the acoustic transmission of the boot. This improvement motivated experimenting with different materials in order to study if variations of the elastic modulus could generate a shift in frequency that kept out of the operating frequency of the MEMS sensor.

The next experiment consisted of building three boots with different thicknesses using PMC-780, which, according to the seller, was the material that had the closest chemical properties to the material NUWC XP-1 reported by [48]. Three boots were molded using this material—B5-2, B3-4, and B1.5-10—corresponding to thicknesses of 5, 3, and 1.5 mm, respectively. The results of the calibrations using these prototypes are shown in Figure 36.

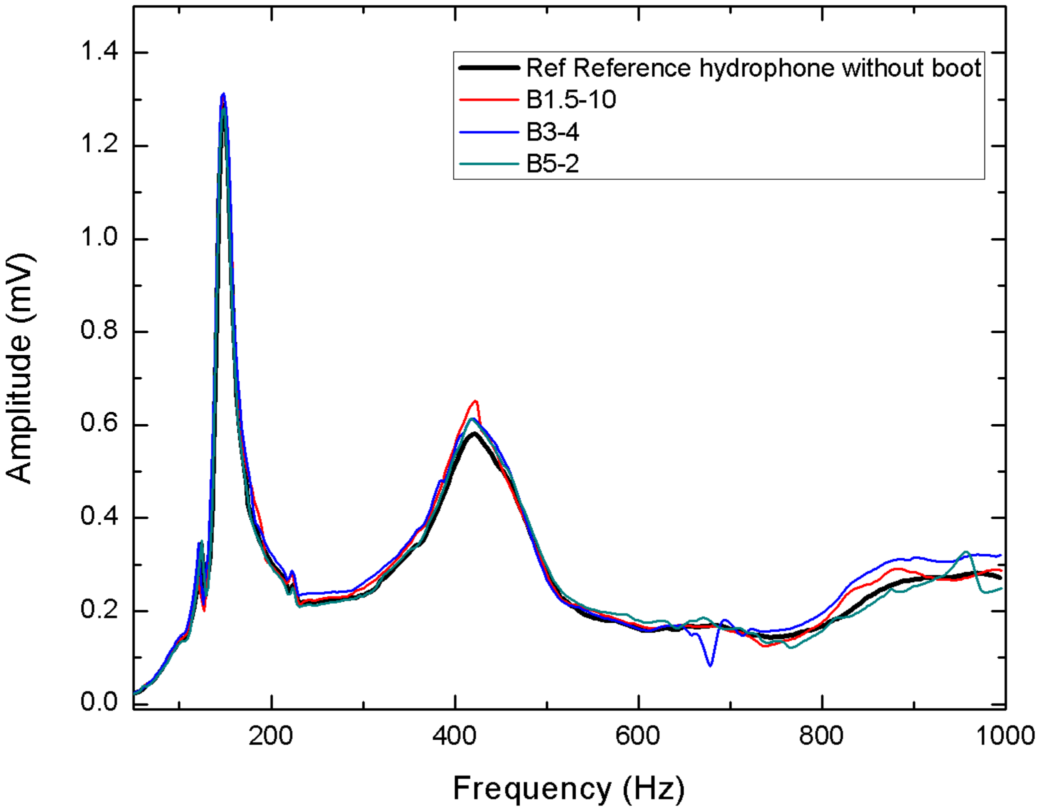

Figure 36. Sensitivity comparisons for 5-, 3-, and 1.5-mm thick PMC780 boots

The PMC-780 polyurethane showed a better acoustic transmission and completely eliminated any undesired resonant features regardless of the thickness used. This showed a promising material that could be used for packaging the MEMS acoustic sensor for underwater operation.

Finally, a hard-shell boot was also molded. This experiment was carried on to test if the resonant frequency could be shifted beyond 600 Hz. An Epox A-Cast-690 crystal clear boot was molded. Boots B3-2, B3-4, and B3-11 were molded in 3-mm thickness using Flexane 80, PMC-780, and Epox Acast-690, respectively. The results of the calibrations using these prototypes are shown in Figure 37.

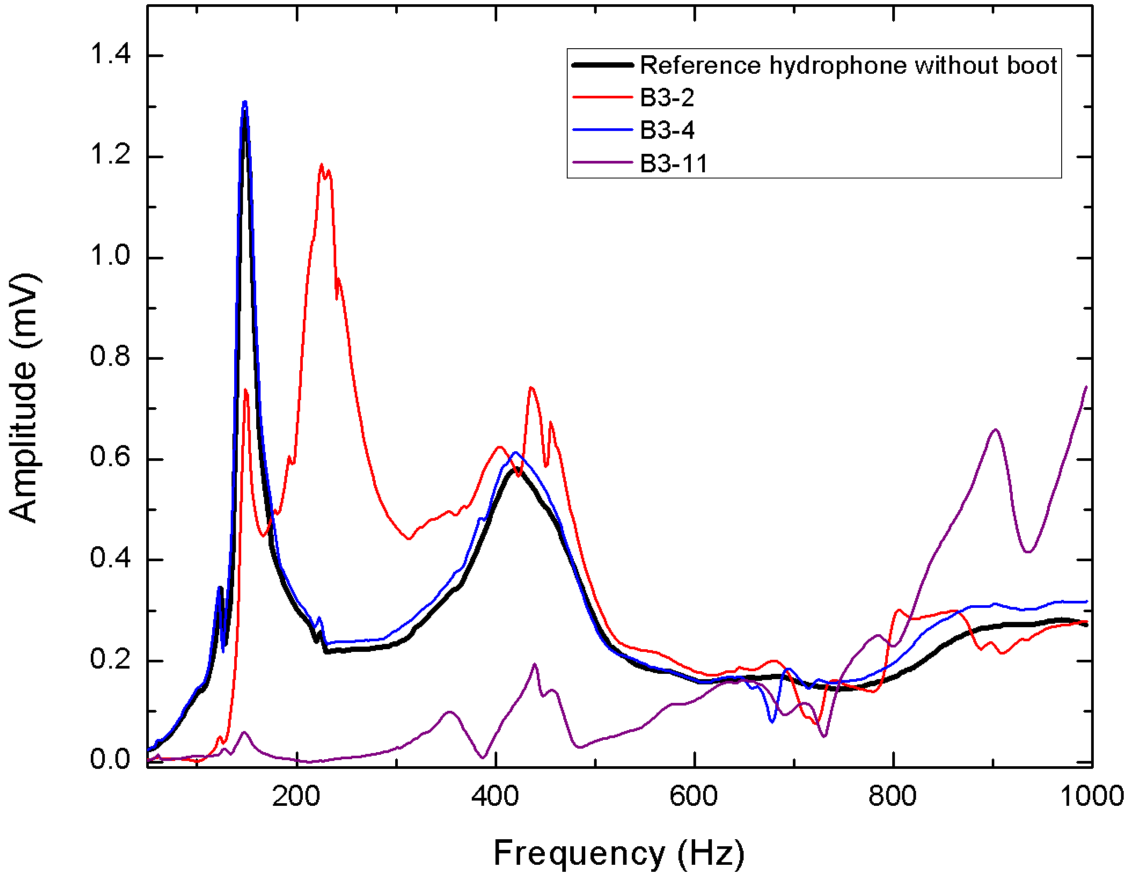

Figure 37. Sensitivity comparisons for 3-mm thick boots, molded with Flexane-80, PMC-780, and Epox Acast 690

As expected, the frequency shift using a hard boot moved out of the 600-Hz region, while completely attenuating the resonant frequency of the source.

After comparing the behavior of the boots molded under two different techniques and using three different materials, the 3-mm boot using PMC-780 polyurethane was chosen as the option to package the MEMS acoustic sensor for underwater application.

3. Acoustic Transmission Comparison

For this experiment, the graphs were generated using MATLAB to interpolate the frequency sweeps done during the different experiments. The acoustic transmissions were calculated by dividing the data with boot by without boot. This data was appropriately normalized by the individual sensitivities of the two different hydrophones employed. The results of this analysis are shown in Figure 38.

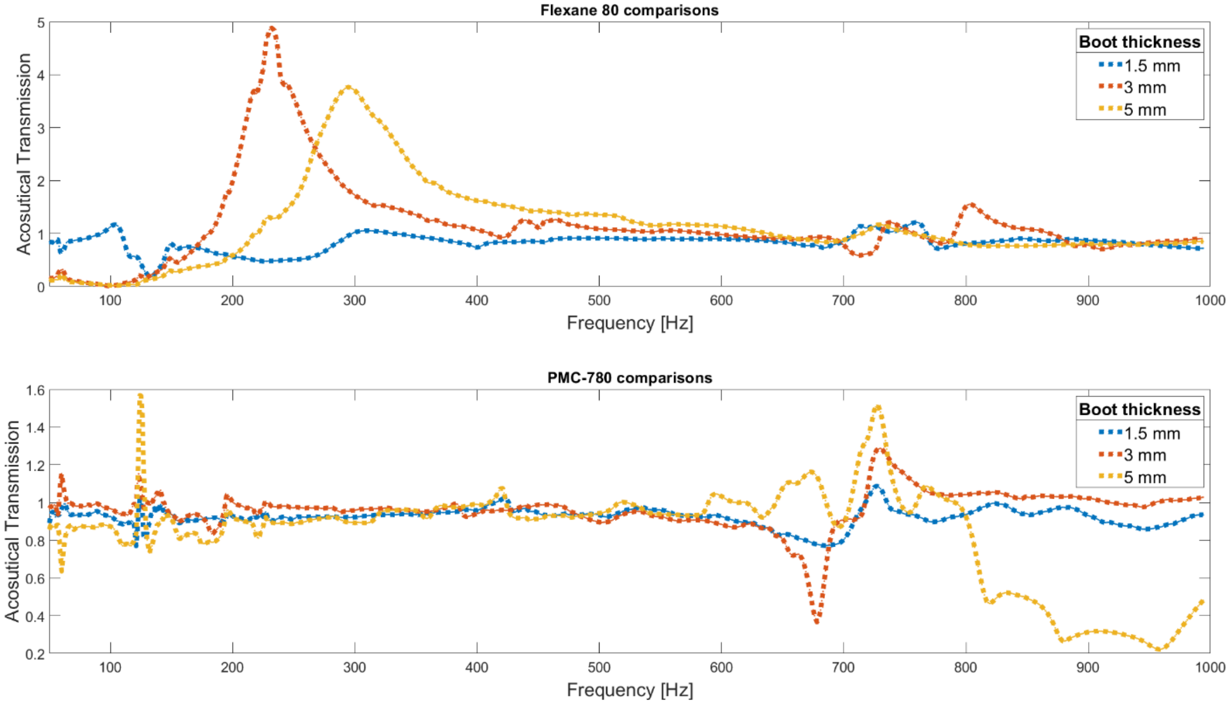

Figure 38. Acoustic transmission comparisons for 5-, 3-, and 1.5-mm boots, molded with Flexane 80 and PMC780

It is possible to observe certain regions where the transmission was higher than 1; one possible reason of this behavior could be a resonance of the boots by themselves, which was addressed in Chapter II. We were able to measure a most uniform sound transmission using the PMC-780 boots, in which almost all the lines were close to a reference value of 1, indicating acoustical transparency in the 200 to 600 Hz range. This is in comparison to Flexane-80 boots made with 5- and 3-mm thicknesses, where a sound amplification from 200 to 600 Hz could be observed.

If this behavior could be appropriately understood and modeled, this would represent an additional advantage for enhancing sensor performance, suggesting that the boot could be tailored to the operating frequency of the sensor. In addition, enhancement of response at boot resonance can be used as a second resonance peak.

THIS PAGE INTENTIONALLY LEFT BLANK

IV. SENSOR ASSEMBLY AND CHARACTERIZATION

After optimizing the simulation, the next steps were to fabricate and characterize MEMS sensor performance, both in air and underwater. This process involved the design of the masks for microfabrication, microfabrication (done using an external foundry service), electronic packaging, and characterization.

The testing was done at the NPS anechoic chamber for the air characterization while underwater characterization was carried out using the NPS water tank and TRANSDEC facilities. Using these facilities, frequency and directional responses were measured.

A. SENSOR FABRICATION AND ELECTRONIC PACKAGING

The first step was to generate masks using MEMS Pro software according to the design rules of the micromachining process. The silicon-on-insulator multi-user micromachining process (SOIMUMPS) employed in the fabrication provides two options for the device layer thickness of silicon-on-insulator (SOI) wafers (10 or 25 μm). In addition, four processing steps used include front and back etching and two metallizations to facilitate electrical connections. According to the SOIMUMPs design rules [49], "The four available mask level SOI patterning and etching processes" are: 1) deposition and patterning of the pad metal layer made of 20 nm of chromium and 500 nm of gold, followed by a liftoff process, 2) lithographic patterning and DRIE etching of the device layer, 3) lithographic patterning and DRIE etching of the substrate layer, followed by a wet oxide etching and removal of remaining oxide using a vapor HF process, and 4) deposition of blanket metal layer using a shadow masking technique.

Once the sensors were received from the manufacturer, they were thoroughly inspected by microscopy, looking for known micromachining issues like damage of comb fingers and partial release of wings and comb fingers. A picture of a fabricated sensor taken with a digital microscope is shown in Figure 39.

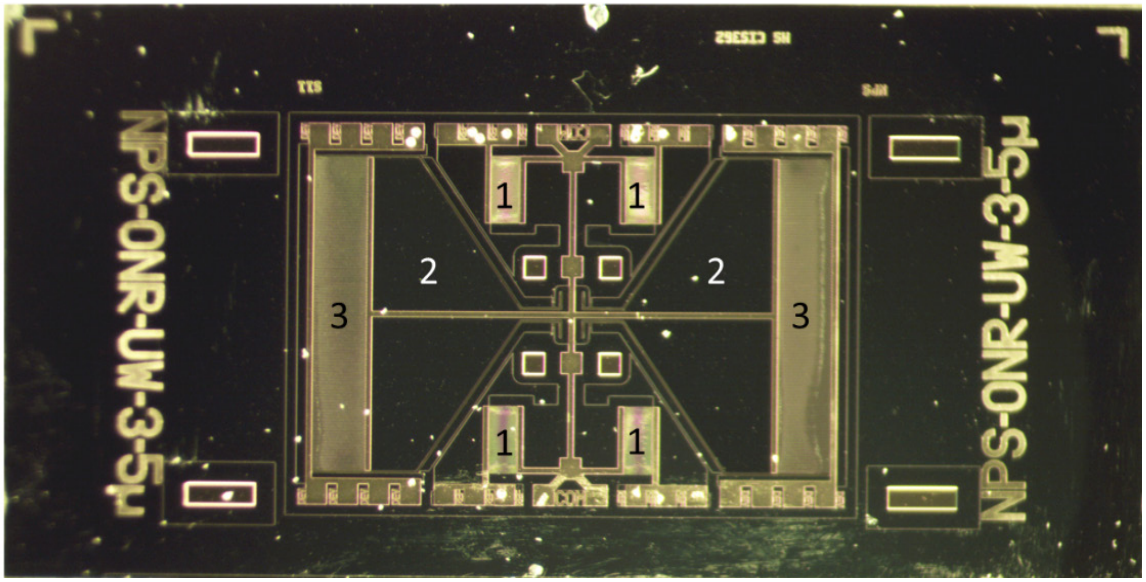

Figure 39. MEMS acoustic sensor (Generation 3) with 5 μm gap between comb fingers. (1) Reference capacitors, (2) wings, and (3) interdigitated comb fingers for capacitance readout.

After the visual inspection, the sensors were mounted on a custom-fabricated circuit board with MS3110 capacitive readout integrated circuit and wire bonded for testing. The testing began with connecting the assembled sensor to a MS3110 programming board to balance the bridge formed by the sensor and reference capacitors, as described in [2].

B. CHARACTERIZATION IN AIR

After initial testing of the sensor in the lab, it was mounted in an anechoic chamber for detailed characterization. In the anechoic chamber, both the frequency and directional response of the sensor were performed. For the frequency response, sound was incident on it at normal. The rotation measurement was done using the built-in turntable.

The sensitivity results obtained (Dr. Renato Rabelo helped to obtain the data) are plotted in Figure 40, which shows the measured sensitivity as a function of frequency for the sensor shown in Figure 39. A main resonance peak due to the bending mode is observed at around 1580 Hz, and a weak feature, possibly due to the rocking mode, is observed at around 1470 Hz. The experiment was performed setting the orientation of the sensor at normal incidence and 45° with respect to the normal. It was found that light did not affect the sensor characteristics, though the silicon-based sensor was exposed to it.

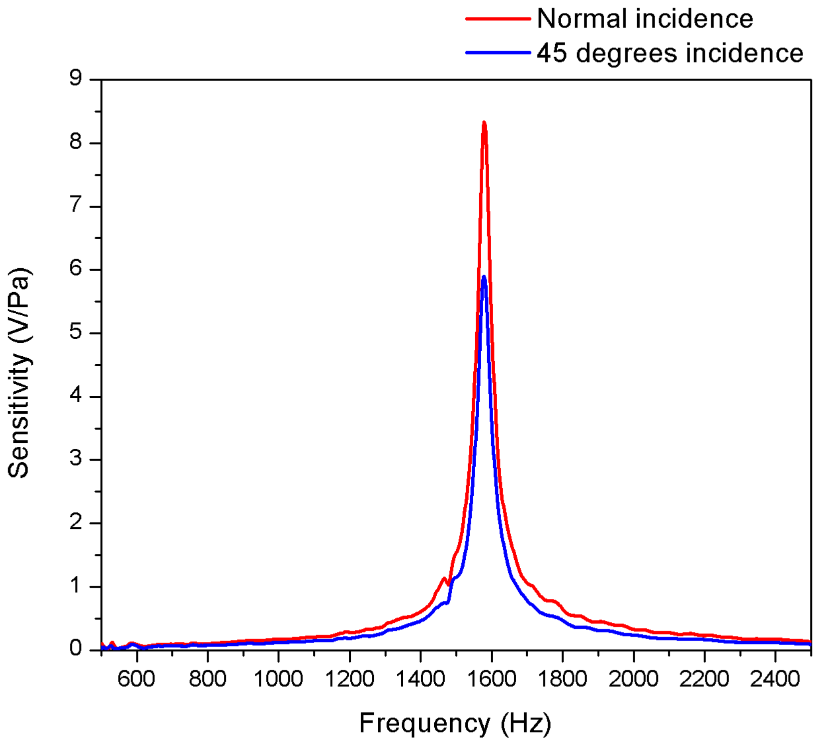

Figure 40. Measured sensitivity of sensor in air

A polar plot of the directivity pattern obtained at the resonant peak is shown in Figure 41. This 8-shaped directivity pattern corresponds to the expected directional response due to interaction of sound from both sides of the wings, making it act as a pressure-gradient microphone [32]. The maximum amplitude is at normal incidence while the null occurs when the sound wave travels parallel to it. This behavior is characteristic of the two-element interferometer configuration [2].

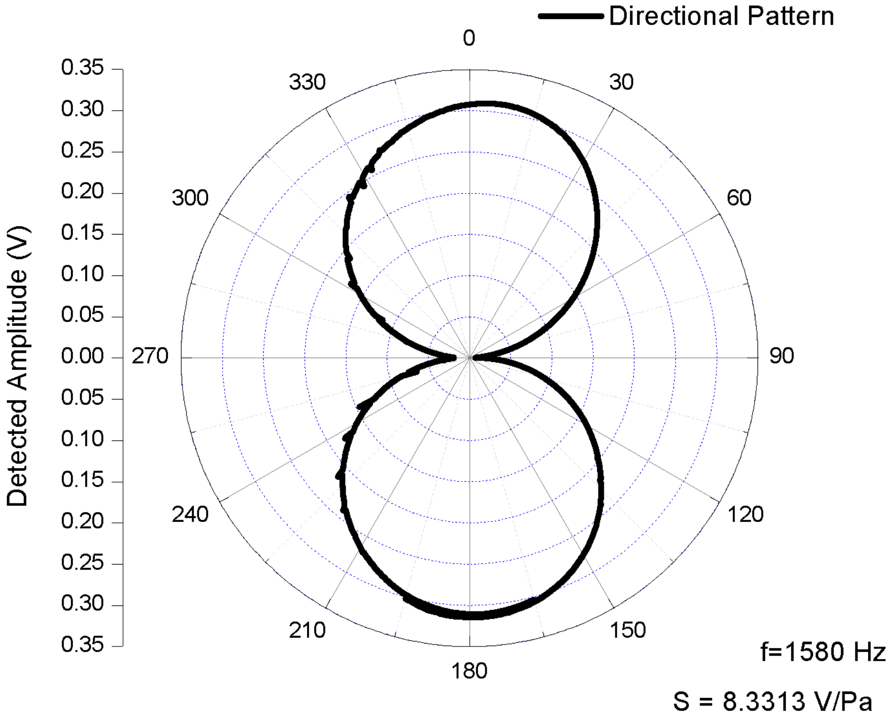

Figure 41. Measured directivity pattern in air

C. UNDERWATER PACKAGING CONSIDERATIONS

Several considerations should be taken into account before adapting the MEMS sensor to underwater operation. As Swan [38] and Da Re [40] mentioned, the primary purpose is to submerge the sensor protected from an underwater environment while being able to receive and transduce acoustic signals. The option used for this task was to design an acoustically transparent housing capable of withstanding an underwater environment. This packaging should allow the transmission of sound from the exterior environment to the sensor. In addition, the MEMS sensor should be immersed in a low-viscosity dielectric fluid that does not interfere with the functions of readout electronic circuitry.

The adaptation of the sensor for an underwater environment must consider acoustical, mechanical and electrical effects:

- Acoustical effects. Primarily focused on improving the transparency of the boot to incident sound in addition to holding the silicone oil used for immersing the sensor.

- Mechanical effects. During the calibration process, it was noticed that the adhesive used for mounting the sensor to the circuit board stressed the die, which affected the balance point due to change in capacitance. In addition, change in temperature in water could also affect the stress condition of the sensor.

- Electrical effects of the underwater packaging were related to the change in the operational environment from air to silicone oil. When the sensor was immersed in oil, the capacitance changed due to the higher dielectric constant of the oil. Thus, it was necessary to characterize the dielectric constant of degassed and non-degassed oil in order to determine additional capacitance needed to balance the bridge.

In order to build a reliable repetitive process for assembling the sensor, all of the above-mentioned steps should be taken into account.

Once the boot was optimized for acoustic transparency in the desired frequency range, the sensor was mounted in it for testing. After several tries, it was found that degassing the oil before submerging the sensor as well as balancing the readout electronics at a temperature similar to that of the water tank was needed to avoid drifting of the balance point with temperature.

1. Effect of Silicone Oil on Sensor Capacitance

The balancing of the capacitance bridge in readout electronics requires the knowledge of how the comb finger capacitors change when submerged in oil due to its higher dielectric constant. The capacitance balance is usually done through adjustment of the built-in capacitors of the MS3110 chip, which are not affected by the oil [37]. Thus, the balance point can affect the oil, which generates an unwanted DC offset.

In order to determine change of capacitance when submerged in oil, we measured it using a Keysight B1500A semiconductor device analyzer with help of Keysight B1500A Opt ASF test fixture. Additionally, a Johnson variable plate capacitor 160–311-1 was employed to determine the dielectric constant of the degassed oil. The variable plate capacitor has three terminals, two connected to a fixed set of plates and the third connected to a central rotating rod with a set of plates. This capacitor allows adjustment from 2.7 to 19.6 pF. The measurement position was set at 11.08 pF, approximately the middle of the range. First, the capacitance was measured in air. Second the capacitance was measured using non-degassed cSt-1 silicone oil. Third, the capacitance was measured using cSt-1 15 min degassed oil. Finally, the capacitance was measured using cSt-1 24 h degassed oil. Figure 42 shows a measurement of capacitance as a function of bias across the terminals using cSt-1 oil degassed for 15 minutes.

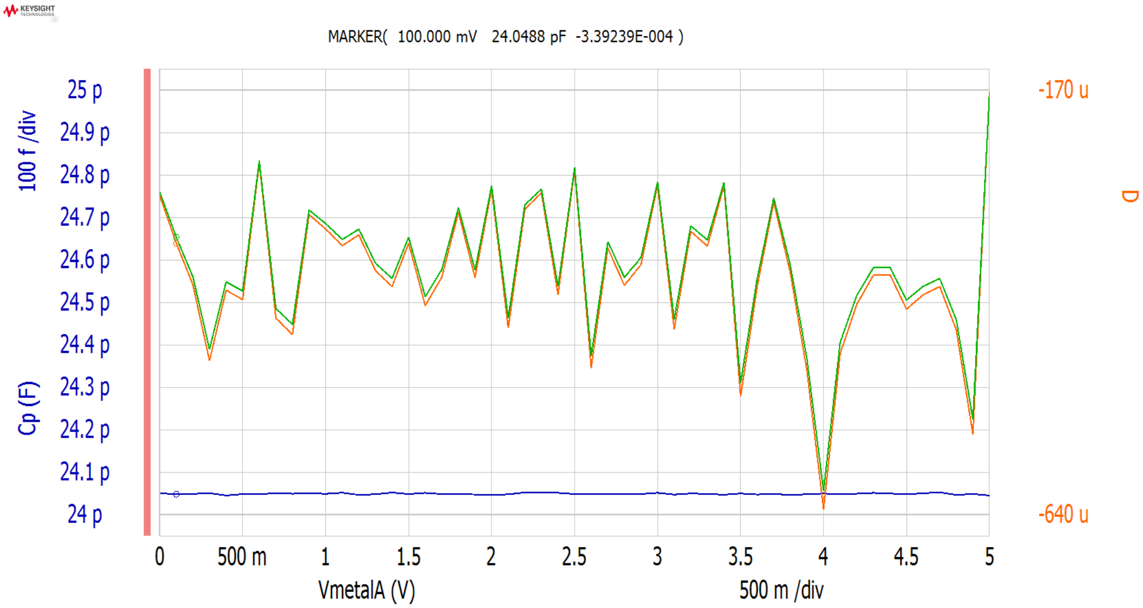

Figure 42. Measured capacitance with bias for cSt-1 oil after 15 min degassing

As observed in Table 2, the capacitance of the oil did not seem to change under different degassing conditions.

Table 2. Capacitance measured values

Measurement condition of the variable plate capacitor	Measured capacitance (pF)
Air @ 22.6°C	11.0861
cSt-1 oil @ 22.4°C. non-degassed	24.1431
cSt-1 oil @ 22.1°C. 15 min degassed	24.0913
cSt-1 oil @ 21.9°C. 24 hour degassed	24.1145

The dielectric constant of oil can be calculated using the measured capacitances in air (C_{air}) and in oil (C_{oil}) as presented in Equation 4.1 derived from [50]:

$$\varepsilon_{oil} = \frac{C_{oil}}{C_{air}} \varepsilon_{air} \tag{4.1}$$

$$\varepsilon_{oil} = \frac{24.11[pF]}{11.09[pF]} 1.000589 * 8.85 * 10^{-12} \left[\frac{F}{m}\right] = 19.26 * 10^{-12} \left[\frac{F}{m}\right]$$

In addition, the relative permittivity of oil ($\varepsilon_{relative\ oil}$) can be obtained as:

$$\varepsilon_{relative\ oil} = \frac{\varepsilon_{oil}}{\varepsilon_0} = \frac{19.26 * 10^{-12} \left[\frac{F}{m}\right]}{8.85 * 10^{-12} \left[\frac{F}{m}\right]} = 2.175$$

The measured relative dielectric agrees with the values reported by Carey [51], indicating that for oils this parameter is between 2.1 and 2.8. The dielectric constant of a pure compound strongly influences its viscosity, melting point, boiling point and refractive index . The displacement of wings of the MEMS sensor depends on the viscosity of the fluid. Thus, the dielectric constant indirectly influences the oscillation amplitude in addition to the comb finger capacitance.

2. Assembly for Underwater Characterization

After corroborating that the sensor works properly in air, we assembled it for underwater testing. First, the circuit board was attached to the flange with the electrical connectors. As described before, two oil degassing processes were included before assembling the sensor for underwater testing. First, the oil was degassed in a cup to extract all the air that could be trapped in it. Second, the oil was poured into the boot and degassed again to extract the air that became trapped in the grooves of the boot produced by the molding process.

Once the oil had been degassed, the sensor was submerged in the oil and the clamp was installed. A small plug in the flange was used to inject oil into the boot and eliminate any trapped air bubbles. The components of the assembly and assembled sensor are schematically shown in Figure 43. Lastly, the capacitance bridge was balanced again. The capacitance balance was done by submerging the assembly in water for at least 15 minutes to allow a thermal settling.

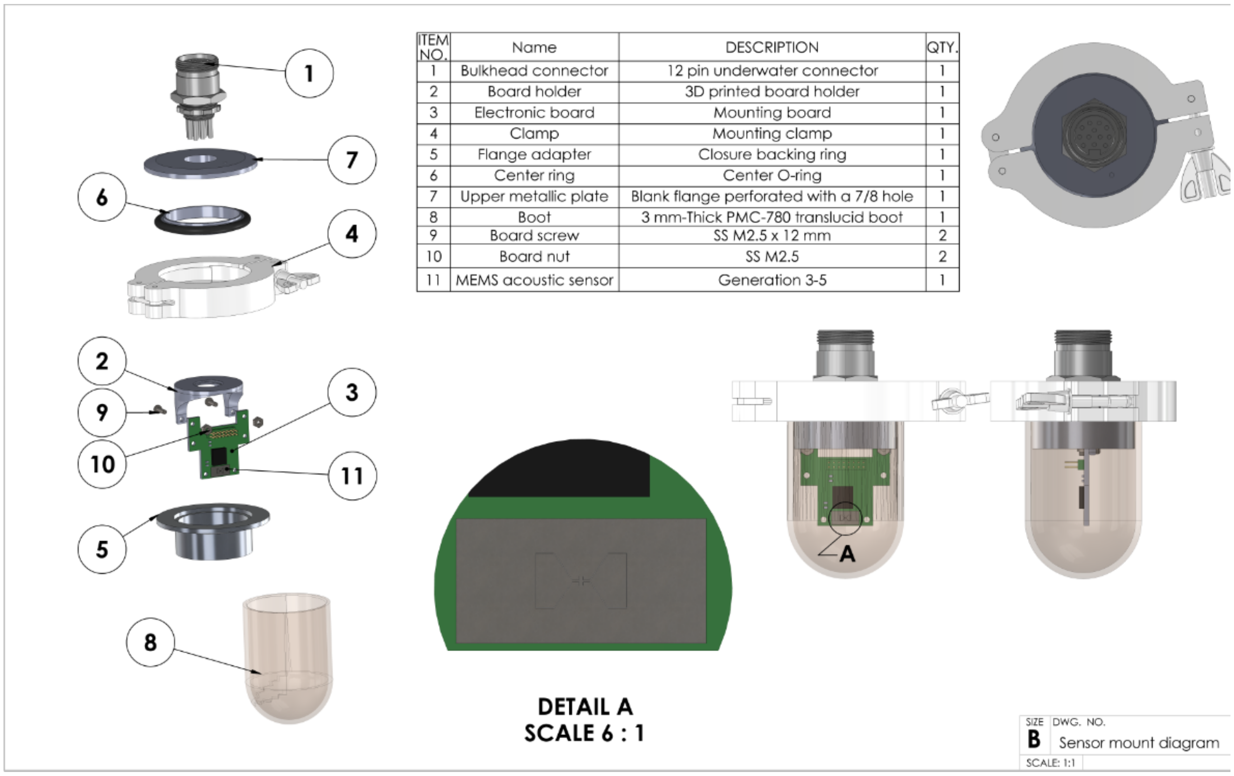

ITEM NO.	Name	DESCRIPTION	QTY.
1	Bulkhead connector	12 pin underwater connector	1
2	Board holder	3D printed board holder	1
3	Electronic board	Mounting board	1
4	Clamp	Mounting clamp	1
5	Flange adapter	Closure backing ring	1
6	Center ring	Center O-ring	1
7	Upper metallic plate	Blank flange perforated with a 7/8 hole	1
8	Boot	3 mm-Thick PMC-780 translucid boot	1
9	Board screw	SS M2.5 x 12 mm	2
10	Board nut	SS M2.5	2
11	MEMS acoustic sensor	Generation 3-5	1

Figure 43. Schematics of parts and assembled sensor

D. UNDERWATER CHARACTERIZATION AT NPS

Testing of the MEMS sensor was carried out using the NPS water tank as well as the TRANSDEC facility. The measurement setup employed for characterizing the frequency response of the sensor is shown in Figure 31.

The measurements were taken following some of the recommendations established on IEC 60565 [47] and ANSI/ASA S1.20-2012 [52]: 1) Before submerging the sensor, a wetting agent was applied in order to improve the coupling of sound and eliminate air bubbles on the surface of the boot and 2) the sensor and acoustic source were submerged in the tank for at least 24 hours prior to the test, allowing thermal setting and air dissipation.

The distance between the source and sensor was determined based on the far-field distance condition given in Equation 4.2. The far-field distance (d) can be estimated by [52] as:

$$d > \frac{\pi a^2}{\lambda} \tag{4.2}$$

Where a is the radius of the source (10.61 cm) and λ the wavelength of the highest frequency used in the measurement. The estimated far-field distance for the frequency range of interest was about 7.5 cm. During the characterization, the sensor was placed at either 75 or 20 cm from the source. The sensor was suspended from the ceiling to minimize any mechanical coupling.

The tests carried on at NPS consisted of measuring the frequency responses under the following conditions: 1) reference hydrophone B&K 8036082 without boot, 2) reference hydrophone B&K 8036083 with boot, and 3) MEMS sensor G3-5. Figure 44 shows measured raw frequency responses from 50 to 1000 Hz for these three measurements. It was determined that the peak at approximately 140 Hz is primarily generated by the source based on measurements and simulations presented in Chapters II and III. Figure 45 shows the measured raw frequency response with the resonance of the sensor at 285 Hz.

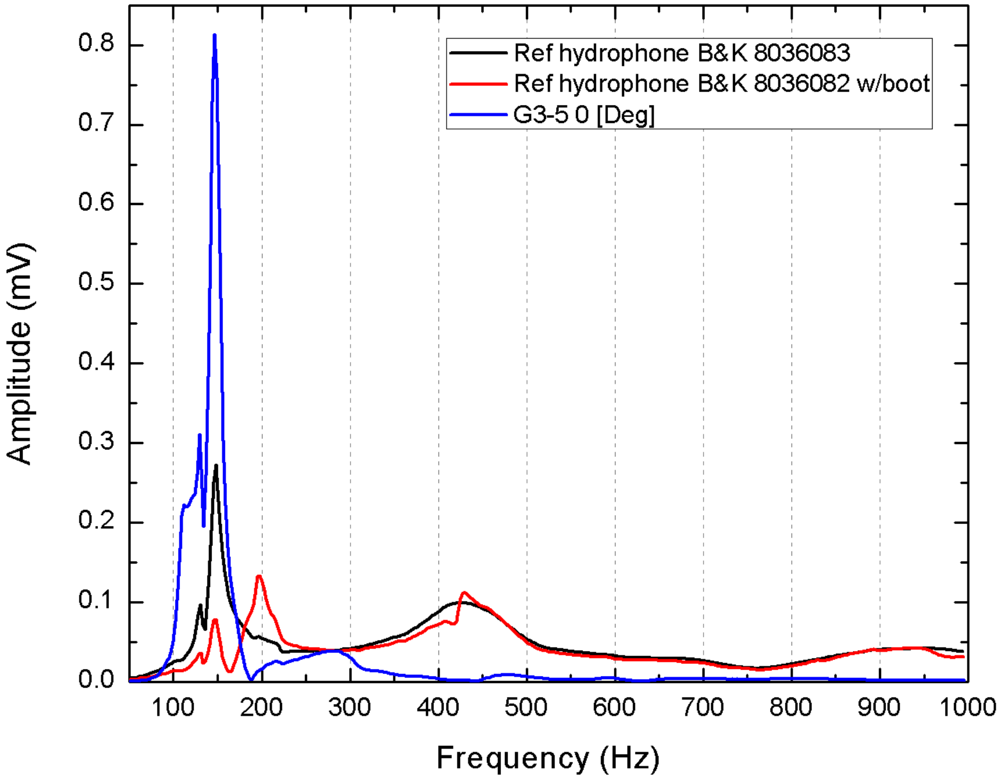

Figure 44. Measured signals from hydrophone and sensor using the NPS water tank.

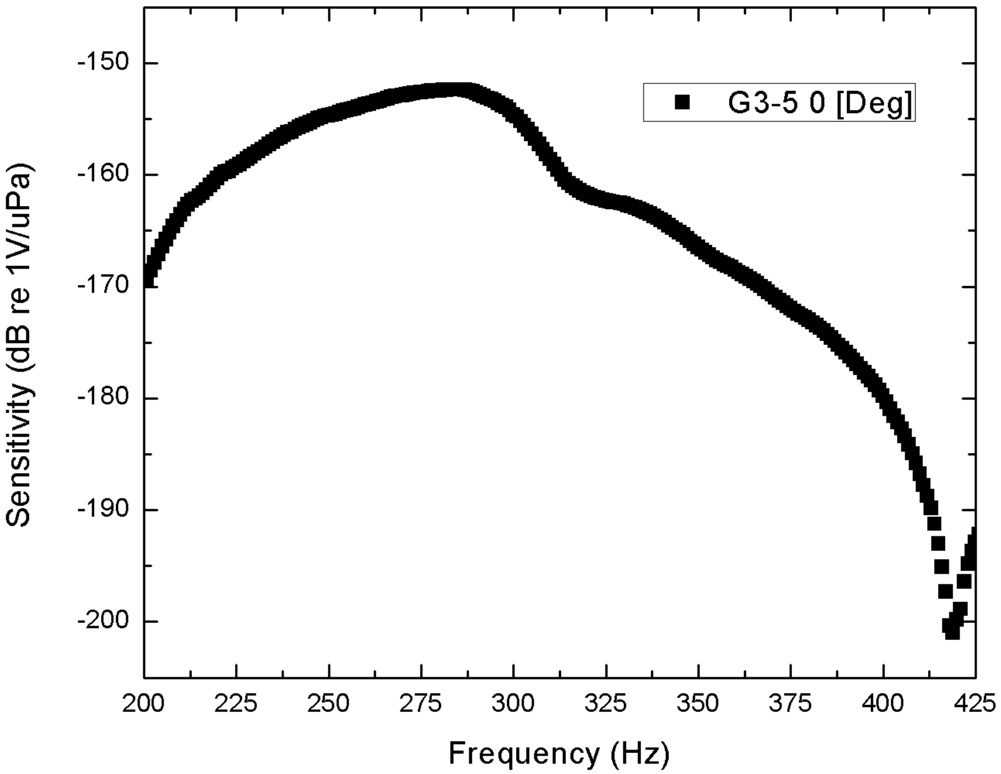

Figure 45. Sensitivity of the MEMS acoustic sensor G3-5 with frequency.

Figure 46 shows the measured sensitivity of the MEMS sensor at 0, 45°, and 90° incident angles of sound for frequencies from 200 to 300 Hz. A resonant peak centered around 275 Hz can be seen in Figure 45. The sensitivity (dB re 1V/µPa) was calculated using the measured signal of the MEMS sensor divided by the sound pressure at the sensor, measured using a calibrated hydrophone as shown in Equations 4.3 and 4.4 [53]:

$$SPL = \frac{V_{ref}\left[mV\right]}{G * S_{ref}\left[\frac{mV}{Pa}\right]} \tag{4.3}$$

$$S_{G3-5} = 20 * \log\left(\frac{\frac{V_{G3-5}\left[V\right]}{SPL\left[Pa\right]}}{1\left[\frac{V}{\mu Pa}\right]}\right) \tag{4.4}$$

where *SPL* is the sound pressure at the sensor, V_{ref} is the measured signal of reference hydrophone, and G =1000 is the gain of the amplifier used for reference, S_{ref} is the sensitivity of the hydrophone (-212.6 dB re 1V/µPa) and $V_{G3\text{-}5}$ is the signal from the sensor.

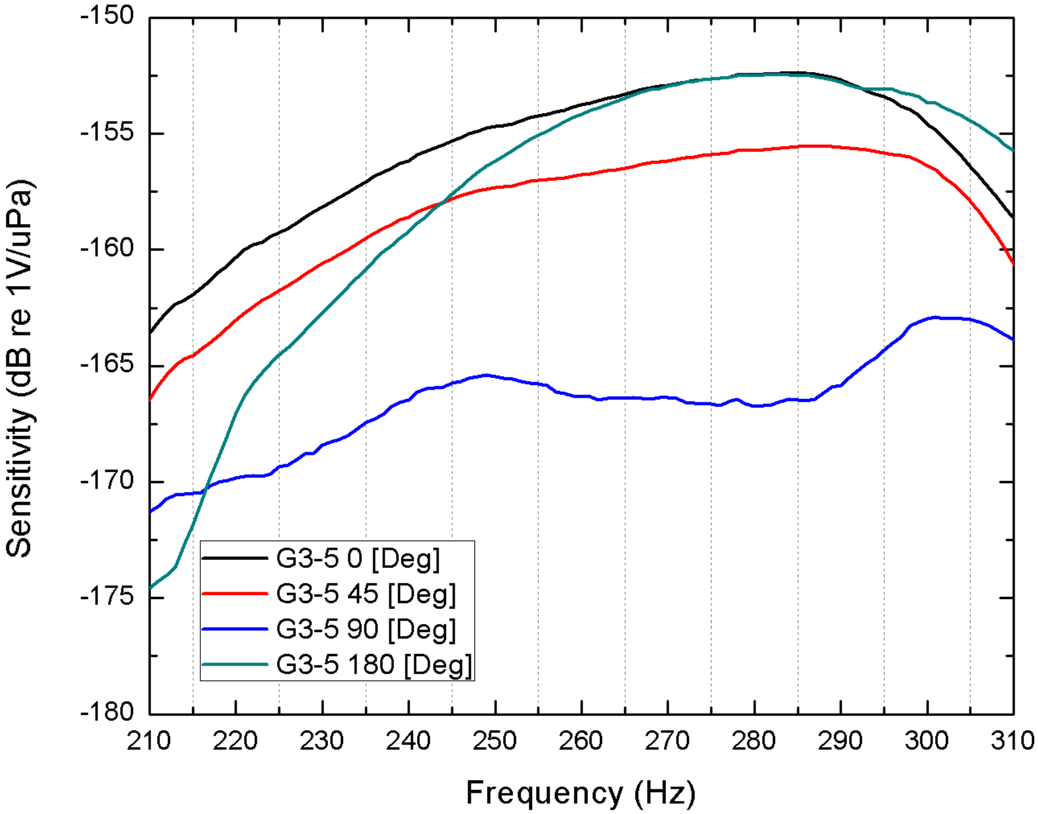

Figure 46. Sensitivity of MEMS sensor at four different angles

It can be seen in Figure 46 that as the incident angle of sound changed from normal incident to 90° degrees (parallel to the sensor surface) the sensitivity decreased by about 16 dB showing the directional response. As expected, the sensitivities measured at a 0° and 180° incidence are approximately the same. The lack of a rotator at the NPS facility made the detailed directivity measurement difficult and was later carried out at TRANSDEC.

E. UNDERWATER CHARACTERIZATION AT TRANSDEC

Once the sensor was tested in the lab, anechoic chamber, and NPS water tank, it was taken to the TRANSDEC underwater test facility for detailed characterization. The sensor attached to the test fixture at TRANSDEC is shown in Figure 47. The frequency responses of the MEMS sensor and a reference hydrophone were measured simultaneously from 220 to 450 Hz by placing then at equal distances from the sound source. The measured sensitivity of the sensor is shown in Figure 48. A resonant peak centered around 275 Hz can be seen in Figure 48, with maximum sensitivity of about -165 dB re 1V/µPa, which is about 30 dB higher than a typical broadband hydrophone.

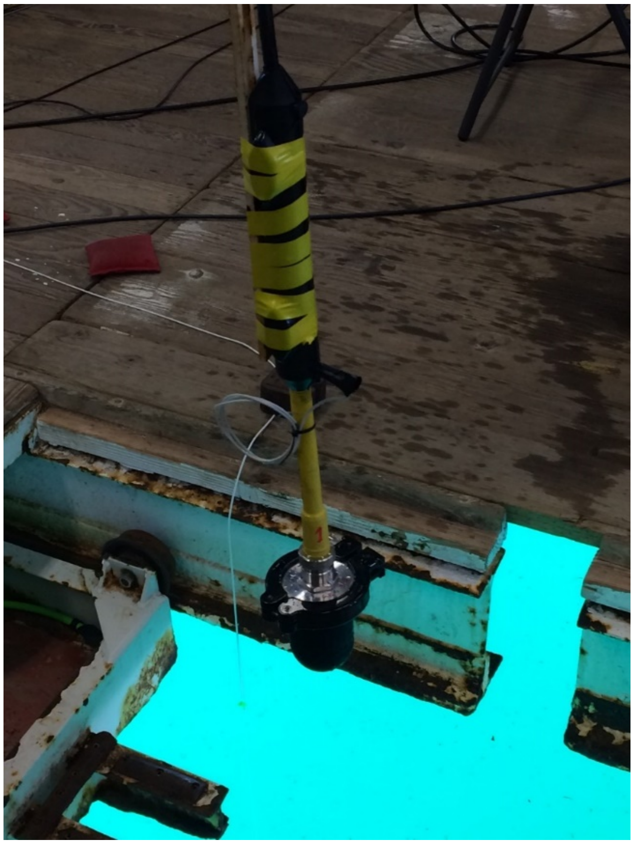

Figure 47. MEMS sensor (G3-5) prior to submerging at TRANSDEC

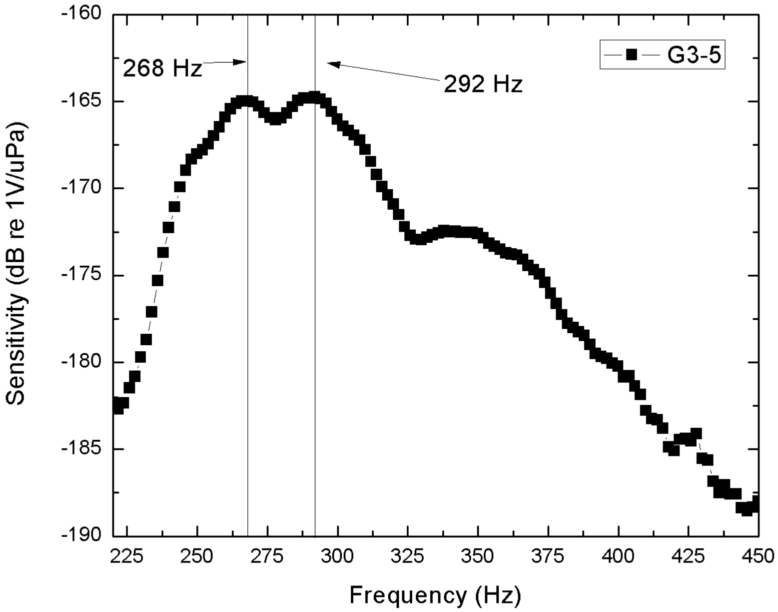

Figure 48. Measured sensitivity at TRANSDEC

The directional response of the MEMS sensor was measured by rotating it at the peak frequency of 292 Hz. The directivity pattern at 292 Hz is shown in Figure 49. An 8-shaped directivity pattern with uneven lobes was observed. Additional characterizations are required to fully understand the directivity pattern in an underwater environment.

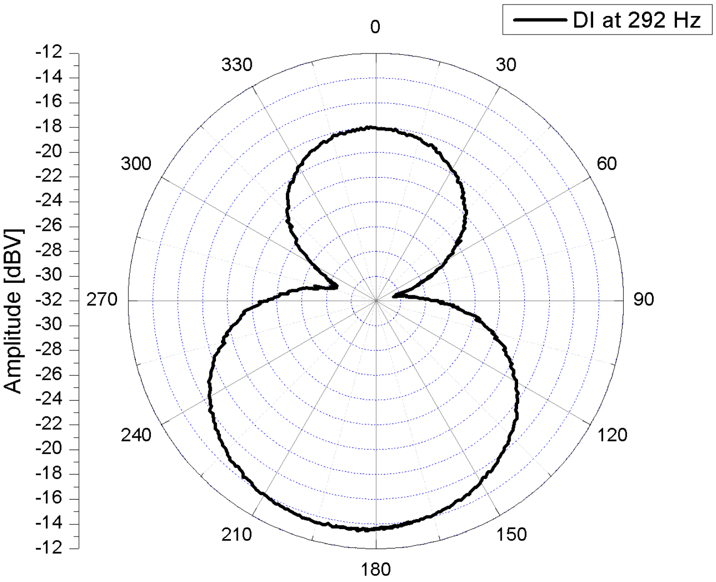

Figure 49. Measured directivity pattern at 292 Hz

F. COMPARISONS BETWEEN SIMULATION AND TESTS

The simulated and measured frequency responses in air and underwater are plotted in Figure 50 and Figure 51, respectively. The data in Figure 50 shows good agreement between simulated and measured responses. The slight difference of the peak positions (about 6 Hz) is most likely due to the uses of designed parameters in the simulation versus the actuals, which can vary during fabrication. The simulated and measured frequency responses in Figure 51 show relatively larger difference between peak positions (about 30 Hz), possibly due to approximations employed in FE modeling.

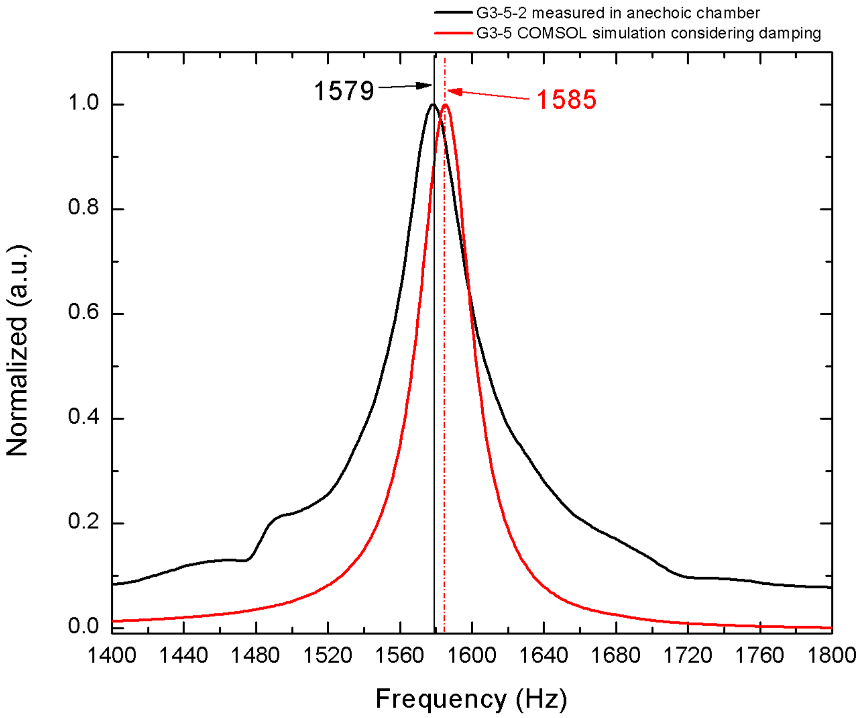

Figure 50. Measured and simulated frequency responses in air

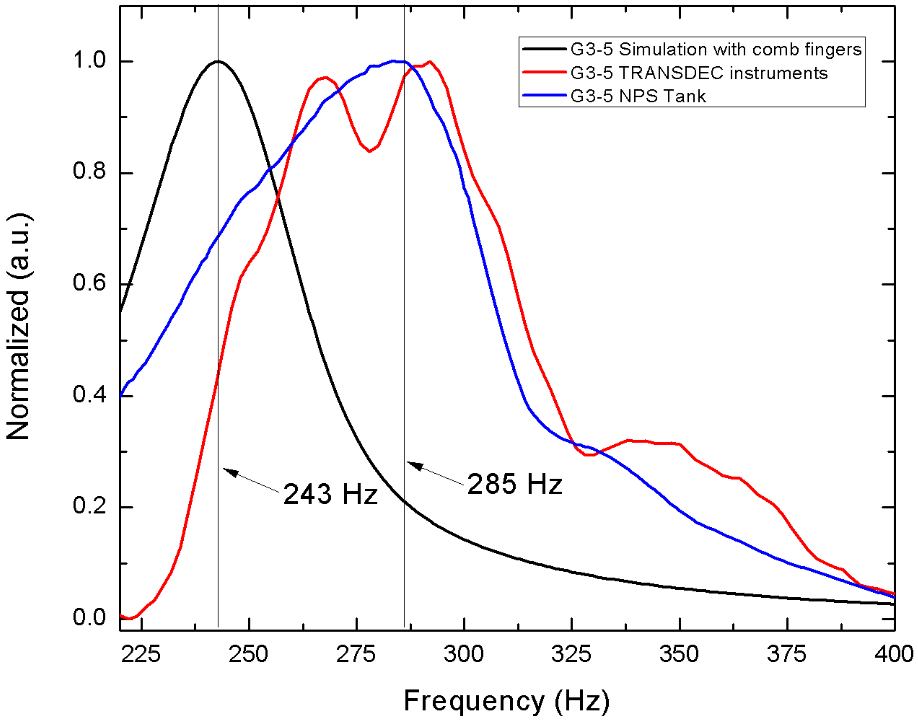

Figure 51. Measured (NPS-blue and TRANSDEC-red) in underwater and simulated (black) frequency responses

V. FABRICATION OF MEMS ACOUSTIC SENSOR

To date, the MEMS acoustic sensors have been fabricated using the MEMSCAP foundry service and the sensor development has reached a stage that requires some variations with respect to what is commercially available. In addition, longer turnaround time can be reduced if the fabrication process can be developed using the cleanroom facility at NPS.

Towards achieving these goals, recipes needed for micromachining of MEMS sensors are being implemented using the tools available at NPS cleanroom facility. In the following sections, the initial findings are presented.

A. THE IMPORTANCE OF MEMS TECHNOLOGY

MEMS devices are an emerging technology that take advantage of the manufacturing processes implemented by the microprocessor industry. Using those techniques, researchers have developed microsensors and actuators based primarily on the advantages of mechanical properties of silicon. The main advantages of this technology are batch production, miniaturization, and low power consumption, among many others. Some of the preeminent real-world applications in MEMS technology are in microfluidics and inertial, optical, and biomedical devices [50].

NPS has been developing micromachining capabilities using its Microsystems Fabrication Laboratory. The basic processing tools and needed characterization instrumentation are already available in this facility, which enable us to develop recipes needed for fabricating MEMS acoustic sensors.

B. ADVANTAGES OF MEMS ACOUSTIC SENSOR MICROMACHINING AT NPS

MEMS bioinspired acoustic sensor is a microstructure built from a silicon wafer. The two approaches previously employed to fabricate MEMS acoustic sensors were polysilicon surface micromachining process (POLYMUMPS) and silicon-on-insulator micromachining process (SOIMUMPS) offered by the MEMSCAP foundry service [49].

Details of the fabrication processes using these two approaches were discussed by Shivok [33] and Touse [32].

The SOIMUMPS process used for the MEMS acoustic sensor fabrication is based on SOI wafers. These wafers consist of a 400-µm-thick substrate with a device layer (10 µm or 25 µm) separated by a 1-µm-thick silicon oxide layer. The process provides a minimum feature size of 2 µm. The SOIMUMPS design handbook [49] establishes the instructions, design rules, and recommendations for using this service.

Using the SOIMUMPS services, the allowable device layer thickness is limited to 10 or 25 µm. This limitation reduces the flexibility of using thickness as a variable for tuning the sensor characteristics such as frequency of operation. To address these issues, the SRL team at NPS has decided in parallel to explore the fabrication of MEMS acoustic sensors using our cleanroom facility.

C. SENSOR MICROMACHINING PROCESS

The general micromachining process requires at least the following steps: conceptual design, FE modeling, layout of masks, processing flow, manufacturing of specific tools and masks, and tailoring of the micromachining process for specific applications.

As explained by Touse [28], the steps executed to design and fabricate the sensors include the following:

1. The conceptual design comes from the *Ormia Ochracea* fly’s direction sensing ears
2. The modeling and mask layout are done using COMSOL and MEMSPro software, respectively
3. The micromachining process was executed by MEMSCAP, Inc. using its SOIMUMPS process

D. NPS MICROMACHINING PROCESS DESIGN

This task involves the adaptation of the commercially available materials and machinery to the specific needs for each of the steps involved during the MEMS acoustic sensor micromachining process. In this phase of the manufacturing process, a specific recipe for each of the steps has to be tested in order to build the specific features on the SOI wafer.

A 4-inch SOI wafer was used to create a batch of 24 Gen 1 (seeFigure 52) sensors using a 60-µm-thick device layer with variation of size of the wing and dimension of comb fingers. The thicknesses of the comb fingers were 5, 6, 7, 8, 9, and 10 µm, while the length of the wing was 500 or 980 µm. The processes tested involved surface and bulk micromachining, under the next sequence and as shown in Figure 53.

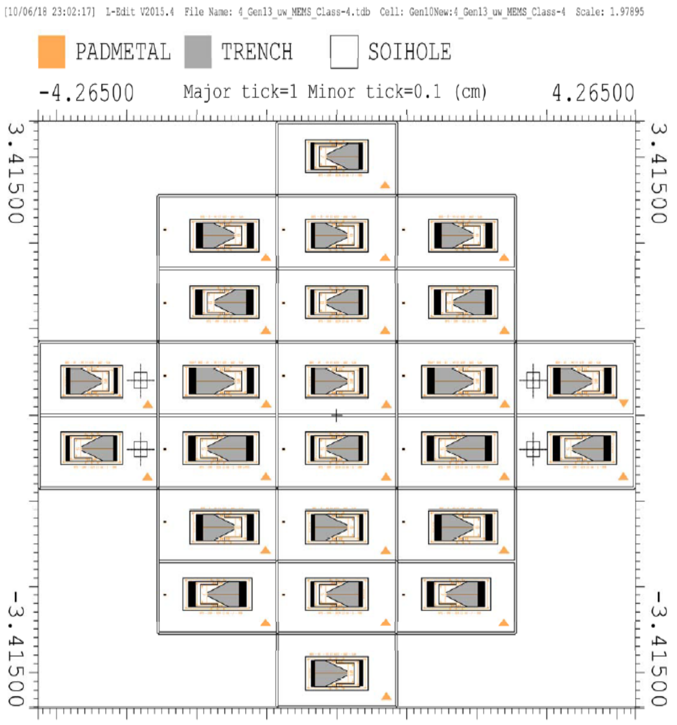

Figure 53. Mask layout

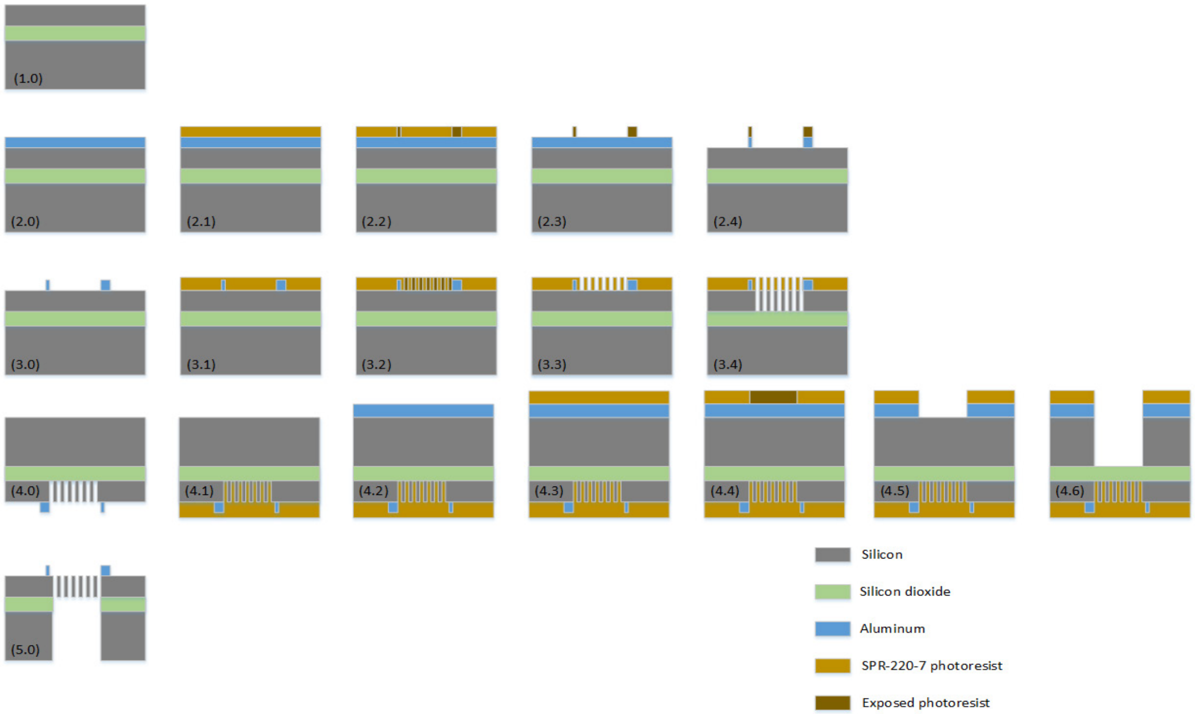

Figure 54. Cross-sectional view of micromachining sequence of Gen 1 MEMS sensor

The steps involved in the micromachining of the MEMS sensor were:

Step 1.0. The process started with a bare 440-µm-thick SOI wafer with 60-µm-thick doped silicon device layer separated by a 1-µm silicon dioxide layer.

Step 2.0. A 100-nm-thick blanket layer of aluminum was deposited using physical vapor deposition (PVD) and etched to form electrical contacts.

2.1 A layer of photoresist was deposited on top of the aluminum by spin coating.

2.2 The photoresist was lithographically exposed using the PAD mask and developed.

2.3 The photoresist was used as a mask for wet etching the aluminum.

2.4 The photoresist remaining over the aluminum was removed by dry etching.

Step 3.0. Etching of the wing and comb finger structure

3.1 A layer of photoresist was deposited on top of the silicon wafer with the patterned aluminum.

3.2 The photoresist was lithographically exposed using the SOI holes mask and developed.

3.3 The photoresist was used as a mask for etching in the device layer the silicon through a deep reactive ion etching (DRIE) process to form the wing and comb fingers.

3.4 The photoresist was removed from the front side using dry etching.

Step 4.0. Etching of backside trench to release the sensor

4.1 A new photoresist layer was deposited over the micromachined structures to protect them during the removal of substrate.

4.2 A layer of aluminum was deposited on the backside of the wafer by PVD.

4.3 A photoresist layer was deposited over the aluminum layer on the back of the wafer by mounting it on a chuck-and-spin coating.

4.4 The photoresist was lithographically exposed using the TRENCH mask and developed.

4.5 The photoresist was used as a mask for wet etching the aluminum to expose the silicon surface for subsequent etching of the substrate. The aluminum was etched by the developer.

4.6 The photoresist and aluminum layers were used as a mask for etching the silicon through a DRIE plasma process.

Step 5.0. The photoresist was removed, releasing the wing and comb fingers after etching the substrate and thin oxide layer underneath.

The following tools in the cleanroom were employed for micromachining: COVAP Angstrom PVD system, Alpha step D-500 KLA TENKOR Stylus profiler, spin coater, EVS-620 mask aligner, Filmetrics F40, Olympus B51microscope, Oxford Plasmalab system 100, and Sirus T2 Trion plasma etching system.

E. MICROMACHINING ADAPTATION TO NPS CAPABILITIES

Each step has a different purpose and its own considerations and specific recipes. The difficulties and particular variations encountered during each of the steps were as follows:

At step 1.0, ability of selecting the thicknesses of the device layer allowed us to change the resonant frequency of the sensor not just by modifying the dimensions of the wings, legs, and bridge, but also by varying the thickness of the bridge. The dependence of sensor characteristics on dimensions are explained in [34]. The wafer employed for this process had a 60-μm device layer, in comparison with the 25 μm available in the SOIMUMPS process.

At step 2.0, a process capable of depositing a conductive metal that could form an ohmic bonding with the silicon was needed. This was achieved by depositing aluminum. An image of the aluminum pads created in the NPS cleanroom is shown in Figure 53.

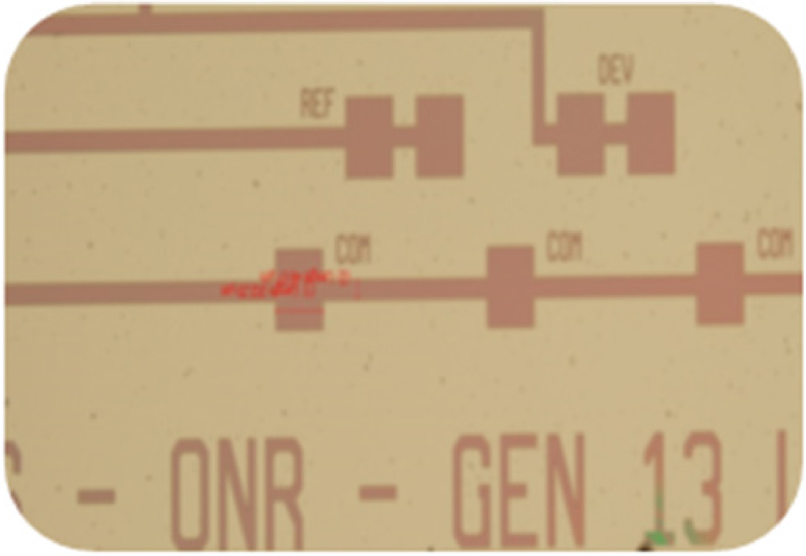

Figure 55. Aluminum pads etched in NPS cleanroom

The gold pads were commonly used in MEMS, which needed an interface material to make it adhere to silicon. The material intended was titanium, but the vacuum needed to reduce the vaporization temperature of titanium could not be reached in our evaporator. An alternative was nichrome, but that did not arrive in time for using this run.

At step 3.0, the main difficulty in using DRIE etching was the varying thickness of comb fingers. During this step, different numbers of DRIE cycles were carried out in order to observe and carefully control the desired depth without laterally etching the thinner comb fingers. The silicon device layer etched by surface micromachining to form the wing and comb fingers is shown in Figure 54. A three-dimensional optical profile of the comb finger structure is shown in Figure 55. This image was taken after 70 cycles of DRIE etching, which amounts to removal of 55 out of 60 µm of the device layer.

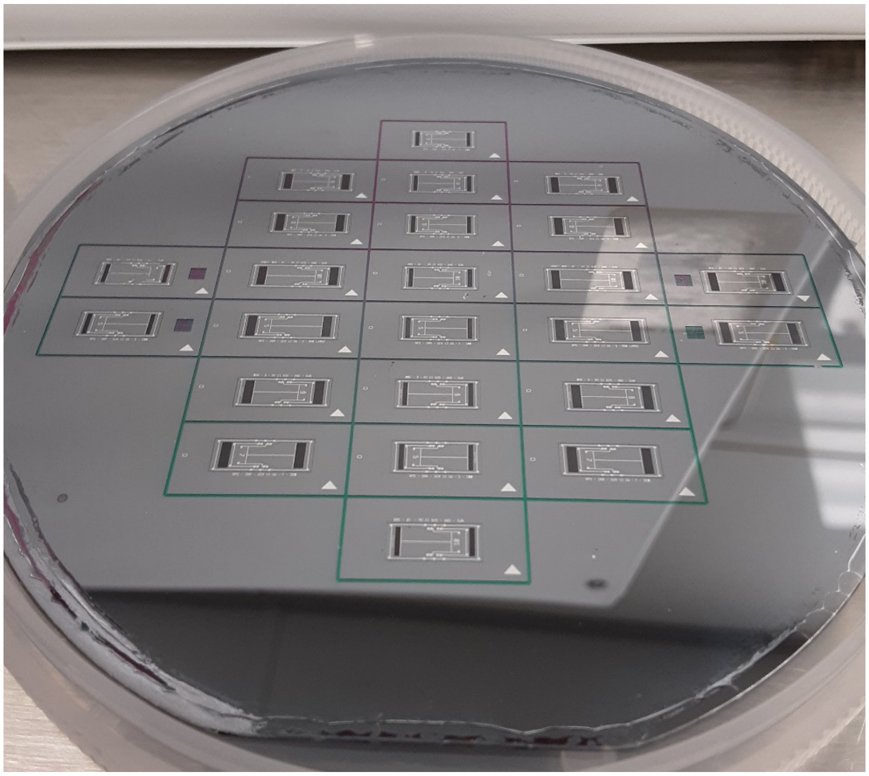

Figure 56. Micromachined wafer after steps 2.0 and 3.0

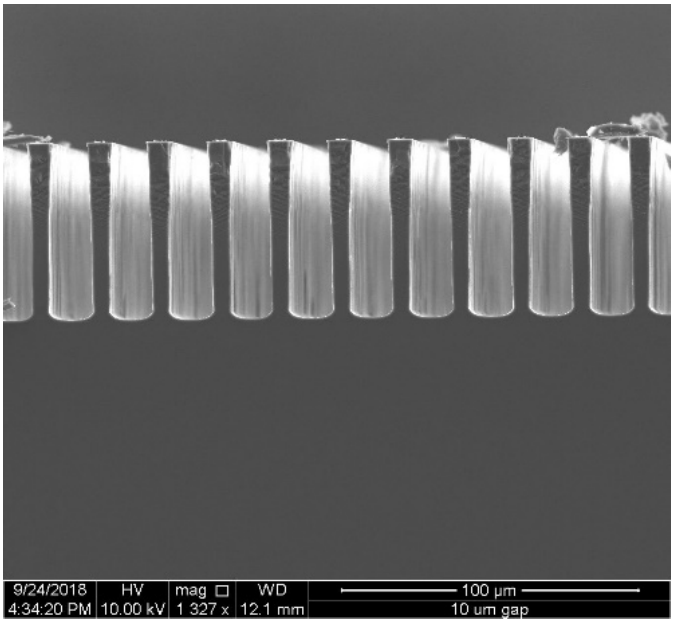

Figure 57. Electron microscope picture of the surface micromachined comb fingers. Source: [54].

At step 4.0, the main difficulty was to develop a recipe for etching of the backside of the wafer by the available tools. In addition, the unexposed part of the wafer needed to be protected using a suitable masking material during etching of the 440-µm-depth trench to release the sensor structure. We encountered two problems.

The first problem was the difficulty of holding the wafer in the spin coater using vacuum, due to the etched grooves on the front surface. These grooves prevented the vacuum holder from gripping the wafer tightly during spinning it. The problem was partially solved by implementing a special chuck, shown in Figure 56, to hold the wafer while spinning. The use of the chuck resulted in a delicate step due to dripping of the spun substances to the section below the wafer and ejection of the wafer during the spin coating process, causing the destruction of the wafer.

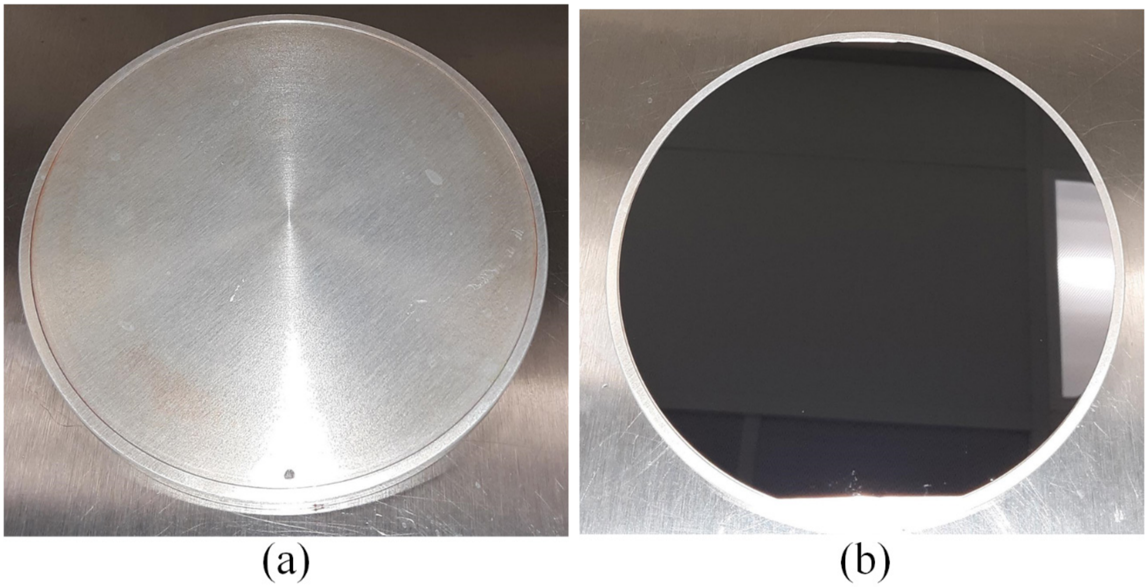

(a) (b)

Figure 58. Holding wafer chuck adapted to the spin coating equipment. (a) Chuck without wafer and (b) chuck with wafer.

The second problem consisted of creating an appropriate protective layer on the backside of the wafer. This protective layer needed to protect the silicon substrate to withstand enough cycles of the DRIE process, until all of the substrate underneath the sensor was etched to the desired depth. The first attempt was by forming a 12-µm SPR-220.7 layer, which did not withstand more than 200 DRIE etch cycles. The second attempt was by depositing an aluminum layer covered with a 12-µm SPR-220.7 layer, as shown in Figure 57 (a). This process satisfactorily solved the problem, allowing us to reach the SiO_2 layer after etching 440 µm of silicon with 560 cycles of DRIE etch, as shown in Figure 57 (b). Figure 58 shows the measured depths at different cycles of DRIE etching.

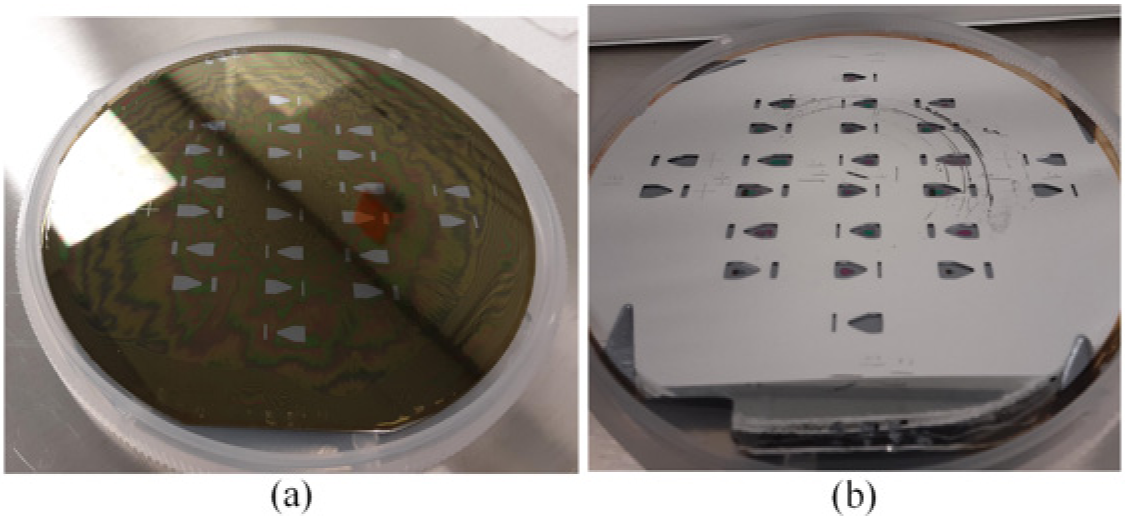

Figure 59. Backside patterning and etching. (a) 12 um of SPR-220.7 over 100 nm of aluminum patterned with TRENCH mask and (b) backside after 560 cycles of DRIE etching.

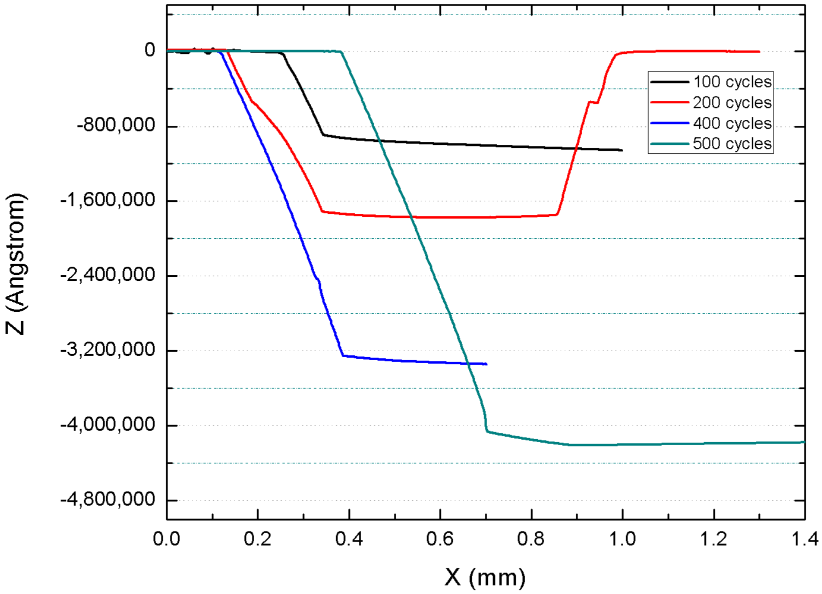

Figure 60. TRENCH etching evolution with number of DRIE cycles

A detailed explanation of each step was compiled by LT Riarh Parminder (Canadian Navy). The time spent to micromachine a 4-inch wafer, to produce 24 sensors, was 13 hours and 45 minutes. The estimation of times for each of the steps is summarized in Table 3.

Table 3. Estimated time for micromachining 24 MEMS acoustic sensors in a wafer

Steps	Estimated time [min]	Total time [min]
1.0	30	30
2.0, 2.1, 2.2, 2.3, and 2.4	75, 15, 15, 15, and 20	140
3.0, 3.1, 3.2, 3.3, and 3.4	20, 15, 25, 15, and 25	100
4.0, 4.1, 4.2, 4.3, 4.4, 4.5, and 4.6	30, 30, 75, 15, 25, 20, 300	495
5.0	60	60
Total time		825

Each 4-inch wafer was allocated 24 devices. After each major step, the sensors that were micromachined and did not show any apparent damage during the process were tallied to identify a statistical success rate. The statistics are summarized in Table 4, indicating the number of devices damaged after each major step and the reason to consider that damage.

Table 4. Success rate during the MEMS sensor micromachining.

Step	Wafer 1		Wafer 2	
	Working devices	Damaged devices and reason	Working devices	Damaged devices and reason
1.0	24	0	24	
2.0	24	0	23	Incautious handling, causing porous metallized pads
3.0	9	Comb fingers etched longer than needed, causing its disintegration	19	Incautious handling, causing some of the fingers to be improperly etched
4.0	0	SOI mask misalignment, causing complete misalignment of TRENCH	0	Cracking of the wafer during spin coat of the photoresist for exposing the TRENCH mask
5.0	0		0	
Success rate	0%		0%	

The fabricating process in the cleanroom has almost achieved the first device manufactured at NPS.

THIS PAGE INTENTIONALLY LEFT BLANK

VI. CONCLUSION AND FUTURE WORK

A. CONCLUSIONS

In this thesis, bio-inspired MEMS directional sound sensor was studied for potential application in an underwater environment. The sensor was designed using COMSOL finite element modeling and its frequency and directional responses in air and oil were simulated. A close agreement between simulations and characterization in an anechoic chamber was obtained with only a 6 Hz (< 1%) difference between the resonant frequencies. A housing was designed for testing the sensor underwater, immersing it in non-conducting silicone oil. Several materials were tested to get good acoustic transmission and the best material was found to be PMC-780 with a good acoustical transparency in the frequency band from 200 to 600 Hz.

The measurements carried out at NPS water tank and TRANSDEC underwater test facility showed a close agreement between measurements. However, the measurements show about 30 Hz higher resonant frequency compared to that of the simulations. This difference is about 15% and most likely arise from the approximation used in the modeling and limitations of the modeling software. The measured directional responses showed the expected dipole behavior associated with pressure gradient microphones.

An attempt was made to improve the modeling by including the effect of housing on the sensor response. It was found that the housing affects the frequency characteristics of the sensor due to its own vibrational modes in the frequency range of interest. A further refinement of the model is needed to accurately predict the frequency response of the sensor. Additionally, the resonant modes of the housing can be incorporated into the sensor response to further enhancement of the sensitivity.

In addition, the fabrication of the MEMS sensor using the NPS cleanroom facility was also explored using metallization, surface micromachining and DRIE etching processes, showing promising results. Further refinement of the process is needed to complete the fabrication.

B. FUTURE WORK

1. Simulation of the frequency response of the sensor including the underwater packaging and the circuit board in which it is mounted.
2. Redesign of the underwater packaging to reduce its size.
3. Explore the directional behavior of the sensor in regions away from the resonant frequency.
4. Explore the use of multiple sensors to accurately determine the bearing of sound sources.
5. Fine-tune the DRIE etch recipe in the cleanroom for etching of the device layer and the TRENCH on the backside of the wafer.
6. Investigate alternative means to spincoat the backside of the wafer.
7. Write integration code to automate the underwater calibrations.

APPENDIX A. HOUSING REDESIGN AND BOOT MANUFACTURING

The change of the protective housing with respect to the previous design simplified the assembly process. The previous process consisted of tightening six bolts while the whole assembly was submerged in oil [39]. The new process changed to locking a clamp and adding missing oil to the boot by a filling plug.

After exploring and testing different thicknesses, materials, and processes to build the boot, a 3-mm, black-pigmented, urethane, vacuum- and pressure-treated-during-molding boot was selected. The material employed for the boot of this prototype changed from Devcon Flexane 80 to Smooth-On PMC-780. This configuration of processes and material characteristics showed a similar frequency response with respect to a reference sensor calibrated without the boot. The numerous tests carried out suggested that the desired acoustical transparency to test the real sensor was achieved.

An additional advantage of the design here described is that it allowed fast prototype manufacturing and testing for different configurations of the boot, due to the acoustical effects probably caused by the boot itself [40].

A. HOUSING REDESIGN

The union interface between the closure-backing ring and the upper metallic plate changed from a bolted union to a compression sealing.

These modifications implied four changes:

1. Adapting a clamping device to produce the compressed sealing between the metallic plate and the closure backing ring in which the boot is adhered.
2. Redesigning of the mold to form the boot.
3. Restructuring the molding process and exploring different urethanes.

4. Improving the board holder between the electronic board and the upper metallic plate in which the bulkhead connector is installed.

The change in sealing interface, from bolted union to compressed sealing by clamping, required the analysis of desired specs that the sensor should withstand in order to be underwater tested. To address those requirements, a 150-psi-resistant clamp made of stainless steel or aluminum to prevent rust was selected. A mounting plate for the bulkhead connector was machined to the size. A board holder was designed and 3D printed. This allowed for connection of the sensor electronics to the surface cable, using an appropriate underwater connector. An exploded view of the digital model is shown in Figure 43.

B. BOOT MANUFACTURING PROCESS

1. Design Process of the Boot Mold

The previous housing for packaging the MEMS acoustic sensor for underwater applications was reported by Swan [38] and Collins [39]. The boot was molded using a Delrin mold. They used a polyurethane boot made of Flexane-80 liquid. This material is a two-part urethane compound. After molding, the boot was mounted on a metallic ring and filled with a synthetic oil, PSF-2cSt, to match the impedance between the sensor and the water [38].

The new version of the mold was designed and modified using a digital model of the boot using CAD software (SolidWorks). This version consisted of a splitting polyurethane casting mold for open-mold filling. The molds designed were manufactured by 3D printing the parts shown in Figure 59. The 3D printing process allowed for fast prototyping and molding.

The modification of the mold with respect to the previous versions used by Swan and Collins were:

1. Designing the boot according to the dimensions of the clamping interface, considering enough space to fit appropriately the sensor electronic board inside

2. Designing three different molds that produced 1.5-, 3-, and 5-mm boot thicknesses. This allowed experimental comparison of the variations on the response once the boot was installed

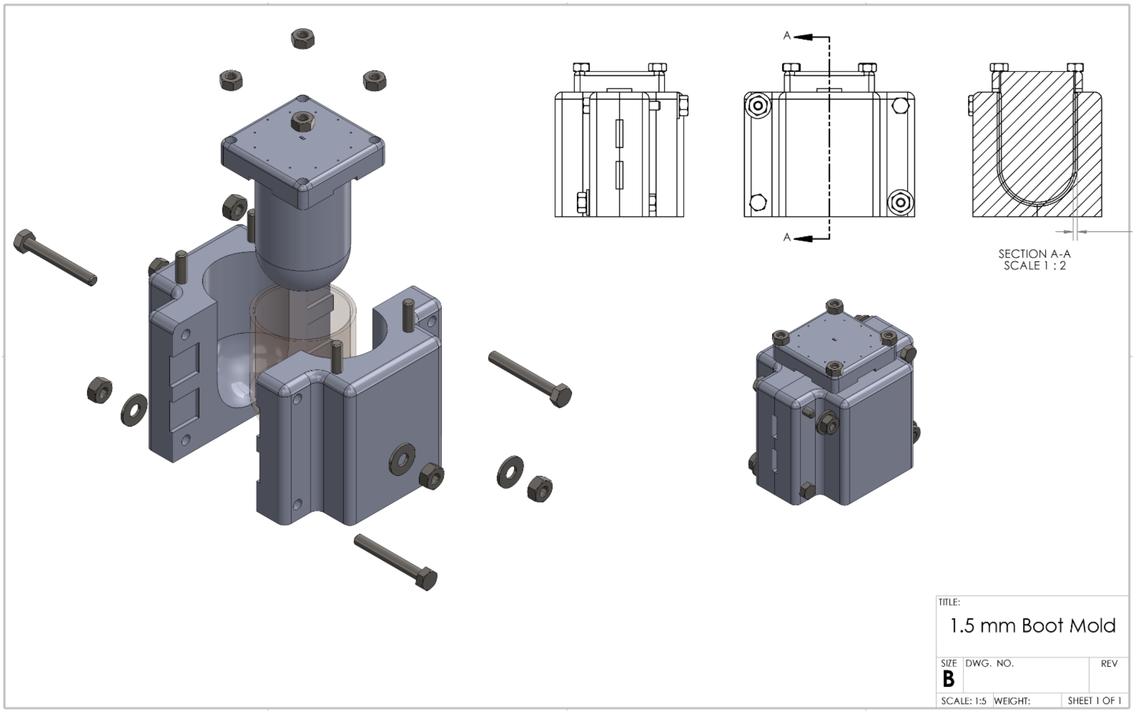

Figure 61. Exploded view of the mold

Once the mold was 3D printed, some finishing steps were required: sanding the inner sections to obtain smoother surfaces and adjusting the bolting holes used to seal the piece once the compound was poured into the mold.

2. Boot Molding Process

When the mold parts were ready, the boots were molded by two different techniques, using different materials. These variations were required to compare the results of the final cured polymers. The techniques employed were:

1. Mixing both parts of the urethane without any previous treatment, pouring it into the mold, and shaping it by compression when an inner core was inserted. After that, it was allowed to cure for 24 hours before demolding.

2. Degassing both parts of the polyurethane at a vacuum pressure of 29 inHg for 24 hours prior to mixing; once mixed, they were degassed again for ten minutes and molded as described in technique 1. After the mold was assembled, it was introduced into a pressure chamber and cured while applying 60 psi of pressure for at least 8 hours, depending on the specifications of the polymer being used.

The materials tested were:

1. DEVCON Flexane 80 liquid 15800. Black rubber flexible polyurethane, mixed in a 77A:23B weight ratio, which produced a flexible boot that required 24 hours to cure

2. Smooth-On PMC-780. Amber transparent flexible rubber polyurethane, mixed in a 2A:1B volume ratio, which produced a flexible boot and required 48 hours to cure

3. EpoxAcast 690. Clear transparent hard polyurethane, mixed in a 100A:30B ratio, which produced a rigid boot that required 24 hours to cure and heating the mold for 2 hours at 73 ºC for demolding

3. Boot Assembly

Before testing the boots, it was necessary to mount them on the upper metallic plate. This process required surface preparation of the polyurethane boot and the aluminum ring, sanding the section of each part that was going to be adhered to another part. Once sanded, two coatings were used: FL-10 adhesive as coating for the aluminum part and FL-20 adhesive as coating for the polyurethane boot and the FL-10 adhesive. After applying the coatings, an additional quantity of Flexane 80 was mixed and applied between the parts. This adhesion was allowed to cure for 24 hours.

After assembling the boot, the inner section was filled with oil and the assembly was degassed for 12 hours. During this part of the assembly process, it was noted that the oil released a significant amount of air bubbles when it was degassed on the boot, in contrast to degassing the oil in a different container, where it hardly released any bubbles. The microscope inspection allowed observing that some grooves of the mold were copied on the inner surface of the boot, producing cavities that possibly trapped air when the boot was filled with oil.

THIS PAGE INTENTIONALLY LEFT BLANK

LIST OF REFERENCES

[1] M. Lasky, “Review of World War I acoustic technology,” *U.S. Navy Journal of Underwater Acoustics,* vol. 24, no. 3, pp. 363–385, 1974.

[2] L. J. Ziomek, *Sonar Systems Engineering*, Boca Raton, FL, USA: Taylor & Francis Group, 2017.

[3] B. J. Nott, “Long-endurance maritime surveillance with ocean gliders,” M.S. Thesis, Dept. of Ocean., NPS, Monterey, CA, USA, 2015.

[4] R. N. Miles, D. Rober and R. R. Hoy, “Mechanically coupled ears for directional hearing in the parasitoid fly Ormia ochracea,” *Acoustical Society of America,* vol. 98, no. 6, pp. 3059–3069, 1995.

[5] D. Huang, “A hybrid pressure and vector sensor towed array.” United States Patent 12/221149, 24 July 2008.

[6] V. Pallayil, M. A. Chitre and P. Deshpande, “A Digital Thin Line Towed Array for Small Autonomous Underwater Platforms,” in *Oceans 2007*, Vancouver, 2007.

[7] J. Potter, E. Delory, S. Constantin and S. Badiu, “The ‘THINARRAY’; a lightweight, ultra-thin (8mm OD) towed array for use from small vessels of opportunity,” in *Proceedings of the 2000 International Symposium on Underwater Technology*, Tokyo, 2000.

[8] A. Maguer, R. Dymond, M. Mazzi, S. Biagini, S. Fioravanti and P. Guerrini, “SLITA: A new Slim Towed Array for AUV applications,” in *Proc. of Acoustics*, Paris, 2008. [Online]. Available: http://www.conforg.fr/acoustics2008/cdrom/data/articles/000200.pdf.

[9] F. Edalatfar, S. Azimi, A. Qureshi, A. Yaghootkar, A. Keast, W. Friedrich, A. Leung and B. Bahreyni, “A Wideband, Low noise Accelerometer for Sonar Wave Detection,” *IEEE Sensors Journal,* vol. 18, no. 2, pp. 508–516, 2017.

[10] S. Choi, H. Lee and W. Moon, “A micromachined piezoelectric hydrophone with hydrostatically balanced air backing,” *Sensors and Actuators,* vol. A 158, pp. 60–71, 2010.

[11] C. H. Sherman and J. L. Butler, *Transducers and Arrays For Underwater Sound*, Cohasset, MA, USA: Springer, 2007.

[12] B. M. Gür, H. de Bree and T. Akal, “A comparative analysis of triplet and vector sensor arrays,” in *Proc. of the 10th European Conference on Underwater Acoustics*, Istanbul, 2010. pp. 927–930. [Online]. Available: http://berkegur.com/wp-content/uploads/2015/07/ECUA2010_270_GurBreeAkal.pdf.

[13] T. AAkal, H.-E. de Bree and B. Gur, “Hydroflown based low frequency underwater acoustical receiver,” in *Proc. 4th Int. Conf. & Exhib. in Underwater Acoustics Measurements: Technologies & results*, Kos island, 2011, pp. 871–878.

[14] J. Merhaut, “Theory of electroacoustic receivers,” in *Theory of Electroacoustics*, New York, London: McGraw-Hill International, 1981, pp. 274–311.

[15] D. A. Brown, B. Aronov, L. Reinhart and T. Oishi, “Acoustic pressure gradient sensors: piezoelectric motion and fixed types,” in *Proceedings of the Workshop on Directional Acoustics Sensors*, Newport, 2001.

[16] L. L. Beranek and T. J. Mellow, *Acoustics Sound Fields and Transducers*, Oxford: Elsevier, 2012.

[17] R. Dymond, A. Sapienza, L. Troiano, P. Guerrini and A. Maguer, “New vector sensor design and calibration measurements,” in *Fourth International Conference of Underwater Acoustic Measurements: Technologies and Results*, Kos, 2011.

[18] M. J. M. Hazemans, “Feasibility study to adapt the microflown vector sensor for underwater use,” M.S. Thesis, Dept. of Ocean., NPS, Monterey, CA, USA, 2012.

[19] H.-E. de Bree, B. M. Gur and T. Akal, “The Hydroflown: MEMS-based underwater acoustical particle velocity sensor. The sensor, its calibration and some possible localization techniques,” in *Third International Conference & Exhibition on Underwater Acoustic Measurements: Technologies & Results,* Nafplion, 2009.

[20] H.-E. de Bree, E. Tijs and T. Akal, “The Hydroflown: MEMS-Based Underwater Acoustical Particle Velocity Sensor Results of lab tests and sea trials,” in *Tenth European Conference on Underwater Acoustics*, Istanbul, 2010.

[21] C. J. Shipps and K. Deng, “A miniature vector sensor for line array applications,” in *Oceans 2003. Celebrating the Past ... Teaming Toward the Future*, San Diego, 2003.

[22] C. J. Shipps and B. M. Abraham, “The Use of Vector Sensors for Underwater Port and Waterway Security,” *Sensors for Industry Conference,* pp. 41–44, 2004.

[23] Wilcoxon Sensing Technologies, “Mid-frequency vector sensor VS-209 brochure,” October 2018. [Online]. Available: https://wilcoxon.com/wp-content/uploads/2018/11/VS-209-spec-99080NCB.1.pdf

[24] C. B. Leslie, J. M. Kendall and J. Jones, "Hydrophone for Measuring Particle Velocity," *The Journal of the Acoustical Society of America,* vol. 28, no. 4, pp. 711–715, 1956.

[25] L. Guan, G. Zhang, J. Xu, C. Xue, W. Zhang and J. Xiong, "Design of T-shape vector hydrophone based on MEMS," in *16th Int. Solid-State Sensors, Actuators and Microsystems Conf.*, Beijing, 2012. [Online]. https://doi.org/10.1109/TRANSDUCERS.2011.5969121

[26] C. Xue, Z. Tong, B. Zhang and W. Zhang, "A Novel Vector Hydrophone Based on the Piezoresistive Effect of Resonant Tunneling Diode," *IEEE Sensors Journal,* vol. 8, no. 4, pp. 401–402, 2008.

[27] C. Sungjoon, L. Haksue and M. Wonkyu, "A micro-machined piezoelectric hydrophone with hydrostatically balanced air backing," *Sensors and Actuators,* vol. A 158, pp. 60–71, 2010.

[28] M. Touse, J. Sinibaldi, K. Simsek, J. Catterlin, S. Harrison and G. Karunasiri, "Fabrication of a microelectromechanical directional sound sensor with electronic readout using comb fingers," *Applied Physics Letters,* no. 96, p. 173701, 2010.

[29] R. H. Downey, L. N. Brewer and G. Karunasiri, "Determination of mechanical properties of a MEMS directional sound sensor using a nanoindenter," *Sensors and Actuators,* vol. A 191, pp. 27–33, 2013.

[30] R. H. Downey and G. Karunasiri, "Reduced residual stress curvature and branched comb fingers increase sensitivity of MEMS acoustic sensor," *Journal of Microelectromechanical Systems,* vol. 23, pp. 417–423, 2014.

[31] R. H. Downey, "Toward a micro.scale acoustic direction-finding sensor with integrated electronic readout," Ph.D. Dissertation, Dept. of Phys., NPS, Monterey, CA, USA, 2013.

[32] M. Touse, "Design, fabrication, and characterization of a microelectromechanical directional microphone," Ph.D. Dissertation, Dept. of Phys., NPS, Monterey, CA, USA, 2011.

[33] T. J. Shivok, "MEMS polymumps-based miniature microphone for directional sound sensing," M.S. Thesis, Dept. of Phys., NPS, Monterey, CA, USA, 2007.

[34] D. Grevenitis, "Effects of substrate on response of MEMS directional sound sensor," M.S. Thesis, Dept. of Phys., NPS, Monterey, CA, USA, 2010.

[35] S. C. W. Harrison, "Free field modeling of a MEMS-Based pressure gradient microphone," M.S. Thesis, Dept. of Ocean., NPS, Monterey, CA, USA, 2009.

[36] D. D. Davis, “Characterization of the MEMS directional sound sensor in the high frequency (15 - 20 kHz) range,” M.S. Thesis, Dept. of Phys., NPS, Monterey, CA, USA, 2011.

[37] J. D. Roth, “Integration of high sensitivity MEMS directional sound sensor with readout electronics,” M.S. Thesis, Dept. of ECE, NPS, Monterey, CA, USA, 2012.

[38] W. D. Swan, “Bio-inspired MEMS direction finding acoustic sensor for air and underwater applications,” M.S. Thesis, Dept. of Phys., NPS, Monterey, CA, USA, 2016.

[39] J. D. Collins, “Bio-Inspired MEMS underwater direction finding acoustic sensor,” M.S. Thesis, Dept. of Ocean., NPS, Monterey, CA, USA, 2017.

[40] G. Da Re, “MEMS underwater direction finding acoustic sensor,” M.S. Thesis, Dept. of Ocean., NPS, Monterey, CA, USA, CA, 2018.

[41] M. A. Hopcroft, N. . D. William and K. W. Thomas , “What is the Young’s Modulus of Silicon?,” *Journal of Microelectromechanical Systems,* vol. 19, no. 2, pp. 229–238, April 2010.

[42] Smooth On, “PMC-780 Dry & PMC-780 Wet,” 22 August 2012. [Online]. Available: https://www.smooth-on.com/tb/files/PMC-780_Dry-Wet.pdf

[43] DEVCON, “Flexane 80 Liquid,” 2012. [Online]. Available: https://www.freemansupply.com/datasheets/Devcon/flexane80.pdf

[44] T. Klose, H. Conrad, T. Sandner and H. Schenk, “Fluidmechanical damping analysis of resonant micromirrors with out-of-plane comb drive,” in *COMSOL Conference*, Hannover, 2008.

[45] W. O. Davis, “Nonlinear air drag damping of torsional microscanners,” in *16th International Solid-State Sensors, Actuators and Microsystems*, Beijing, 2011.

[46] G. Mennig and K. Stoeckhert, *Mold-Making Handbook,* Munchen: Hanser Publications, 2013.

[47] IEC 60565, International Electrotechnical Commission, *Underwater Acoustics-Hydrophones,* Geneva, 2006.

[48] T. Ramotowski, “NUWC XP-1 Polyurethane-Urea: A new, “Acoustically Transparent” Encapsulant for Underwater Transducers and Hydrophones,” *Oceans 2003 MTS/IEEE Conference,* 2003.

[49] MEMSCAP Inc., "SOIMUMPs Design Handbook," 2011. [Online]. Available: http://www.memscap.com/__data/assets/pdf_file/0019/1774/SOIMUMPs.dr.v8.0.pdf

[50] C. Liu, *Foundations of MEMS*, Hoboken, NJ, USA: Pearson Education, 2006.

[51] A. A. Carey, *The dielectric constant of lubrication oils,* Knoxville, TN, USA: Computational Systems Incorporated, 1998.

[52] *Procedures for Calibration of Underwater Electroacustic Transducers,* ANSI/ASA Standard S1.20, 2012, Melville, NY, USA: Acoustical Society of America.

[53] Bruel & Kjaer, *Hydrophones Types 8103, 8104, 8105 and 8106,"* Nærum, Denmark: Bruel & Kjaer, 1992.

[54] P. Riarh, private communication, 2018.

THIS PAGE INTENTIONALLY LEFT BLANK

INITIAL DISTRIBUTION LIST

1. Defense Technical Information Center
   Ft. Belvoir, Virginia

2. Dudley Knox Library
   Naval Postgraduate School
   Monterey, California